

# **Holographic and Hybrid Spectacle Lenses**

**Dissertation**  
**zur Erlangung des akademischen Grades**  
**doctor rerum naturalium (Dr. rer. nat.)**

**vorgelegt dem Rat der Physikalisch-Astronomischen Fakultät  
der Friedrich-Schiller-Universität zu Jena**

**von M.Sc. Jannik Michael Trapp**  
**geboren am 21.02.1990 in Frankenthal (Pfalz)**

1. Gutachter: .....

2. Gutachter: .....

3. Gutachter: .....

Tag der Disputation: .....

# Deutschsprachige Zusammenfassung

Die vorliegende Arbeit behandelt das Design und die Analyse von neuartigen holographischen und holographisch-refraktiven Brillengläsern. Ziel ist es hierbei, das Potential von Hologrammen, wie die Möglichkeit komplizierte optische Funktionen in einer dünnen Schicht zu realisieren oder die Möglichkeit die Dispersion von refraktiven Linsen zu kompensieren, für verbesserte Designs von Brillengläsern zu nutzen. Eine besondere Schwierigkeit an dieser Aufgabenstellung besteht darin, die Eigenschaften von Hologrammen wie hohe Winkel- und Wellenlängenabhängigkeit der Beugungseffizienz und starke Dispersion so zu kontrollieren, dass sie für das Design von Brillengläsern vorteilhaft oder zumindest nicht nachteilig sind. Eine weitere Schwierigkeit besteht darin, Konzepte aus dem Design herkömmlicher Brillengläser, wie die gleichzeitige Optimierung für verschiedene Blickrichtungen des Auges, auf Hologramme anzuwenden und diese entsprechend anzupassen. Zu diesem Zweck wurde eine Designmethode neuentwickelt, die es ermöglicht entsprechend für den Einsatz in Brillengläsern geeignete Hologramme zu entwerfen und zu analysieren. Diese Methode ist geeignet um sowohl holographische als auch holographisch-refraktive Brillengläser zu entwerfen und zu optimieren. Die Brillengläser können dabei einfache Einstärkengläser oder Gleitsichtgläser sein.

Das Verständnis dieser Arbeit erfordert Vorkenntnisse aus den Bereichen Holographie und dem Design von Brillengläsern. Da dies eine in der Literatur so bisher noch nicht vorgekommene Kombination ist, werden die Historie und der Stand der Technik von sowohl Holographie als auch vom Design von Brillengläsern in der Einleitung dieser Arbeit beschrieben. Kapitel II greift die in der Einleitung als Überblick beschriebenen Konzepte auf und erläutert die für das Verständnis der neu entwickelten Designmethode benötigten Methodiken und theoretische Hintergründe im Detail. Besonders wichtig ist hierbei, wie im Design von Brillengläsern mit den verschiedenen Blickrichtungen des Auges umgegangen wird und die Beschreibung von Volumen hologrammen und ihrer Beugungseffizienz. Die neu entwickelte Designmethode wird in Kapitel III beschrieben. Nach einer Abschätzung, wie groß die benötigten Winkel- und Wellenlängen für die Beugungseffizienz der Hologramme sind, wird mittels der Fourier Modal Methode ein Parameterbereich aus Gitterperiode, Gitterdicke und Modulationsstärke des Brechungsindex identifiziert, in dem die Anforderungen an die Beugungseffizienz der Hologramme erfüllt sind. Ein fester Parameterbereich für die Gitterperiode wirkt sich auf die möglichen Ablenkwinkel zwischen einfallendem und gebeugtem Strahl der ersten Beugungsordnung aus und erlaubt es nicht Ablenkwinkel von  $0^\circ$  einzustellen. Daher ist es in diesem Fall nicht möglich, dass Licht der ersten Beugungsordnung gerade durch die Linsenmitte eines Brillenglases mit einem Hologramm geht. Diese Limitation wird in der Designmethode dadurch umgangen, dass ein Tandem aus zwei Hologrammen genutzt wird, deren Dispersion und

Ablenkwinkel sich teilweise oder vollständig kompensieren können. Dies ermöglicht eine gerade Durchsicht durch die Linsenmitte sowie eine reduzierte Dispersion des Hologrammtandems. Die Dispersion des Hologrammtandems kann weiterhin mit der Dispersion einer refraktiven Linse in einem holographisch-refraktiven Brillenglas kompensiert werden. Um von diesen Erkenntnissen bezüglich Beugungseffizienz und Dispersion zu einem holographischen Brillenglasdesign zu kommen, ist es notwendig, die lokale Variation der Hologramm Parameter, wie der Gitterperiode und der Neigung des Gittervektors im Volumen, zu kontrollieren und für jede Blickrichtung des Auges anzupassen. Im Kapitel III wird daher auch detailliert beschrieben, wie eine geschickte Implementierung der Hologramm Parameter in einer Optikdesignsoftware und vorher berechnete Initialwerte der fraglichen Parameter genutzt werden können, um die Leistung von holographischen und holographisch-refraktiven Brillengläsern gezielt zu optimieren. Dabei wird auch beschrieben, wie komplizierte optische Funktionen wie etwa die einer Gleitsichtbrille mit Hologrammen nachgebildet werden können.

Die mit Hilfe der neu entwickelten Designmethode gewonnenen Designs für holographische oder holographisch-refraktive Brillengläser werden in Kapitel IV präsentiert und diskutiert. Für holographisch-refraktive Einstärkengläser wird dabei gezeigt, dass es möglich ist, den bei hohen Brechkraften störenden Farbfehler durch die Kompensation von Dispersion deutlich zu reduzieren und dabei auch die Randdicke der Gläser zu reduzieren. Außerdem ist es teilweise möglich, die durch Asphären mögliche Korrektur der Brechkraft und des Astigmatismus mittels Hologrammen zu ersetzen. Für Gleitsichtgläser wird gezeigt, dass es für Additionsbrechkraften von bis zu zwei Dioptrien möglich ist, die optische Funktion von refraktiven Gleitsichtgläsern mit holographischen Gleitsichtgläsern nachzubilden.

Zum Abschluss wird noch über die Ergebnisse dieser Arbeit hinaus diskutiert, wie die hier vorgestellten Konzepte im Bereich Augmented Reality (AR) oder speziellen Brillen zur Prävention von Myopie genutzt werden können.

# Contents

<b>I. Introduction</b>	<b>5</b>
1.1. History and state of the art . . . . .	5
1.2. Motivation and scope of this work . . . . .	14
<b>II. Background</b>	<b>17</b>
2.1. Spectacle lenses . . . . .	17
2.2. Volume holography . . . . .	33
<b>III. Holographic optical element design method for spectacle lenses</b>	<b>47</b>
3.1. Diffraction efficiency optimization . . . . .	48
3.2. Dispersion and deflection angle management . . . . .	55
3.3. Micro lens approach . . . . .	58
3.4. Continuous holographic optical element approach . . . . .	61
<b>IV. Holographic and hybrid spectacle lens designs</b>	<b>81</b>
4.1. Holographic and hybrid single vision spectacle lenses . . . . .	81
4.2. Holographic progressive addition lenses . . . . .	89
<b>V. Summary and Outlook</b>	<b>97</b>
5.1. Summary . . . . .	97
5.2. Outlook . . . . .	98
<b>Bibliography</b>	<b>100</b>
<b>List of abbreviations</b>	<b>119</b>
<b>Acknowledgements</b>	<b>120</b>
<b>Ehrenwörtliche Erklärung</b>	<b>122</b>
<b>Publications</b>	<b>123</b>
<b>Curriculum Vitae</b>	<b>124</b>



# I. Introduction

In recent years, holography has started to attract a lot of public attention through augmented reality (AR) applications such as the Microsoft HoloLens or automotive head-up displays (HUDs). Holograms have been used in AR applications for a long time, because their strong angle and wavelength selectivity allows designing see-through combiners that are transparent for the environment, but still guide the light from a hidden display towards the eyes of the user. Due to material and manufacturing limitations, applications remained in high-end segments such as military aircraft for decades. The new wave of popularity is mainly driven by advances in holographic materials and surrounding technologies that enable AR applications in consumer-friendly pricing segments. Similar to earlier waves of popularity, for example the wide use of image holograms in museums and representation in science fiction movies like Star Wars, holography again promises to profoundly alter how people interact with technology. This begs the question if there are further applications for holography outside of the realm of AR, which is currently being explored by a large number of research groups. Due to its similarity to near-to-eye AR applications, spectacle lens design is a promising candidate to evaluate possible benefits of connecting it with holography.

## 1.1. History and state of the art

This thesis connects two long-lived fields of research: spectacle lens design and holography. Because there is no significant overlap between these two fields in literature, their histories and current developments are discussed separately. The aim of this discussion is to provide a broader context for Sect. 1.2, in which the benefits of connecting these two fields are explained in detail.

### 1.1.1. Spectacle lenses

Ideally, the optics of the human eye focuses incident light on the retina to enable error-free vision. In reality, approximately one third of persons above the age of 40 in the United States and Western Europe suffer from refractive errors [1] such as myopia (light focuses in front of the retina because the optics of the eye is too strong or the eyeball is too long), hyperopia (light focuses behind the retina because the optics of the eye is too weak or the eyeball is too short), astigmatism (light is split into two foci due to irregular curvature of the eye optics) or presbyopia (age related process, stiffened eye lens can no longer change its curvature to focus on near objects). The prevalence of myopia is even higher in Asia, where myopia has become a huge socioeconomic issue with myopia rates as high as 84% in school children [2, 3, 4, 5]. Modern treatment options for refractive errors include spectacle lenses [6, 7], contact lenses [8] and refractive eye surgery [9] with spectacle lenses being the most versatile and least invasive one. The main challenge of spectacle lens design is to limit unwanted aberrations, especially for oblique gaze directions of the eye, while correcting the refractive errors of the eye by providing the required prescription. The aberrations discussed in this context are oblique spherical power error (remaining offset between the light focus and the patient's retina) and oblique astigmatism (different positions for meridional and sagittal foci), while other aberrations such as transverse color error can not be addressed with existing spectacle lens design principles [6, 7]. In the following, notable innovations of spectacle lens design history are outlined with special attention to recent research papers and patents.

At first glance, designing a spherical lens to act as a single vision spectacle lens, which corrects refractive errors of the eye such as myopia, hyperopia or astigmatism of a given prescription power, is a straight forward task. In a simplified model ignoring lens thickness, the spherical power (SPH) of the lens can be expressed as the sum of the front surface power  $P_1$  and the back surface power  $P_2$  as  $SPH = P_1 + P_2$ . In principle, this means that a target prescription can be achieved by infinite combinations of front power  $P_1$  and the back surface power  $P_2$  even when only considering meniscus lenses ( $P_1$  takes a positive value,  $P_2$  takes a negative one) due to their preferable form factor. The possible combinations of front and back surface powers to achieve a given prescription differ in how curvy the resulting lens looks like, and, more importantly, in how strongly they induce aberrations, such as power error or astigmatism for oblique gaze directions of the eye. Therefore, choosing the best combination of front and back surface power, also



referred to as choosing the base curve, is of central importance in spectacle lens design. Since it is not possible to correct both oblique power error and astigmatism at the same time, lens design theories differ by which oblique errors they minimize [6, 7].

The first notable contribution to the problem of choosing the optimal base curve was made by W. Wollaston in 1804 [10]. He published a formula to calculate a base curve for a given prescription so that the astigmatism induced by the front surface of the lens is compensated by the astigmatism induced by the back surface of the lens. However, his "periscopic" spectacle lenses were unpractical as the high base curve values lead to a bulky lens form. In 1898, F. Ostwalt published another spectacle lens design theory on oblique astigmatism compensation with flatter base curves [11]. The work of Wollaston and Ostwalt was connected by M. Tscherning in 1904, who showed that their designs are both solutions to a quadratic formula that minimizes oblique astigmatism and became known as the Tscherning Ellipse [12]. The Ostwalt solutions on the Tscherning Ellipse are still used for picking base curves in current spectacle lens design practice. The first commercial success of an oblique astigmatism corrected lens design was the "Punktal" (point-focal) lens, which was patented by M. von Rohr of the Zeiss corporation in Germany in 1911 and was later mass produced [13, 14]. However, the downside of these astigmatism compensated approaches is that they have large power error i.e. differences between the prescription power and achieved SPH for oblique gaze directions. The first spectacle lens design theory aiming at minimizing oblique power error rather than oblique astigmatism was published by the English ophthalmologist A. Percival in 1914 [15, 16]. His approach can be understood as minimizing the circle of least confusion between the meridional and sagittal foci and placing it on the retina rather than minimizing the distance between the meridional and sagittal foci and accepting that the circle of least confusion is not on the retina. These concepts are discussed in more depth in Chapt. II. While A. Percival's theory was an improvement over the previous astigmatism corrected lenses [16] in terms of visual acuity, it is not necessary to restrict spectacle lens design to base curves that either minimize oblique power error or astigmatism. In 1917, E. Tillyer of the American Optical Company patented a lens design concept that allowed error budgets for power error as well as astigmatism, which significantly improved spectacle lens performance. E. Tillyer also considered that lens designs should facilitate easy ordering and stocking procedures. Therefore, he proposed that prescriptions should be grouped in 0.12 dpt steps for lower value prescriptions and 0.25 dpt steps for higher prescriptions. This procedure significantly reduces the required stock of lens manufacturers and is still

used for semi-finished lenses today [17, 18].

After the possibilities for oblique error correction by spherical lenses were exhausted by the work of E. Tillyer, the next noteworthy improvement of single vision spectacle lenses was the use of aspherical surfaces, which were previously only used in high positive power aphakic spectacle lenses for cataract patients [19]. The first single vision spectacle lens designs featuring an aspherical surface to further reduce oblique errors were plano-aspheric lenses introduced by W. Merte in 1950 [20]. This was later improved upon, when atoric spectacle lenses were patented in 1968 by the Société des Lunetiers in France [21]. Later, aspherical surfaces were also used to improve the form factor rather than just to minimize oblique errors. In 1981, M. Jalie patented lenses, for which the spherical surface of greater curvature is replaced by a hyperbolic surface to make it flatter and thinner without increasing oblique errors [22]. Shortly after, in 1983, the Tscherning Ellipse was also updated to predict astigmatism compensated base curves for aspheric spectacle lenses [23].

In parallel to the continuous development of single vision spectacle lenses to correct myopia, hyperopia and astigmatism, several different spectacle lens types have been developed to correct presbyopia, which is the age related stiffening of the eye lens leading to a difficulty to focus on near distance objects. The initial solutions to this problem were bifocal and trifocals lenses, which were introduced in 1784 and 1826, respectively [24, 25]. They are lenses whose surface is separated into two or three discrete viewing zones with different curvatures for near and far distance use. The downside of bifocals and trifocals is that there is an edge causing the image to "jump" between the different viewing zones. This can be circumvented by progressive addition lenses, which have a locally varying curvature to smoothly transition from near to far distance viewing. The locally varying curvature comes with the downside of inducing unwanted astigmatism as described by Minkwitz theorem [26, 27]. The first progressive addition lenses are known since the beginning of the 20th century [28, 29], but due to manufacturing limitations the first commercially successful progressive addition lens was designed by B. Cretin-Maitenaz of the company Essilor in 1958 [30].

Initially, the cost effective production of progressive addition lenses relied on pre-manufacturing large quantities of semi-finished lenses, where the progressive surface was already ground and a spherical surface would later be added based on the full prescription of the patient. With improvements in manufacturing technology it became cost effective to stock semi-finished lenses with spherical surfaces and manufacture complex surfaces

such as progressive surfaces or other complicated freeforms based on the prescription of the patient on demand [31, 32]. Since then, it has become feasible to customize spectacle lenses for individual patients as well as for different use cases such as computer work or driving.

In recent years, research interest in spectacle lenses has mainly focused on further improvements of progressive addition lenses as well as specialized lenses for myopia control, i.e. lenses that slow down myopia progression in children rather than to simply correct the refractive error of myopia. The research that is still being done in the field of single vision spectacle lenses is on developing higher order aberration theories, such as third order and fifth order theories [33, 34, 35, 36, 37, 38], correcting higher order aberrations via aspheres [39], improvements on lens optimization routines, e.g. suggesting new design algorithms [40], algorithm improvements for asphere optimization [41, 42], lens design by taking the closer object distances into account for myopia [43] or extending the depth of focus of the lens [44]. In the field of progressive addition lenses, some work is done explicitly on the individualization of the progressive addition lens [45, 46], while others focus on novel design and modeling methods for progressive surfaces [47, 48, 49, 50, 51, 52, 53]. After gradient index progressive addition lenses have been researched for some time [54, 55, 56, 57, 58, 59, 60], the recent research interest is on tunable lenses such as liquid crystal diffractive lenses [61, 62, 63, 64], liquid crystal gradient index lenses [65] or tunable liquid lenses [66]. By changing their power on demand, these lenses could become a viable alternative to progressive addition lenses, which suffer from unwanted astigmatism induced by the progressive surface according to Minkwitz theorem. Recently, a spectacle lens including a binary zoom function based on a liquid crystal gradient index lens has become commercially available in Japan [67, 68]. Due to the increase in myopia, especially in Asia, a lot of research is conducted on how spectacle lenses can be used to slow down the progression of myopia in children [69, 70]. The proposed solutions based on spectacle lenses can be grouped into either progressive addition lens-based ones [71, 72, 73, 74, 75, 76, 77] or approaches of altering the field curvature of single vision lenses for the peripheral vision [78, 79].

In summary, spectacle lens design has become very mature over the last decades and the possibilities of correcting the main optical errors, oblique spherical power error and oblique astigmatism, via refractive lenses seem to be well-exhausted. Therefore, innovation in the field of spectacle lenses likely requires the introduction of new technology, such as holography, into the field.

### 1.1.2. Volume holography

While the design and manufacturing of spectacle lenses is a research field with a relatively well-defined set of applications, holography comprises a multitude of wavefront reconstruction techniques that cater to a wide range of applications. The term "volume holography" describes wavefront reconstruction techniques, which are based on recording interference patterns as refractive index modulations into thick volumes (relative to the wavelength) of photosensitive materials [80]. For a typical image hologram, a two step process is followed: In the recording step, a coherent wave is split into two paths by a beam splitter. The first path, called the object wave, illuminates an object and is scattered from it. The second path, called the reference wave, remains a plane wave. The optical setup is constructed in such a way, that the object and reference wave then interfere and the interference pattern is recorded on a photosensitive material. After some steps to permanently fix the interference pattern, the photosensitive material is considered a hologram. In the reconstruction step, the hologram is illuminated by the reference wave and diffracts it in such a way, that the object wave is reconstructed. An observer then sees a recreation of the object as a 3D image with perspective and depth. For appropriate hologram parameter choices and the incident light being the reference wave, which obeys the Bragg condition, volume holograms are capable of reconstructing a desired wavefront with unity diffraction efficiency [81]. Violating the Bragg condition either by angle or wavelength detuning quickly reduces diffraction efficiency [80]. This combination of high peak diffraction efficiency and small angular and wavelength bandwidth make volume holograms interesting optical components for many applications that require partial transparency such as optical combiners. In the following, the history of holography is discussed along recent research trends with special attention to current applications of volume holograms.

The beginning of holography dates back to experiments conducted by D. Gabor in 1948, which originally aimed at reducing aberrations in electron microscopes. By chance, he discovered the two step process of recording and reconstruction holograms described in the previous paragraph. But the reconstructed object waves achieved by Gabor were of poor visibility and low contrast since his on-axis configuration did not allow to spatially filter the used diffraction order from the zeroth order light [82, 83]. The work of D. Gabor did not attract much attention due to the lack of strong coherent light sources until the the invention of the laser in 1960 [84]. Two years later, E. Leith and J. Upatniek recorded

the first high quality holograms, in which they employed an off-axis geometry to spatially filter out the zeroth order [85]. Gabor as well as E. Leith and J. Upatniek recorded transmission holograms i.e. holograms, in which the object wave and reference wave travel in the same direction. The first reflection hologram was recorded by Y. Denisyuk in 1962, which was also the first hologram that could be used with white light as he used lasers with three different wavelengths in the recording process [86, 87]. One of the main drawbacks of the first holograms was that recording an interference pattern into a photosensitive material modulates the real and imaginary parts of the refractive index of the photosensitive material. Since the imaginary part of the refractive index corresponds to absorption, these holograms absorb a part of the incident light, which then is not available to achieve the maximum possible image brightness. It was first mentioned by G. Rogers in 1952 and then later treated in greater detail by W. Cathey in 1965 that bleaching a hologram can remove the absorption modulation, while keeping the modulation of the real part of the refractive index intact. The resulting phase hologram is then still capable of reconstructing the amplitude and phase information of an object wave. The absence of absorption related losses in image brightness makes phase holograms the standard choice for holography applications today [88, 89, 90, 91].

With growing interest in holography, it became important to theoretically predict the diffraction efficiency behavior of a given hologram parameter choice. In 1969, H. Kogelnik derived analytical, approximate formulas for hologram diffraction efficiency, which became known as Kogelnik theory or two wave coupled wave theory because of the assumptions used: neglecting boundary conditions, neglecting second derivatives of the field amplitudes and retaining only two waves (one diffracted wave and the transmitted wave). Even though the assumptions of Kogelnik theory are only valid for holograms with a high peak efficiency, they are used for their simplicity up to today [92]. Another reason for the popularity of Kogelnik theory was that the rigorous methods of calculating diffraction efficiency of surface gratings were not applicable to volume holograms because of computational limitations for many years. This only changed in 1981 when M. Moharam and T. Gaylord published an easy to compute rigorous coupled wave analysis that allowed to accurately predict the diffraction efficiency behavior of volume holograms without approximations or assumptions [93].

The holographic processes described so far, such as using the light scattered from a real object as the object wave in the hologram recording process or reading-out a hologram with a physically present reference wave, are referred to as analogue holography.

However, both the recording and reconstruction can be done by digital means, which is then referred to as digital holography. In the recording step, an object wave with the desired properties can be computed instead of being scattered from a real object. In the reconstruction step, the fringe pattern of a hologram can be the input to a computational reconstruction of the object wave rather than being illuminated by a physically present reference wave to recreate the object wave by diffraction. Holograms created with a computed object wave are known as computer generated holograms (CGHs). Since the 1960s CGHs are used as filters or as optical elements e.g. holographic lenses or mirrors [94, 95, 96]. CGHs can be volume holograms in the sense that a computer generated phase mask is written into a 3D volume holographic film [97, 98], or the computer generated phase mask can be realized as a phase modulations profiles on spatial light modulators (SLMs) [99, 100, 101, 102] or, since recently, as metasurfaces, which allow to modulate the amplitude and phase of a wavefront within thin dielectric or plasmonic layers [103, 104, 105, 106, 107, 108, 109, 110, 111]. Both SLMs and metasurfaces realize phase functions in a way that is better compared to 2D surface gratings like blazed gratings than to 3D modulations of the refractive index of a volume hologram. Volume hologram CGHs are often used to generate holographic optical elements (HOEs) that act as lenses, as mirrors or have complicated non-standard optical functions e.g. holographic lens arrays with varying aberration profiles for adaptive optics [112]. HOEs with a lens-type function are often a cascade or tandem of several holograms to either increase the wavelength bandwidth for the use in polychromatic systems [113, 114] or angular bandwidth for wide angle lenses [115]. Wide angle lenses can also be realized by partitioning the field into different sub-holograms [116]. In this context, holographic-refractive hybrid optics have been investigated [117], even though angular and wavelength bandwidth limitations restrict their potential use cases [118, 119]. SLM-based CGHs are an interesting alternative to static volume hologram CGHs as they can perform fast switching between optical functions, which enables their application in optical filters e.g. for telecommunication channel management, where they bring benefits like transparency, low crosstalk, low losses and high switching speeds [99] or in see-through displays, where they are crucial for displaying video information [100, 101, 102]. Apart from being used as CGHs, SLMs can also be used to record volume holograms that are CGHs. Instead of recreating the object wave required in the recording process of a CGH by conventional optical components, the object wavefront can be created with an SLM. Due to the pixelation of the SLM, the SLM image is typically demagnified and the CGH is written as an array of holographic

pixels (hogels). This type of recording setups is therefore referred to as a holographic printer [120, 121, 122, 123, 124]. Aside from the wide spread use of CGHs discussed so far, the concepts and algorithms of digital holography are also used in many image reconstruction applications. Recording the interference pattern of a known reference wave and an object wave on an image sensor like a CCD allows calculating the object image [125]. This concept is used in digital holographic microscopy to image phase objects like living cells with high sensitivity [126, 127, 128, 129] or adaptive optics for astronomical imaging with dynamic compensation of atmospheric turbulence [130, 131].

While digital holography found its use in many applications thanks to technological advances in image sensors, computational resources and SLMs [132, 133, 134, 135, 136, 137], analogue holography suffered from a lack of holographic materials suitable for industrial mass production in terms of processing difficulty and environmental stability. Consequently, for a long time applications were limited to expensive high end use cases with small production quantities such as military aircraft head-up displays (HUDs) [138]. A lot of research on holographic materials was done in the 1990s, when holographic data storage attracted a lot of interest as volume holograms promised high data capacity and fast read-out speeds. To date holographic storage has not been able to develop into a commercial alternative to magnetic storage [139, 140, 141, 142, 143, 144, 145], but research on holographic data storage has significantly benefited other applications of holography due to progress in holographic materials. Most notably, Bayfol, a photosensitive material for holography, is a successor of materials that have been developed originally for holographic storage. Bayfol has several advantages over previous materials such as dichromated gelatin, most notably that it is sold as thin films on a polymer substrate, which do not require any wet chemical or thermal processes, and great stability under light and temperature. Bayfol starts to enable a broad commercial breakthrough in volume holography, especially in augmented reality (AR) applications [145, 146, 147, 148, 149, 150, 81, 151, 91, 138] HOEs based on volume holograms are used as optical combiners in AR systems since their high peak diffraction efficiency at narrow angular bandwidth allows them to efficiently project a display image into the users view while being transparent for the other incident light. Furthermore, they can include arbitrary optical functions such as focusing or aberration correction. Proposed AR systems include HOEs as optical combiners with a mirror lens function [152], optical combiners for viewing angle enlargement [153], optical combiners for eyebox duplication [101] or optical combiners for laser scanning systems [154]. A very common AR system configura-



tion uses two HOEs: one for in-coupling of light coming from a display into a waveguide, and one to out-couple the light in the users view [155, 156, 157, 158, 159, 160]. Other applications for volume holograms that have been investigated include HOEs as optical switches and interconnects in telecommunication networks or chip-to-chip communication [161, 162], HOEs for concentrators to increase solar cell energy yield [163, 164], holographic diffusers e.g. for light-field displays [165] or for color mixing in the back-light systems of cell phones [166] or security holograms [167, 168, 169, 170].

In summary, holography is a thriving field and recent innovations such as the Bayfol material or holographic printers have created a larger potential for innovation than what has been addressed in research so far.

### 1.2. Motivation and scope of this work

Transferring the recent success of holography in AR applications into other fields is scientifically interesting on its own right as motivated in the beginning of this chapter. But there are further specific reasons why incorporating holograms into spectacle lens designs is a promising endeavor.

Considering the advances in spectacle lens design methods in the last decades, it seems fair to state that classical spectacle lens design as choosing the shape of a refractive lens made from one of the known spectacle lens polymers does not promise significant performance improvements anymore. Therefore, spectacle lens design innovations are likely to include new technology, be it new materials, new coatings, manufacturing methods, electric components or diffractive components. For the purposes of this thesis, several limitations of spectacle lenses are worth evaluating for potential holography-based solutions. For example, the transversal color error of spectacle lenses scales with prescription power. If a user finds the color error of their high prescription spectacle lenses to be disturbing, the only practiced way of reducing color error so far is to use a material with less dispersion i.e. a higher Abbe number. Looking at the Abbe-diagram [171], for spectacle lens materials a higher Abbe number generally comes with a lower refractive index. Lowering the refractive index of a lens means that the curvatures need to be increased to achieve the same prescription power. Increased curvatures mean that the lens becomes thicker and heavier. This compromise between color error and weight is especially unfortunate because high prescription spectacle lenses are very heavy already.

Here, holography has the potential to leverage the concept of refractive-diffractive dis-



persion compensation [117] to reduce color error. An added benefit to this could be that holograms realize optical functions in thin films, which means a hybrid spectacle lens including holograms can be thinner and flatter than a refractive one of the same prescription. This is important not only for wearing comfort, but also for aesthetics, which are very important for the marketing of spectacle lenses. A further advantage of holograms is that their optical functions can be chosen almost arbitrarily, which allows aberration correction e.g. astigmatism reduction in a similar manner as e.g. aspherical surfaces or free-form surfaces. Another potential benefit of realizing arbitrary optical functions in thin holograms is that they could replace the free-form surface in progressive addition lenses. Due to the spatially varying power, progressive addition lenses require high precision manufacturing processes, which are usually based on computer-numerically controlled (CNC) machines with soft polishing instead of the easier hard polishing used for spherical lenses [172]. Even though cheaper processes such as compression molding are used for small elements like camera lenses or larger elements with lower accuracy requirements e.g. condenser lenses for projectors [173], they are not used for high-end spectacle lenses with individualized prescriptions. Here, holograms could be used to provide the same functionality as a free-form surface in a thin film.

However, besides the mentioned application advantages, using holograms in spectacle lens applications has several challenges that need to be overcome, such as diffraction efficiency or dispersion management. This thesis presents a tool chain that incorporates solutions to these challenges into a design method for holograms in spectacle lens applications. The upcoming Chapt. II prepares this by reviewing relevant theories and methods of spectacle lens design as well as holography. The focus in that chapter is on design methods for refractive spectacle lenses and methods for the calculation of hologram diffraction efficiency. Chapt. III builds upon these methods and presents the aforementioned design tool chain. The design tool chain incorporates solutions for high diffraction efficiency holograms and dispersion compensation into a method that allows to design holograms with arbitrary optical function that can be used for single vision spectacle lenses as well as progressive addition lenses. An important feature of this tool chain is to design holograms for all gaze directions of the eye. Chapt. IV presents several designs of either holographic or refractive-holographic hybrid single vision spectacle lenses as well as designs of holographic progressive addition lenses. These designs are compared to their refractive counterparts and it is evaluated whether or not the discussed benefits of including holograms in spectacle lens designs, such as dispersion compensation, thickness

reductions or replacement of progressive addition lens free-forms or aspheres, can be achieved in simulation. The findings of the design evaluations are then summarized in Chapt. V.

## II. Background

This chapter is to summarize important theories and methods in the fields of spectacle lens design and holography that are required to understand the following chapters. Sect. 2.1 is devoted to spectacle lens design, because the spectacle lens design method for HOE-based spectacle lenses presented in chapter III is best understood as an extension of design methods for refractive spectacle lenses. Sect. 2.2 is devoted to volume holography and starts with a brief discussion of the recording and wavefront reconstruction process to give a conceptual understanding of holography. Afterwards, methods to calculate hologram diffraction efficiency (DE) that are used in chapter III are presented. In this context, many of the relevant hologram parameters for the design method of HOE-based spectacle lenses are introduced.

### 2.1. Spectacle lenses

This section is to introduce the field of spectacle lens design, especially to readers whose background is in holography rather than spectacle lens design. First, the refractive errors of the eye that can be corrected by spectacle lenses such as myopia, hyperopia, astigmatism and presbyopia are introduced. The second subsection is devoted to the discussion of paraxial formulas for the design of single vision spectacle lenses (SVSLs), which aim at providing the user with a certain spherical power (SPH) and astigmatism (AST) that corrects the users myopia, hyperopia and astigmatism. But paraxial formulas only describe the optical performance of a SVSL for looking straight ahead, which is not sufficient as SVSLs are expected to correct the users vision for all gaze directions. Therefore, the next subsection discusses spectacle lens design methods that aim at reducing the deviations from the desired SPH and AST, here referred to as SPH error and AST error, for all gaze directions of the eye. In this context, the ability of aspheres (ASPHs) to reduce the combined error budget of SPH error and AST error is discussed for three sample SVSL designs. Because color error (CE) is important for the evaluation of the hologram-based spectacle

## II Background

---

lenses designed in this thesis, the CE calculation method is presented along with the CE results for the sample SVSLs. The last subsection discusses progressive addition lenses (PALs) that can be used to correct the refractive error of presbyopia and introduces a sample PAL design to illustrate their general functionality.

### 2.1.1. Refractive errors of the eye

Spectacle lenses are the most prevalent treatment options for refractive errors of the eye. Fig. II.1 visualizes the four most relevant ones. For reference, part (a) shows an emmetropic eye, i.e. an eye without any refractive errors in its optics i.e. the cornea and the eye lens. In that case, the optics of the eye image a distant object, which could be a e.g. a point source in a distance of more than 5 m, so that the focus lies directly on the retina. Deviations of the focus from the retina are referred to as refractive errors. Part (b) shows the refractive error myopia, which is also known as nearsightedness. In that case, the focus is placed in front of the retina, because of a combination of the eye ball being too long and the optics of the eye being too strong. Myopia can be corrected with a negative SPH SVSL. The opposite of myopia is hyperopia or farsightedness, which is shown in part (c). Here, the focus is placed behind the retina, which is caused by a combination of the eye ball being too short or the optics of the eye being too weak. Hyperopia can be corrected with a positive SPH SVSL. All refractive errors that lead to two foci for different meridians are referred to as astigmatism. Part (c) shows a sample configuration with a first focus  $F_1$  being placed in front of the retina, while a second focus  $F_2$  is placed behind the retina. This case is referred to as mixed astigmatism, but all other possibilities exist as well: simple myopic astigmatism (one focus on the retina, one in front of it), compound myopic astigmatism (both foci in front of the retina), simple hypermetropic astigmatism (one focus on the retina, one in behind it) and compound hypermetropic astigmatism (both foci behind the retina). The 2D figure does not specify the relationship between the two meridians shown as light and dark blue. If the principal meridians (steepest and flattest meridians) are perpendicular to each other, the astigmatism is referred to as regular. If the principal meridians are not perpendicular, the astigmatism is referred to as irregular [174]. Astigmatism can be corrected with an astigmatic SVSL.

The last relevant refractive error called presbyopia is shown in parts (e) and (f). Presbyopia is a age related stiffening process of the eye lens that does not affect viewing distant objects as shown in part (e). The problem is that for near objects, the human eye usually changes the curvature of the eye lens to "zoom in" by increasing the SPH of the

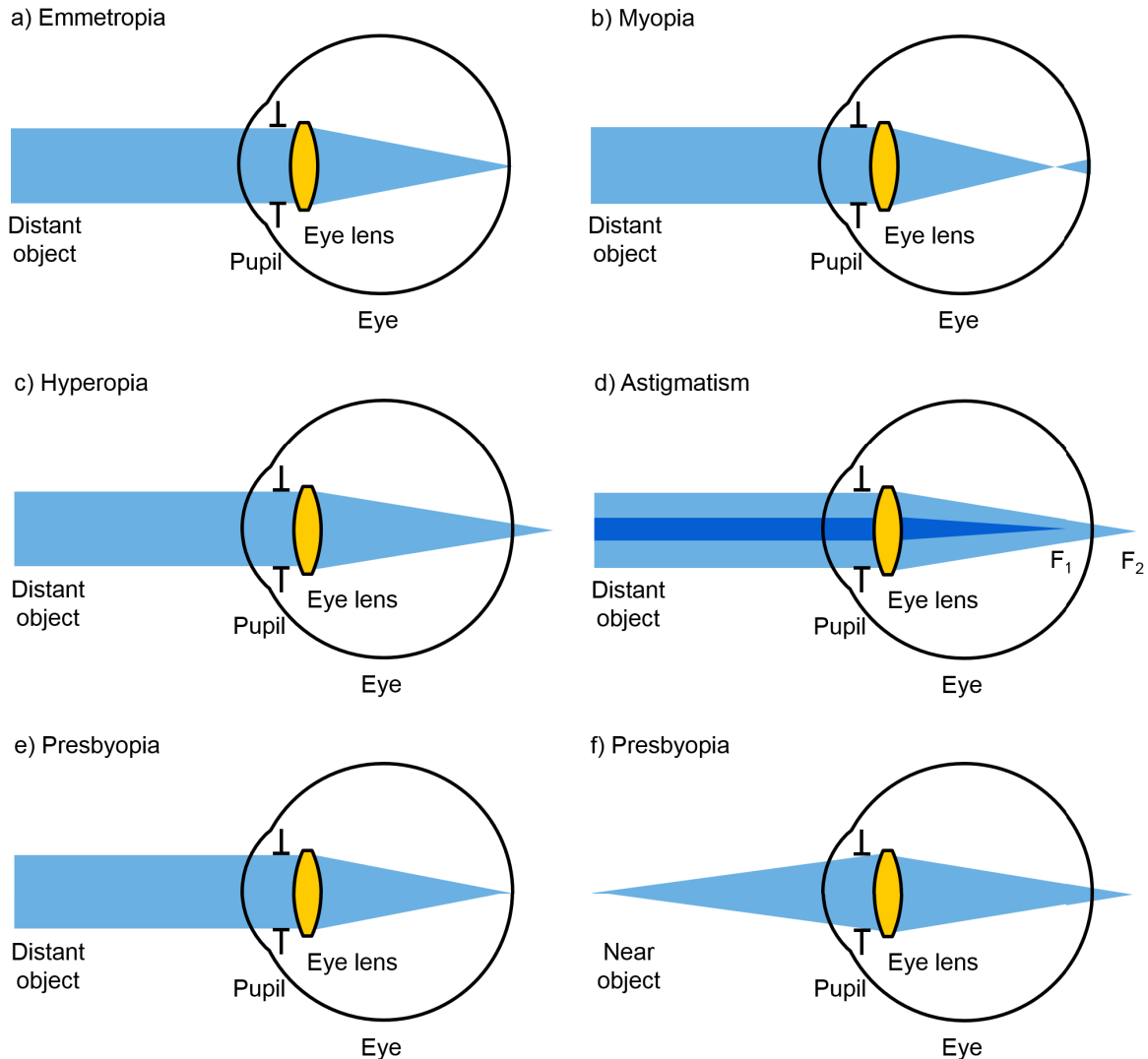


**Figure II.1.** Refractive errors of the eye. Emmetropia (a) is defined as the absence of refractive errors. In that case, the optics of the eye i.e. eye lens and cornea, image a distant object directly on the retina. In the case of myopia (b) the optics of the eye image a distant object in front of the retina, while in the case of hyperopia (c), the optics of the eye image a distant object behind the retina. Myopia and hyperopia can be caused by an inadequate combination of eye ball length and strength of the eye optics. Astigmatism (d) is a refractive error in which the irregular curvature of the optics of the eye creates two foci when imaging a distant object. In the figure, the second beam shown in the darker blue is meant to be on a different meridian than the light blue one. Presbyopia (e and f) is an age-related stiffening process of the eye lens that does not affect distant objects (e), but the eye lens is no longer capable to provide the additional SPH required to image near objects (f).

## II Background

---

optical system, which is referred to as accommodation. The SPH difference required is a function of object distance and known as add power. In a presbyopic eye, the eye lens became so stiff that it cannot or can only partially change its curvature to accommodate and provide the required add power to image near objects, which leads to the focus being behind the retina as shown in part (f). Presbyopia can be corrected by providing the required add power e.g. by reading glasses which are just SVSLs with positive SPH or bifocals, which correct the other refractive errors of the eye over the full lens surface and then provide the required add power in a small section of the lens. But both of these solutions provide only one fixed add power, which corrects for one fixed distance of a near object, but not the whole distance range as a natural accommodation process does. A continuous increase in add power to view near objects at variable distances is provided by PALs. The four refractive errors discussed here are the ones relevant to the contents of this thesis. Further technical aspects of special cases in spectacle lens design, e.g. the implications of distortion due to magnification variances between the two eyes and prism for binocular vision, are skipped here.

### 2.1.2. Paraxial formulas

For the on-axis position of the user looking straight through a spectacle lens, simple formulas can be derived from paraxial optics to describe the lens properties. Here, formulas that can be found in standard text books such as Ref. [175] are put into the context of this thesis. Even though off-axis performance is crucial in spectacle lens design, these paraxial formulas offer a good initial orientation when e.g. looking for suitable starting values for further optimization in an optical design software.

In the following, a spherical lens made from a material with refractive index  $n$  with front and back surface curvatures  $R_1$  and  $R_2$ , respectively, and center thickness  $D$  is considered. Fig. II.2 shows an illustration of such a lens in front of an eye. The optical power of this spectacle lens depends on the front and back surface powers. The front surface power  $P_1$  is given as

$$P_1 = \frac{n - 1}{R_1} \tag{II.1}$$

and the back surface power  $P_2$  as

$$P_2 = -\frac{n-1}{R_2}. \quad (\text{II.2})$$

The optical powers are usually expressed in diopters with  $\text{dpt} = 1/\text{m}$ . The full power of the lens  $P_{\text{full}}$  is then

$$P_{\text{full}} = P_1 + P_2 - \frac{D}{n}P_1P_2. \quad (\text{II.3})$$

The term including the lens thickness  $D$  can be neglected in many cases especially when calculating starting values for an optimization rather than a final design. E.g. for a lens with  $P_1 = 2$  dpt and  $P_2 = -6$  dpt,  $n = 1.5$  and  $D = 0.006$  m, which are realistic values for a spectacle lens, the term in question would take a value of 0.048 dpt, while the first two terms sum up to -4 dpt. According to Eq. II.3, a given prescription value can be realized by an infinite combination of front and back surface powers. This is true even when only considering meniscus shaped lenses, where both  $R_1$  and  $R_2$  take positive values. A prescription of -4 dpt, for example, can be realized by  $P_1 = 0$  dpt and  $P_2 = -4$  dpt,  $P_1 = 2$  dpt and  $P_2 = -6$  dpt or  $P_1 = 4$  dpt and  $P_2 = -8$  dpt. The implications of choosing a specific combination of front and back surface powers on off-axis gaze directions are discussed later in this chapter. Eq. II.3 relates the lens power to the principal plane. For spectacle lens design, it can be advantageous to relate the optical power to the back vertex plane, which is shown as a red line in Fig. II.2 since the location of the principal planes is not necessarily known. In that case, the back vertex power corresponds to the curvature of an incident plane wave after refraction by the spectacle lens. The back vertex power is then given as:

$$\text{SPH} = \frac{P_1}{1 - \frac{D}{n}P_1} + P_2 = \frac{P_{\text{full}}}{1 - \frac{D}{n}P_1}. \quad (\text{II.4})$$

In the following chapters, SPH and AST are always meant to describe back vertex powers.

These paraxial formulas can also be used to calculate the required power to view a close object. Ref. [175] states the required optical power for viewing a near distance object  $P_{\text{near}}$  as the sum of the back vertex power for viewing an object at infinity SPH and

## II Background

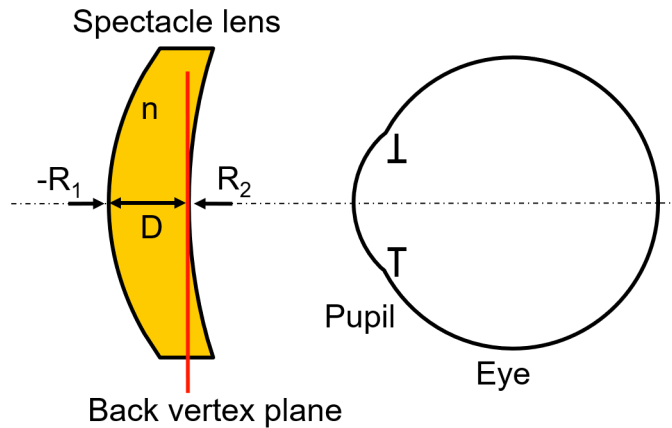


**Figure II.2.** A spherical spectacle lens can be described by the following parameters: refractive index  $n$ , front and back surface curvatures  $R_1$  and  $R_2$ , and center thickness  $D$ .

an additional term that depends on the magnification  $M$

$$P_{\text{near}} = \text{SPH} + \frac{M^2 P_1}{1 - \frac{D}{n} M P_1} = \text{SPH} + \text{add power.} \quad (\text{II.5})$$

The second term can be labeled the add power and is either contributed by accommodation of the eye or describes the required add power of a presbyopia correction vision aid such as a bifocal spectacle lens or a PAL. Since the magnification of a lens of a given prescription  $\text{SPH}_{\text{prescription}}$  depends on the object distance  $d_{\text{obj}}$  as

$$M = \frac{1}{1 - d_{\text{obj}} \text{SPH}_{\text{prescription}}}, \quad (\text{II.6})$$

the add power depends on the object distance.

### 2.1.3. Gazing eye problem

The refractive errors of the human eye can be assumed to be independent of gaze direction. This means that, if a given prescription corrects the refractive errors of the eye, the goal of spectacle lens design is to provide that prescription for all gaze directions of the eye. In spectacle lens design, it makes sense to evaluate this situation without taking into account the optics of the eye. If the optics of the eye are considered, the goal of spectacle lens design is to place the focus of incident ray bundles on the retina. If the optics of the eye are not considered, the goal is to place the focus on a sphere whose center coincides



with the rotational center of the eye, but whose radius differs from the eye radius. For objects at infinity, which are assumed e.g. for SVSL design, this sphere is called the far point sphere and its radius is  $1/\text{SPH}_{\text{prescription}}$ . If the focus of incident ray bundles is on the far point sphere this means that target prescription is achieved and the combination of the spectacle lens and the optics of the eye would place the focus on the retina. Using the paraxial formulas discussed above, it is possible to design spectacle lenses that place the focus on the far point sphere for the on-axis gaze direction. But for other gaze directions, different parts of the lens are used that at least in the case of spherical lenses do not provide the same optical function and therefore induce aberrations i.e. a combination of the two oblique errors. These oblique errors, here referred to as SPH error and AST error, are visualized in Fig. II.3 (a) and (b), respectively. SPH error denotes the case that there is an offset between the focus and the far point sphere. If there is uncompensated astigmatism in the spectacle lens design, there are two foci  $F_1$  and  $F_2$  and the circle of least confusion  $C$  between them as denoted in part (b) of the figure. If  $C$  is placed right on the far point sphere, there is no SPH error. The AST error is then given as the distance between the foci. It should be noted that to keep in line with the descriptions in the paraxial formulas SPH and AST are defined relative to the back vertex sphere for the off-axis gaze directions. This follows the same logic as relating them to the back vertex plane in the paraxial case, but ensures that all gaze directions are evaluated for the same conditions.

How much oblique aberrations, SPH error and AST error, are induced depends on the base curve of the lens i.e. which combination of front and back surface power is used to achieve the desired prescription. The goal of choosing a base curve can be to either minimize SPH error, AST error or to minimize both within certain error budgets.

While in general this problem is best addressed by optimization in an optical design software, it should be noted that in some cases analytical formulas allow calculating favorable solutions that in turn can be used as initial values for an optimization. The Tscherning ellipse, for example, describes analytical solutions with vanishing AST error for a large range of prescriptions provided that only a small range of gaze directions is considered and that the thin-lens approximation is valid. The starting point for these considerations are Coddington's equations, which can be used to calculate the meridional and sagittal foci for any given ray and an infinitesimal close neighboring ray coming from the same object point [176]. Expressing the refraction on the front and back surface using Coddington's equations and then asking for the astigmatism to vanish, i.e. for the

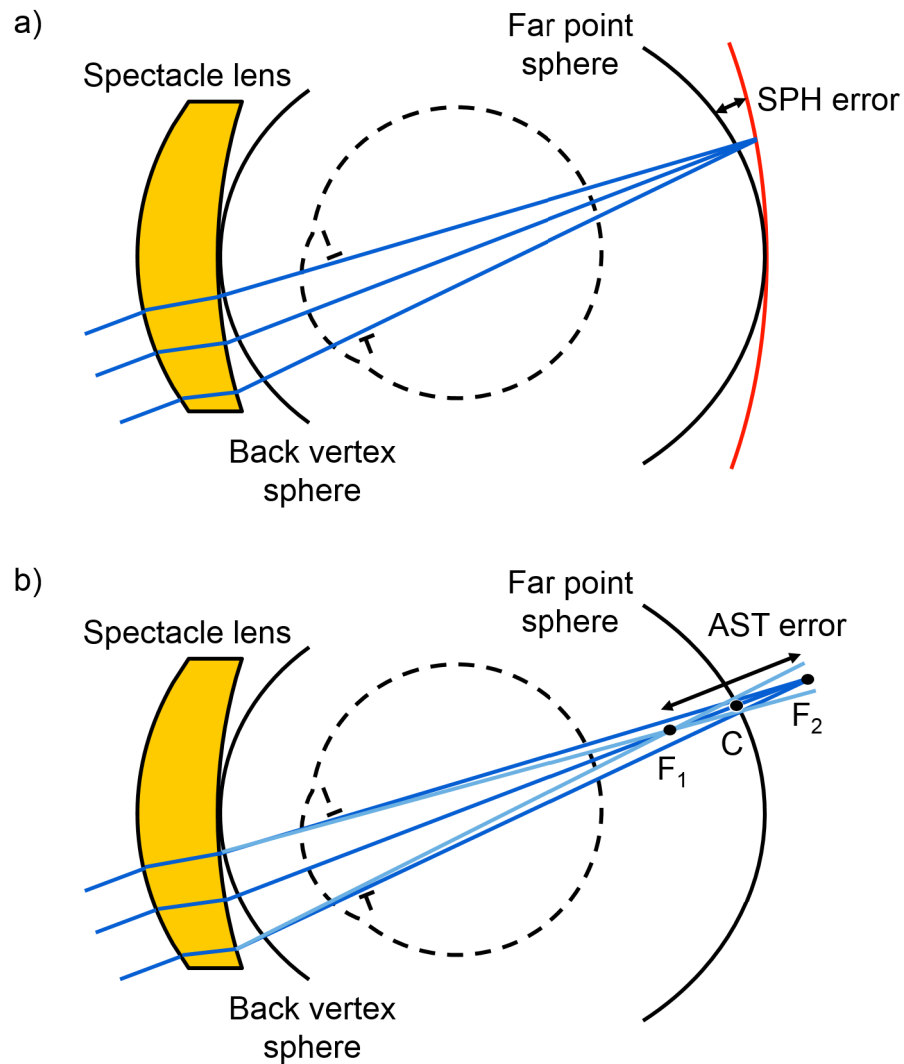


**Figure II.3.** SPH error (a) and AST error (b) are oblique errors occurring for off-axis gaze directions of the eye through a spectacle lens. If the focus is placed on the far point sphere, the combination of the spectacle lens and the optics of the eye places the focus on the retina for an object at infinity. Deviations of the focus from the far point sphere are referred to as SPH error. If the focus is split up into a meridional and sagittal focus, but the circle of least confusion is placed on the far point sphere, there is no SPH error, but AST error equal to the displacement of the foci.

meridional and sagittal foci to coincide, yields the equation for the Tscherning ellipse as

$$(n+2)P_2^2 + \left[ 2(n^2-1)\left(\frac{1}{a} - \frac{1}{s}\right) - (n+2)P_{\text{full}} \right] P_2 + \left[ \left( nP_{\text{full}} - \frac{2(n-1)}{a} \right) \left( \frac{1-n^2}{s} + P_{\text{full}} \right) + \frac{n(n-1)^2}{a^2} \right] = 0 \quad (\text{II.7})$$

with  $a$  being the distance between the lens and the rotational center of the eye and  $s$  being the distance between the lens and the object. Equations for the Tscherning ellipse can also be found in more complicated scenarios such as a larger range of valid gaze directions, finite lens thicknesses or aspherical surfaces, but in these cases no analytical solutions are available and the equations can only be solved numerically [175].

The alternatives to analytical spectacle lens design methods such as the Tscherning ellipse are optimization procedures in optical design software. The general approach there is to define an optical system with variable parameters in an initial configuration and to then vary these parameters until a merit function describing the system's performance is minimized. The main challenge of spectacle lens design in an optical design software is that most optical systems have only one optical axis and a fixed aperture. A camera objective lens, for example, is designed under the assumption that a certain angular spectrum around the optical axis is transferred through the optical system and limited by the objective's aperture. This is different from spectacle lenses, where the aperture is the pupil of the eye that moves around between different gaze directions. One way of describing this is to consider each gaze direction of the eye as its own optical system configuration with the pupil of the eye being the system aperture and the current optical axis being given by connecting the center of the pupil and the rotational center of the eye  $M$ . Fig. II.4 shows two sample gaze directions in parts (a) and (b) and a discrete sampling of the full angular range of principal rays within the field of view of the spectacle lens in parts (c). This is typically solved by writing a merit function, which is minimized by varying a given set of lens parameters such as front and back curvatures  $R_1$  and  $R_2$ , refractive index  $n$  of the lens material, center thickness  $D$  or possibly additional coefficients describing an aspheric or free-form surface. The merit function needs to include contributions of principal rays sampling the entire field of view of the spectacle lens in order to achieve good off-axis performance. Because it might not be possible to achieve the desired performance for the entire field of view, it is important to weight the contributions of different principal rays to the merit function. E.g. in the case of radially symmetric designs such as SVSLs, it makes sense to assign radially decreasing weights to ensure that the desired prescription

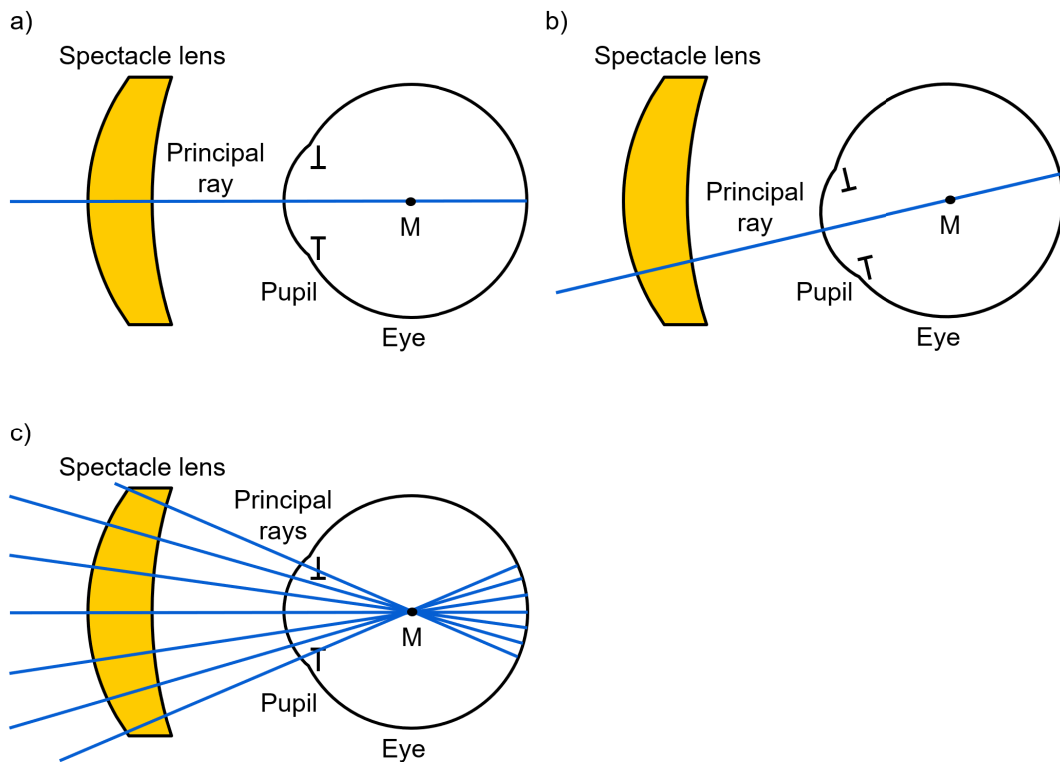


**Figure II.4.** Visualization of the principal rays of different gaze directions. Principal rays are constructed by connecting the rotational center of the eye  $M$  with the center of the pupil. Parts (a) and (b) show the principal rays of the on-axis (a) and an off-axis (b) gaze direction. Part (c) shows a discrete sampling of the principal rays within the field of view of the spectacle lens.

values are achieved in the center and slight errors are accepted in the outer parts of the SVSL. In addition to terms evaluating the optical performance of the lens in terms of SPH error and AST error, the merit function can include terms concerning other properties like the lens center or edge thickness. Another challenge of optimizing spectacle lenses in an optical design software is to find a good initial system so that the optimization converges to a local minimum of the merit function that corresponds to a final optical system with the required optical performance. In spectacle lens design, this is often done by calculating lens parameters that achieve desired prescription for the on-axis gaze direction, for example using e.g. Eq. II.4 or II.7.

### 2.1.4. Aspheres

The optimization compromise between SPH error, AST error and lens thickness discussed above can be further improved by using ASPHs. To showcase the potential of ASPHs, a

SVSL with a prescription of -4 dpt SPH at 0 dpt AST realized as a spherical lens is compared to two designs with the same prescription and ASPHs to improve the optimization compromise. The spherical lens is chosen out of the available list of semi-finished lenses from Zeiss and has the following geometry:  $R_1 = 200$  mm,  $R_2 = 85.5$  mm,  $D = 1.2$  mm. The lens material is a standard polymer for spectacle lenses with a refractive index  $n$  of 1.59 and an Abbe number  $V_d$  of 41.11. Consequently, the front surface power  $P_1$  is 2.95 dpt, the back surface power  $P_2$  is -6.95 dpt and, neglecting thickness, the expected prescription value is -4 dpt SPH. This lens is not chosen according to the Tscherning ellipse for compensated astigmatism, but rather to satisfy a compromise of SPH error, AST error and lens form in terms of thickness and flatness. The latter two are important since the commercial success of spectacle lenses is influenced by the aesthetics as well as the optical properties.

Fig. II.5 (a), (b) and (c) show the SPH error, AST error and CE, respectively, over the lens surface of the spherical lens with the prescription of -4 dpt SPH at 0 dpt AST. CE is discussed in the later in this section and can be ignored for the time being. The values shown in these plots can be understood as follows: the optical properties of the lens SPH error, AST error and CE are evaluated for a discrete sampling of gaze directions covering the entire lens surface. Therefore, each pixel in the plot corresponds to the result of a bundle around the principal ray that corresponds to the current gaze direction. The performance of the spherical SVSL shown in Fig. II.5 (a)-(c) was optimized by choosing the base curve i.e. the lens curvatures. Altering the base curve would decrease either SPH error or AST error while increasing the other. Using ASPHs, however, can improve the optimization compromise as a whole. For example, the aspherical SVSL shown in Fig. II.5 (d)-(f) has a slightly reduced SPH error and strongly reduced AST error, compared to the spherical SVSL shown in Fig. II.5 (a)-(c). But even with ASPHs, it is not possible to completely remove SPH error and AST error. The aspherical SVSL in Fig. II.5 (g)-(i) illustrates what happens when trying to decrease SPH error below the level of the aspherical SVSL shown in Fig. II.5 (d)-(f). Here, SPH error decreases are achieved only by strongly increasing AST error. In other words, ASPHs reduce the error budget, but trade-offs between SPH error and AST error remain.

### 2.1.5. Color error

When evaluating the optical performance of a spectacle lens in this thesis, three quantities are reported: SPH error, AST error and CE. The first two have been introduced in Fig. II.3

## II Background

---

already and are standard quantities in spectacle lens design. CE is usually not considered in spectacle lens design as its impact on the users vision depends on individual factors and there are no ways to significantly reduce CE by refractive means outside of choosing materials with low dispersion i.e. a high Abbe number  $V_D$ . If CE is calculated in refractive spectacle lens design, it is typically done using an approximate formula based on the Abbe number:

$$CE_{\text{ref}} = \frac{h \text{ SPH}}{V_D} \quad (\text{II.8})$$

with  $h$  denoting the considered height on the lens i.e. the distance from the lens center that corresponds to the gaze direction of looking straight ahead. The human perception threshold for CE calculated with Eq. II.8 is reported as 0.12 cm/m in Ref. [177]. This means that, when looking at a black object on a white screen in 2 m distance, the user of a spectacle lens inducing a CE of 0.12 cm/m would see 0.24 cm thick color fringes around the edges of the object. Eq. II.8 is based on the Abbe number and therefore not applicable for diffractive HOE tandems investigated in this thesis. Therefore, in this thesis, CE is calculated as the direction difference between a red ( $\lambda = 620$  nm) and a blue ray ( $\lambda = 430$  nm) in the pupil of the eye and scaled with the airy disc of a the green center wavelength ( $\lambda = 546$  nm). Since the absolute value of this calculation can not be interpreted, all CE described in this thesis are normalized so that the CE of the spherical lens shown in Fig. II.5 (c) at a height of 30 mm is one. This CE is known to be uncritical from practice, even though it is above the perception threshold. The perception threshold of 0.12 cm/m corresponds to a normalized CE of 0.4. The CE of the spherical and two aspherical SVSLs shown in Fig. II.5 (c), (f) and (i), respectively, illustrates that the introduction of ASPHs has negligible effect on CE.

### 2.1.6. Progressive addition lenses

PALs are used to correct the refractive error of presbyopia by replacing the "zoom" function of the accommodating eye by varying their SPH over the lens surface. The upper part of the PAL typically has a fixed SPH and AST prescription that corrects the refractive errors other than presbyopia for viewing a distant object as it is the case with SVSLs. In the following, it is assumed that there are no other refractive errors and consequently, the upper part of the PAL has a prescription of 0 dpt SPH and 0 dpt AST. In the lower part of the PAL, the curvature increases to increase SPH. The SPH increase relative to the part

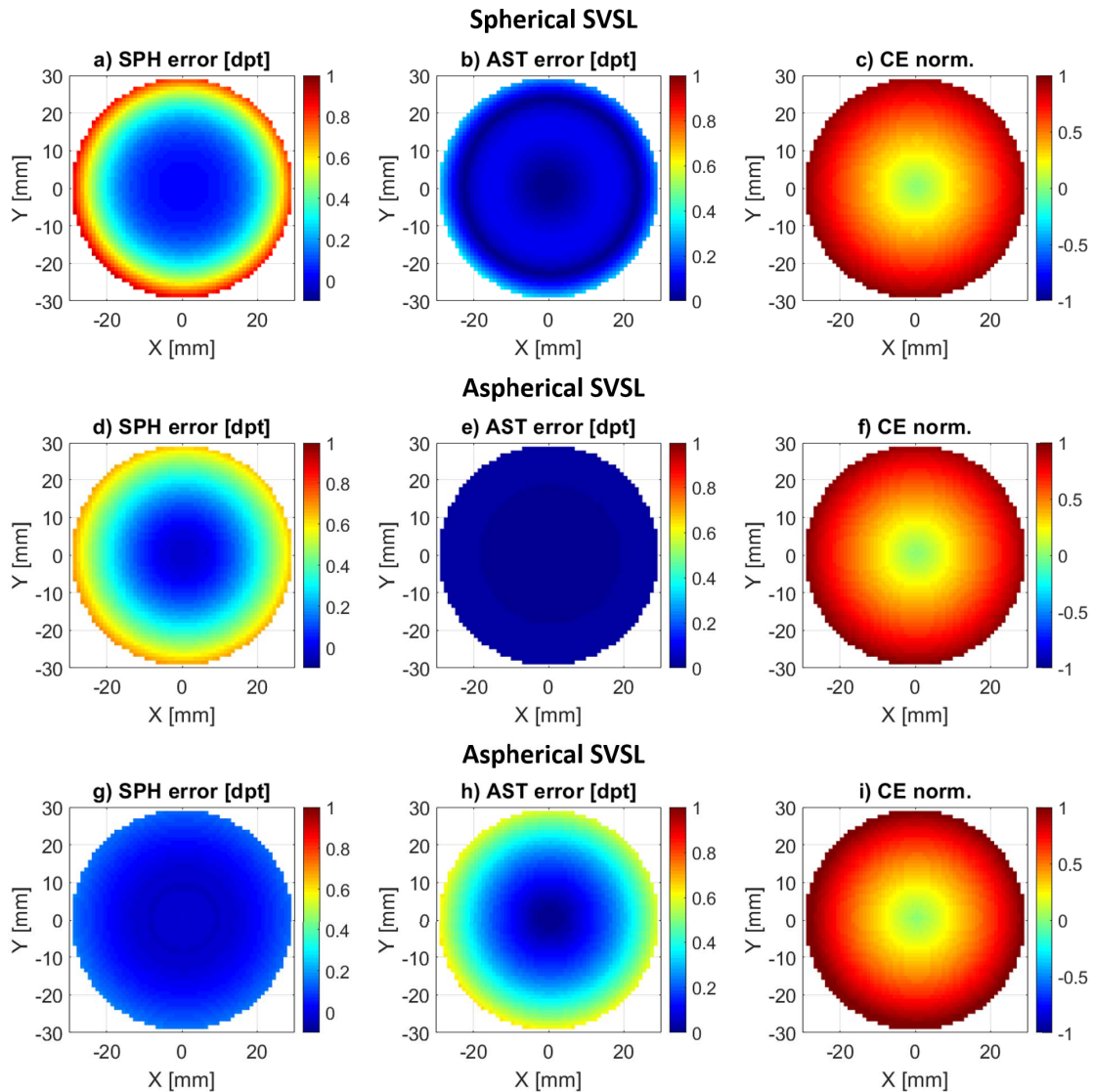


**Figure II.5.** SPH error (a), AST error (b) and CE (c) over the lens surface of a SVSL with a prescription of -4 dpt SPH and 0 dpt AST realized as a spherical lens. The performance can be improved by introducing an asphere to one surface. The design shown in (d)-(f) is optimized to minimize AST error and achieves a lower AST error than the spherical lens while also reducing SPH error. The design shown in (g)-(i) is optimized to minimize SPH error, which is strongly reduced at the cost of increasing AST error. Both ASPHs have no notable influence on CE.

## II Background

---

used for viewing distant objects is called the add power. Because the SPH increase is smooth, the user can select the required add power for viewing near objects by choosing the gaze direction which uses the correct lens area. In practice, this can require some head movements.

The SPH distribution of an ideal PAL, i.e. the desired functionality from an application point of view, designed for an add power of up to 2 dpt is shown in Fig II.6 (a). The upper half of the lens at  $Y > 0$  mm has 0 dpt SPH, i.e. the curvatures of the front and back surface are similar. This zone can therefore be used for viewing distant objects without any required add power. In the lower part of the lens, one surface curvature then varies so that SPH is smoothly increased up to the desired add power of 2 dpt. The lower part of the lens at  $Y < -18$  mm can then be used for viewing near objects, while the both zones are connected by a transition zone that allows intermediate distance objects to be viewed with the required add power. For users with additional refractive errors other than presbyopia, the SPH distribution shown in part (a) would be added to the SVSL that corrects the other refractive errors. For example, if the user requires a SVSL with a prescription of -4 dpt SPH to correct myopia, the SPH distribution goes from -4 dpt to -2 dpt, which would be expressed as a -4 dpt SPH PAL with 2 dpt of add power. In the ideal case, the lens would not have any non-prescription AST as indicated in part (b). However, Minkwitz theorem

$$\frac{\partial \text{AST}}{\partial x} = 2 \frac{\partial \text{SPH}}{\partial y} \quad (\text{II.9})$$

describes that spatial variations of SPH along one direction cause spatial variations of AST at twice the rate in the perpendicular direction [26, 27]. Because zones with high levels of unwanted AST severely impair imaging performance, PAL design is a complicated process that mainly focuses on achieving large zones that are free of unwanted AST. A real PAL, whose SPH and AST distributions are shown in Fig. II.6 (c) and (d) therefore looks very different from the ideal one shown in parts (a) and (b). The example PAL shown in parts (c) and (d) is created using data by courtesy of Carl Zeiss Vision GmbH. The design is best understood by considering the AST distribution in (d) first. Only regions with close to 0 dpt AST can be used for unblurred imaging, which leaves the upper part of the lens, a small zone at the bottom of the lens and a thin corridor connecting the two zones. The regions of high AST, sometimes referred to as the blending regions, have high AST even above 2 dpt. The role of the zones with close to 0 AST is best understood by considering



the SPH plot in (c). The upper zone at  $Y > 0$  mm has 0 dpt SPH and 0 dpt AST, which is equivalent to the ideal PAL shown in parts (a) and (b). This zone is called the far zone and for viewing distant objects. The red zone in the SPH plot is the near zone for viewing near objects with 2 dpt SPH. This zone does not extend as far in X as it does in the ideal PAL, which is a concession for minimizing AST. The near and far zone are connected by a slim zone referred to as the progressive corridor. The small size of the progressive corridor is the main drawback of PALs [178, 172].

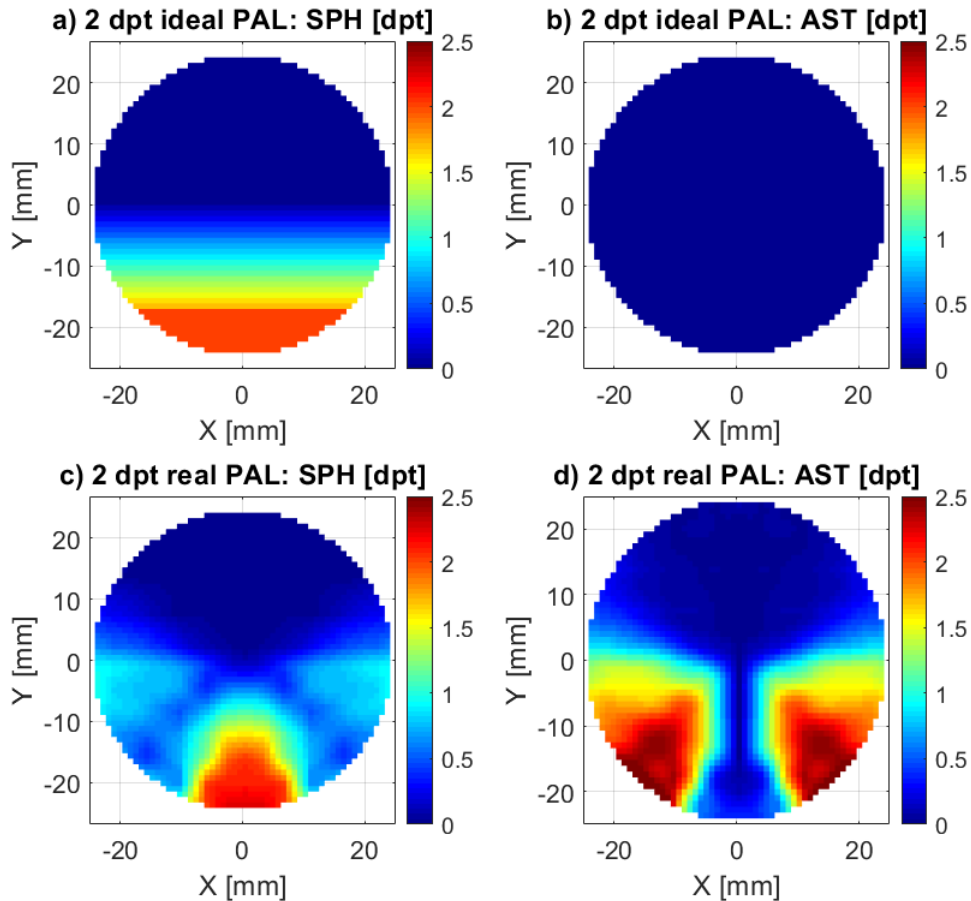


**Figure II.6.** SPH (a) and AST (b) distribution over the lens surface of an ideal PAL, i.e. the desired functionality for an application point of view. This ideal PAL would provide a zone for viewing distant objects with 0 dpt SPH at  $Y > 0$  mm, a zone for viewing near objects with 2 dpt SPH at  $Y < -18$  mm and a smooth transition zone in between, all at 0 dpt AST. But as described by Minkwitz theorem, increasing SPH along one direction also increases AST perpendicular to it, which makes it impossible to fabricate such an ideal PAL. Parts (c) and (d) show a real PAL design, which aims at achieving large AST-free zones despite of Minkwitz theorem. While the zone for viewing distant objects in the upper part of the real PAL is very similar to the one of the ideal PAL, the zone for viewing near objects is significantly smaller in X direction. This is an optimization compromise to increase the size of the transition zone referred to as the progressive corridor.

## 2.2. Volume holography

This section is to give a brief overview of holography, especially for readers whose background is in the field of spectacle lenses rather than holography. First, the wavefront reconstruction principle of holography is introduced in an adaptation from standard textbooks [179] because it provides a good framework to understand potential applications of holograms. For imaging applications such as spectacle lenses, it is important that holograms allow high diffraction efficiency (DE) operation in a single diffraction order. Therefore, the second subsection discusses DE calculation methods based on two well-known papers [92, 93]. Afterwards, a subsection is devoted to holograms in optics design, a topic which is treated in a lot more detail later in chapter III. Finally, the fabrication of arbitrary hologram structures is discussed to motivate that the holograms designed in this thesis can be fabricated even in mass production.

### 2.2.1. Wavefront reconstruction

Holography as a wavefront reconstruction technique is best explained by describing the recording and wavefront reconstruction process of image holograms. The following puts the wavefront reconstruction formalism found in standard textbooks [179] into the context of this thesis.

Image holograms are recorded as the interference pattern between a reference wave and an object wave. This process is shown in Fig. II.7 (a). For the purpose of explaining wavefront reconstruction, the thickness of the photosensitive material is not relevant and the hologram can be assumed to exist in a thin plane  $z_1$ . The thickness of the hologram, here indicated as  $z_1 \dots z_n$ , plays a major role in determining DE, which is discussed after the wavefront reconstruction. The following formalism is presented for  $z_1$ , but could be repeated for any  $z_n$  with the same results. The reference wave is typically chosen as a plane wave, because it is required to reproduce the reference wave later in the reconstruction step. The complex amplitude of the reference wave in the hologram plane  $z_1$  is given as

$$r(x, y) = r e^{ik \sin \theta x} \quad (\text{II.10})$$

with  $\theta$  being the angle of the reference wave to the propagation axis  $z$ . For in-line holograms,  $\theta$  is zero, but here  $\theta$  is assumed to be non-zero to treat the general case of off-axis

## II Background

---

holograms. The object wave is the light scattered from the object that is to be displayed by the image hologram. The complex amplitude of the object wave in the hologram plane  $z_1$  can therefore be formulated as

$$o(x, y) = |o(x, y)|e^{-i\phi(x, y)}. \quad (\text{II.11})$$

In the hologram recording process, the object wave  $o(x, y)$  and the reference wave  $r(x, y)$ , who are mutually coherent, are overlapped on a sheet of photosensitive material. There, their interference pattern is recorded. The interference pattern of the object wave and reference wave in the hologram plane  $z_1$  is then

$$\begin{aligned} I(x, y) &= |r(x, y) + o(x, y)|^2 \\ &= |r(x, y)|^2 + |o(x, y)|^2 + r|o(x, y)|e^{-i\phi(x, y)}e^{-ik\sin\theta x} + r|o(x, y)|e^{i\phi(x, y)}e^{ik\sin\theta x} \\ &= r^2 + |o(x, y)|^2 + 2r|o(x, y)|\cos[k\sin\theta x + \phi(x, y)]. \end{aligned} \quad (\text{II.12})$$

After chemical fixation steps and curing, the photosensitive material with the recorded interference pattern is called a hologram. For wavefront reconstruction, the hologram is illuminated by the reference wave as shown in Fig. II.7 (b). The amplitude transmittance of the hologram can be assumed as

$$t(x, y) = t_0 + \beta TI(x, y) \quad (\text{II.13})$$

with  $t_0$  being a constant background transmittance,  $T$  being the exposure time of the hologram and  $\beta$  being a parameter determined by the holographic material. Substituting Eq. II.12 into Eq. II.13 yields

$$t(x, y) = t_0 + \beta T[r^2 + |o(x, y)|^2 + ro(x, y)e^{-ik\sin\theta x} + ro(x, y)^*e^{ik\sin\theta x}] \quad (\text{II.14})$$

with  $o(x, y)^*$  denoting the complex conjugate of  $o(x, y)$ . When illuminating the hologram with the reference beam  $r(x, y)$ , the complex amplitude of the transmitted wave is then

$$u(x, y) = r(x, y)t(x, y) = u_1(x, y) + u_2(x, y) + u_3(x, y) + u_4(x, y) \quad (\text{II.15})$$

with

$$\begin{aligned}
 u_1(x, y) &= r e^{ik \sin \theta x} (t_0 + \beta Tr^2) \\
 u_2(x, y) &= \beta Tr |o(x, y)|^2 e^{ik \sin \theta x} \\
 u_3(x, y) &= \beta Tr^2 o(x, y) \\
 u_4(x, y) &= \beta Tr^2 o(x, y)^* e^{i2k \sin \theta x}.
 \end{aligned} \tag{II.16}$$

The first term  $u_1(x, y)$  is the directly transmitted reference wave, which is attenuated by a constant factor. The second term  $u_2(x, y)$  forms a halo surrounding the reference wave. The third term  $u_3(x, y)$  is the attenuated object wave and corresponds to the virtual image. The fourth term  $u_4(x, y)$  is the complex conjugate of the attenuated object wave and corresponds to the real image. The additional  $e^{i2k \sin \theta x}$  phase of the fourth term shows that the real image is deflected by  $2 \sin \theta$  in  $k$  space. As shown in Fig. II.7 (b), in the general case of off-axis holograms the components of the transmitted wave propagate in different directions. For a sufficiently large  $\theta$ , either the real or the virtual image can be filtered out e.g. by a spatial filter. This allows to create the high quality, monochrome image holograms that are known e.g. from museums.

The wavefront reconstruction process of holographic optical elements (HOEs) works analogous to the one of image holograms. The only difference is that the object wave  $o(x, y)$  and reference wave  $r(x, y)$  are typically a combination of spherical waves or plane waves. For example, a lens-type HOE can be realized as the interference pattern between either two spherical waves or a spherical wave and a plane wave (spherical wave that originates from infinity). For lens-type transmission HOEs, both waves come from the same side. For mirror-type or reflection HOEs, the waves come from opposing sides. Since the HOEs for spectacle lens applications discussed in this thesis are lens-type HOEs, the HOE recording and wavefront reconstruction process is illustrated using a lens-type HOE in Fig. II.8.

### 2.2.2. Diffraction efficiency

A key parameter to consider when designing optical systems that include holograms is DE. DE describes how much energy of an incident wave is transferred to the desired diffracted wave. Diffraction efficiencies can be calculated by solving Maxwell's equations for a plane wave incident on a film of holographic material in which an interference pattern has been recorded as a modulation of the refractive index in the volume of the holographic mate-

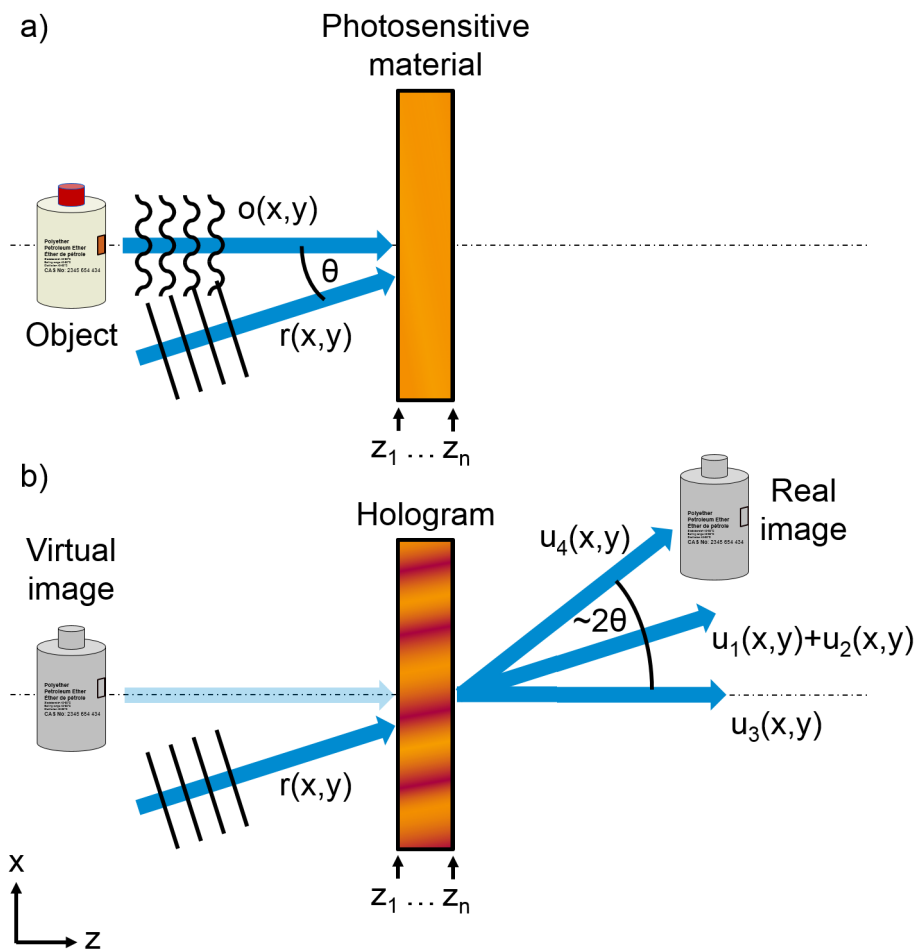


**Figure II.7.** Recording (a) and wavefront reconstruction (b) of an image hologram. The image hologram is created by writing the interference pattern of an object wave  $o(x, y)$ , which is the light scattered from an object, and a reference wave  $r(x, y)$ , which is a plane wave at angle  $\theta$ , into a photosensitive material. After development and fixation of the interference pattern, the photosensitive material is a hologram. Illuminating the hologram with the reference wave in the wavefront reconstruction step leads to the creation of a transmitted wave with four components:  $u_1(x, y)$  is the directly transmitted reference wave,  $u_2(x, y)$  is a halo surrounding  $u_1(x, y)$ ,  $u_3(x, y)$  is a virtual image of the recorded object and  $u_4(x, y)$  is a real image of the recorded object. The spatial separation between the components of the transmitted wave allows to filter out e.g. the real or virtual image. The thickness of the hologram, here indicated as  $z_1 \dots z_n$ , is not relevant for the wavefront reconstruction process, but plays a major role for DE.

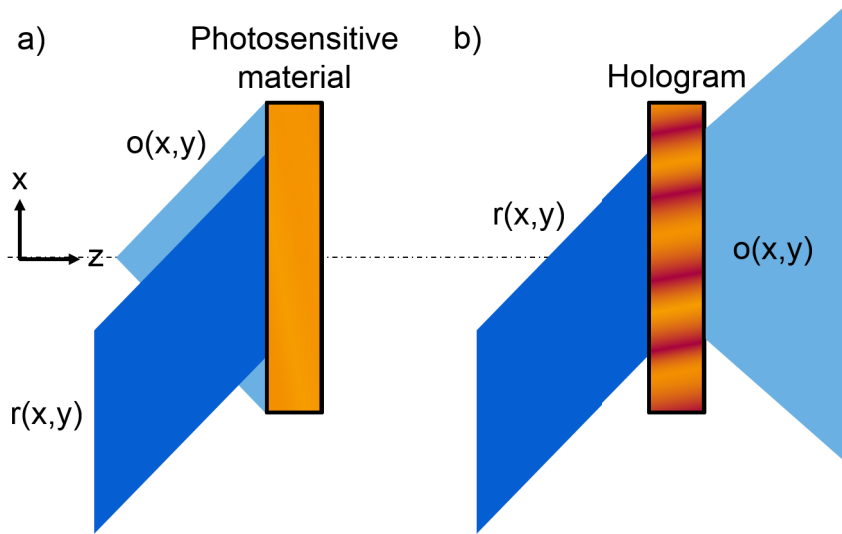


**Figure II.8.** Recording (a) and wavefront reconstruction (b) of a lens-type HOE. The HOE is recorded as the interference pattern of a spherical wave  $o(x,y)$  and a plane wave  $r(x,y)$ . Illuminating the HOE with either of these waves in the wavefront reconstruction process recreates the other one. This is shown here for the plane wave being used to recreate the wavefront of the spherical wave.

rial. The resulting amplitudes of the diffracted waves then give the diffraction efficiencies for the diffracted orders which allow to predict experimental results. Many theories have been developed that differ in choosing the integral or differential form of Maxwell's equations as a starting point, assuming depletion or no depletion of the incident wave and giving either rigorous or approximate solutions [80]. The discussion presented here focuses on two theories, Kogelnik theory and the Rigorous Coupled Wave Analysis (RCWA). The former dates back to a classic paper [92] and is up to today the most widely used approximate theory used to calculate hologram DE. The latter is a rigorous theory, which is mathematically equivalent to Fourier modal method (FMM) and was first applied to slanted holograms by Moharam and Gaylord [93].

### Coupled wave equations

Both methods to calculate hologram diffraction efficiencies that are presented here rely on solving the coupled wave equations. The coupled wave equations can be derived starting from the scalar wave equation, which describes the propagation of waves through a hologram. The scalar wave equation, which is valid for linear polarization and weak refractive index modulations [181], is known to be

$$\nabla^2 E + k^2 E = 0. \quad (\text{II.17})$$

## II Background

---

For the sake of simplicity, it is usually assumed that locally the hologram is a periodic structure that is independent of  $y$ . Consequently,  $E$  can be assumed the complex amplitude of the  $y$ -component of the electric field  $E(x, z)$ , which is independent of  $y$ . Calculating the DE of an image hologram that varies across  $y$  then is done by partitioning the hologram into small regions in which the local approximation is valid. The modulation of the refractive index inside of the volume of the hologram can be described using propagation constant  $k(x, z)$ , which depends on the relative dielectric constant  $\epsilon(x, z)$  and the conductivity of the hologram  $\sigma(x, z)$  as

$$k^2 = \frac{\omega^2}{c^2} \epsilon - i\omega\mu\sigma \quad (\text{II.18})$$

The distributions of  $\epsilon(x, z)$  and  $\sigma(x, z)$  in the volume of the hologram can be found by considering the recording process. In the general case that includes holographic optical elements (HOEs) and not just the previously discussed image holograms, a hologram is recorded as the interference pattern of two arbitrary waves. Locally, this can be approximated as the interference between two plane waves with wave vectors  $\vec{k}_R$  and  $\vec{k}_S$  as  $R(x, z) = Re^{-i\vec{k}_R \vec{r}}$  and  $S(x, z) = Se^{-i\vec{k}_S \vec{r}}$  that are both independent of  $y$ . Calculating the resulting intensity of the interference pattern analogous to Eq. II.12 leads to

$$I(x, z) = R^2 + S^2 + 2RS \cos((\vec{k}_R - \vec{k}_S) \vec{r}) \quad (\text{II.19})$$

The cosine term in Eq. II.19 describes an intensity modulation that causes a modulation of the refractive index in the recording process. The term can be used to define the local grating vector in the volume as

$$\vec{K}_{\text{vol}} = \vec{k}_R - \vec{k}_S. \quad (\text{II.20})$$

The volume grating period in the volume  $\Lambda_{\text{vol}}$  found as

$$\Lambda_{\text{vol}} = \frac{2\pi}{|\vec{K}_{\text{vol}}|} \quad (\text{II.21})$$

then is the distance between two maximums of the modulation of the refractive index in the hologram. The relationship between  $\vec{K}_{\text{vol}}$ ,  $\vec{k}_S$  and  $\vec{k}_R$  is also visualized in the Ewald sphere shown in Fig. II.9 (a). The resulting hologram parameters are shown in Fig. II.9 (b). For the local approximation described earlier, each part of a hologram can be



described by its local grating vector  $\vec{K}_{\text{vol}}$  with volume grating period  $\Lambda_{\text{vol}}$  and slant angle  $\phi$  between the local grating vector and the  $z$ -axis. In the general case, the modulation of the refractive index induced by the modulation of the intensity of the interference pattern can be expressed as a modulation of the dielectric constant  $\epsilon(x, z)$  as well as the conductivity  $\sigma(x, z)$  as

$$\begin{aligned}\epsilon(x, z) &= \epsilon_0 + \epsilon_1 \cos(\vec{K}_{\text{vol}} \vec{r}) \\ \sigma(x, z) &= \sigma_0 + \sigma_1 \cos(\vec{K}_{\text{vol}} \vec{r}).\end{aligned}\tag{II.22}$$

In the case of phase holograms, only  $\epsilon$  is modulated and in the case of absorption holograms, only  $\sigma$  is modulated. Eq. II.18 and Eq. II.22 can be combined to express the propagation constant in the grating as

$$k^2 = \beta^2 - 2i\alpha\beta + 2\kappa\beta(e^{i\vec{K}_{\text{vol}} \vec{r}} + e^{-i\vec{K}_{\text{vol}} \vec{r}})\tag{II.23}$$

where  $\beta$  is the average propagation constant and  $\alpha$  is the average absorption constant and  $\kappa$  is the coupling constant:

$$\begin{aligned}\beta &= \frac{2\pi}{\lambda} \sqrt{\epsilon_0} \\ \alpha &= \frac{\mu c \sigma_0}{2\sqrt{\epsilon_0}} \\ \kappa &= \frac{1}{4} \left( \frac{2\pi}{\lambda} \frac{\epsilon_1}{\sqrt{\epsilon_0}} - \frac{i\mu c \sigma_1}{\sqrt{\epsilon_0}} \right)\end{aligned}\tag{II.24}$$

For low absorption and low modulation of  $\epsilon$  and  $\alpha$  the following approximations can be used:

$$\begin{aligned}\beta &= \frac{2\pi n}{\lambda} \\ \kappa &= \frac{\pi n_1}{\lambda} - i \frac{\alpha_1}{2}\end{aligned}\tag{II.25}$$

with  $n$  denoting the average refractive index and  $n_1$  and  $\alpha_1$  denoting the amplitude of the spatial modulation of  $n$  and  $\alpha$ , respectively. The coupling constant describes how strongly the modulation of the refractive index of the hologram couples an incident wave to a diffracted wave. Inserting Eq. II.23 into Eq. II.17 yields the wave equation for the

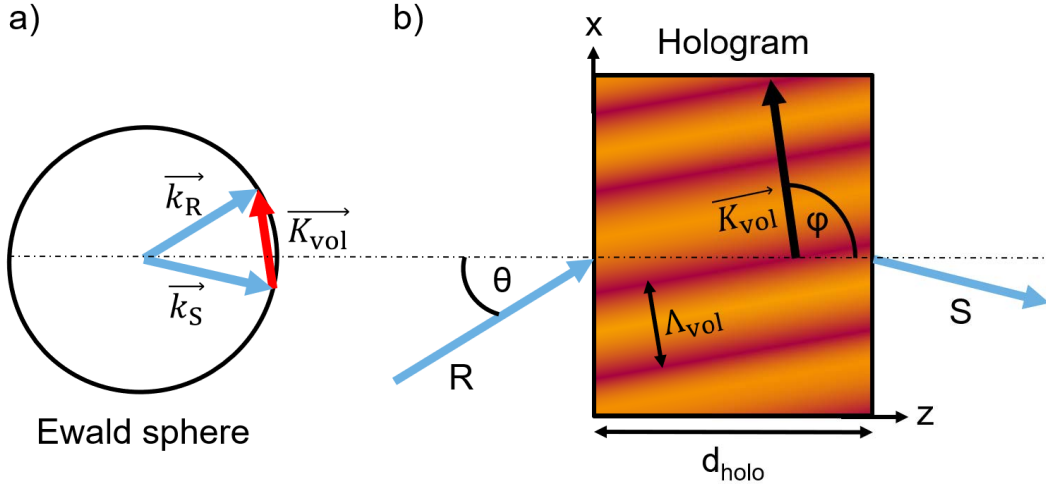


**Figure II.9.** Part (a) shows the wave vectors of a reference wave  $\vec{k}_R$  and a signal wave  $\vec{k}_S$  obeying the Bragg condition with grating vector  $\vec{K}_{vol}$  in an Ewald sphere. This is the case in the hologram recording process when the interference pattern of the reference and signal wave defines the grating vector. Part (b) shows the resulting hologram parameters: the grating vector lies in the hologram volume with volume grating period  $\Lambda_{vol}$  and slant angle  $\phi$  between the grating vector and the  $z$ -axis.

wave propagation in the hologram as

$$\nabla^2 E + (\beta^2 - 2i\alpha\beta + 2\kappa\beta(e^{i\vec{K}_{vol}\vec{r}} + e^{-i\vec{K}_{vol}\vec{r}}))E = 0. \quad (\text{II.26})$$

Solving Eq. II.26 requires to make an ansatz for the incident and diffracted waves. The incident wave can be assumed as a plane wave  $R(x, z) = Re^{-i\vec{k}_R\vec{r}}$  analogous to the one used in the recording process (even though its direction and wavelength  $\lambda$  may differ). In the general case, an infinite number of diffraction orders can be considered so that the total field in the hologram is given as

$$E(x, z) = Re^{-i\vec{k}_R\vec{r}} + \sum_m S_m e^{-i(\vec{k}_R - m\vec{K}_{vol})\vec{r}} \quad (\text{II.27})$$

with  $m$  denoting the different diffraction orders. In this notation,  $S_0$  is zero, because the zeroth order is separated from the sum as the  $Re^{-i\vec{k}_R\vec{r}}$  term. The methods to solve the coupled wave equations presented in the following differ in how many diffraction orders they consider for their ansatz.

### Kogelnik theory

Kogelnik theory, first presented in Ref. [92] and reiterated here, solves the coupled wave equations by making an ansatz that consists of only two waves: the incident reference wave  $R$  and a diffracted wave called the signal wave  $S$ . All other diffraction orders are neglected. This ansatz can be written as

$$E(x, z) = R(z)e^{-i\vec{k}_R \vec{r}} + S(z)e^{-i\vec{k}_S \vec{r}}. \quad (\text{II.28})$$

Inserting Eq. II.28 into Eq. II.26, considering that in the wavefront reconstruction process the wave vector of the diffracted wave is forced by the grating to be  $\vec{k}_S = \vec{k}_R - \vec{K}_{\text{vol}}$  and comparing the terms with equal exponentials yields Kogelnik's coupled wave equations:

$$\begin{aligned} R'' - 2iR'k_{R,z} - 2i\alpha\beta R + 2\kappa\beta S &= 0 \\ S'' - 2iS'k_{S,z} - 2i\alpha\beta S + (\beta^2 - \sigma^2)S + 2\kappa\beta R &= 0 \end{aligned} \quad (\text{II.29})$$

with  $R'$ ,  $S'$  and  $R''$ ,  $S''$  denoting the first and second derivatives in  $z$ -direction, respectively, and  $k_{R,z}$  and  $k_{S,z}$  denoting the  $z$ -components of the wave vectors. Assuming that the energy exchange between the two waves and absorption are slowly occurring as the waves travel through the hologram, Kogelnik neglects  $R''$  and  $S''$ . Using the  $z$ -components of the normalized wave vectors

$$\begin{aligned} c_R &= \frac{k_{R,z}}{\beta} = \cos \theta \\ c_S &= \frac{k_{S,z}}{\beta} = \cos \theta - \frac{K_{\text{vol}}}{\beta} \cos \phi, \end{aligned} \quad (\text{II.30})$$

which can be found by considering the angle of incidence of the reference  $\theta$  and the slant angle  $\phi$  between the grating vector and the  $z$ -axis shown in Fig. II.9 (b), the coupled wave equations can then be expressed as

$$\begin{aligned} c_R R' + \alpha R &= -i\kappa S \\ c_S S' + (\alpha + i\vartheta)S &= -i\kappa R. \end{aligned} \quad (\text{II.31})$$

The coupled wave equations then describe how the amplitude of the waves traveling along  $z$  change by absorption ( $\alpha R$ ,  $\alpha S$ ) and coupling to each other ( $\kappa R$ ,  $\kappa S$ ). The dephasing measure  $\vartheta$  used here describes how strongly the reference wave couples to the

## II Background

---

signal wave and is given as

$$\vartheta = \Delta\theta K_{\text{vol}} \sin(\phi - \theta_0) - \Delta\lambda \frac{K_{\text{vol}}^2}{4\pi n}, \quad (\text{II.32})$$

which is a Taylor series expansion of the Bragg condition after differentiation by incidence angle  $\theta$  and wavelength  $\lambda$ . If the Bragg condition is met, i.e.  $\vartheta$  is zero, there is no additional loss due to dephasing. A general solution to these approximated coupled wave equations can be written down as

$$\begin{aligned} R(z) &= r_1 e^{\gamma_1 z} + r_2 e^{\gamma_2 z} \\ S(z) &= s_1 e^{\gamma_1 z} + s_2 e^{\gamma_2 z}. \end{aligned} \quad (\text{II.33})$$

The coefficients can then be determined by introducing boundary conditions such as  $R(0) = 1$  and  $S(0) = 0$  for transmission holograms and  $R(0) = 1$  and  $S(d_{\text{holo}}) = 0$  for reflection holograms. The DE is defined as the fraction of incident light power that is diffracted into the signal wave along  $z$ -direction:

$$\eta = \frac{|c_S|}{c_R} S S^* \quad (\text{II.34})$$

with  $S$  denoting  $S(0)$  for reflection and  $S(d_{\text{holo}})$  for transmission holograms. For the case of the lossless transmission holograms relevant for this thesis, inserting the solution for  $S(d_{\text{holo}})$  into Eq. II.34 leads to

$$\eta = \frac{\sin^2(\sqrt{\nu^2 + \zeta^2})}{1 + \frac{\zeta^2}{\nu^2}} \quad (\text{II.35})$$

with the parameter  $\zeta$  describing the deviations in angle of incidence and wavelength from the Bragg condition

$$\begin{aligned} \zeta &= \Delta\theta \frac{K_{\text{vol}} d_{\text{holo}} \sin(\phi - \theta_0)}{2c_S} \\ &= -\Delta\lambda \frac{K_{\text{vol}}^2 d_{\text{holo}}}{8\pi n c_S} \end{aligned} \quad (\text{II.36})$$

and the parameter  $\nu$  collecting the other variables as

$$\nu = \frac{\pi n_1 d_{\text{holo}}}{\lambda \sqrt{c_R c_S}}. \quad (\text{II.37})$$

Similar expressions for lossy and reflection holograms are found in Ref. [92] but skipped here for the sake of brevity.

### Rigorous Coupled Wave Analysis

While Kogelnik theory predicts DE well as long as the assumptions of two-wave theory are valid, it often is necessary to obtain more accurate results via rigorous methods. The coupled wave equations can be solved by a rigorous method first applied to slanted gratings by Moharam and Gaylord [93]. The general approach is to find solutions to the wave equation introduced in Eq. II.17 within and outside of the hologram and to determine the amplitudes of the resulting waves by considering the boundary conditions at the interfaces. In the following, the method initially presented in Ref. [93] is reiterated to convey a basic understanding of RCWA and FMM approaches.

For the sake of simplicity, it can be assumed that the media in front of and behind the hologram are homogeneous and that absorption is neglected. The dielectric constant is then  $\epsilon_1$  in front of the hologram called region 1,  $\epsilon = \epsilon_2 + \Delta\epsilon \cos(\vec{K}_{\text{vol}} \vec{r})$  inside the hologram called region 2 and  $\epsilon_3$  behind the hologram called region 3. Since a rigorous approach considers all possible transmitted and reflected waves, the field in region 1 can be written as

$$E_1 = e^{-i(k_{x,0}x + k_{z,0}z)} + \sum_l R_l e^{-i(k_{x,l}x + k_{z,l,s}z)} \quad (\text{II.38})$$

assuming unity amplitude on the incident wave and the  $s$  index on the wave vector denoting if the reflected wave was reflected at the interface ( $s = 1$ ) or in the volume ( $s=3$ ). The  $x$ -component of the wave vector of the reflected waves depends on the grating vector as  $k_{x,l} = k_1 \sin \theta - iK_{\text{vol}} \sin \phi$  with  $k_1$  denoting the length of the wave vector in region 1 and  $k_{z,l,s}^2 = k_l^2 - k_{x,l}^2$ . The field in region 3 is given as a superposition of transmitted waves

$$E_3 = \sum_l T_l e^{-i(k_{x,l}x + k_{z,l,3}(z - d_{\text{holo}}))}. \quad (\text{II.39})$$

## II Background

---

The field in region 2 is

$$E_2 = \sum_l \hat{S}_l(z) e^{-i(k_{x,l}x + k_{z,l,2}z)} \quad (\text{II.40})$$

with the wave vector depending on the angle of refraction in region 2 as  $k_{z,l,2} = k_1 \cos \theta' - iK_{\text{vol}} \cos \phi$  with  $\theta'$  denoting the angle of refraction of the incident wave in region 2.

Similar to the Kogelnik theory, the coupled wave equations can be found by plugging a relation for the dielectric constant such as Eq. II.22 and the ansatz for the fields in region 2 in Eq. II.40 into the wave equation Eq. II.17. When considering that the grating vector  $K_{\text{vol}}$  connects any  $l$ th wave with the  $(l-1)$ th and  $(l+1)$ th wave as  $\vec{K}_{\text{vol}} = k_l - k_{l+1}$  or  $\vec{K}_{\text{vol}} = k_{l-1} - k_l$ , the resulting infinite set of coupled wave equations can be written as

$$\frac{\Delta \epsilon}{8\epsilon_2} \frac{\partial^2 S_l(u)}{\partial u^2} = (\cos \theta' - i\mu \cos \phi) \times \frac{\partial S_l(u)}{\partial u} - \rho(l-B)S_l(u) + S_{l+1}(u) + S_{l-1}(u) \quad (\text{II.41})$$

with  $S_l(u)$  corresponding to  $\hat{S}_l(z)$ ,  $u = i\pi\Delta\epsilon z/2\lambda\sqrt{\epsilon_2} = j\kappa z$ ,  $\mu = \lambda/\Lambda_{\text{vol}}\sqrt{\epsilon_2}$ ,  $\rho = 2\lambda^2/\Lambda_{\text{vol}}^2\Delta\epsilon = 2\mu^2\epsilon_2/\Delta\epsilon$  and  $B = 2\Lambda_{\text{vol}}\sqrt{\epsilon_2}\cos(\phi - \theta')/\lambda = 2\cos(\phi - \theta')/\mu$ . Moharam and Gaylord formulated these coupled wave equations in matrix form to allow efficient computation

$$\begin{bmatrix} S' \\ S'' \end{bmatrix} = \begin{bmatrix} b_{rs} \end{bmatrix} \begin{bmatrix} S \\ S' \end{bmatrix} \quad (\text{II.42})$$

with  $S'$  and  $S''$  denoting the first and second derivatives in  $u$ , respectively. The solution to this equation are the eigenvalues and eigenvectors of matrix  $b_{rs}$  and take the form

$$S_i(u) = \sum_m C_m w_{l,m} e^{q_m u} \quad (\text{II.43})$$

with  $q_m$  being the  $m$ th eigenvalue and  $w_{l,m}$  being the  $m$ th element of the row in the matrix of eigenvectors corresponding to the  $l$ th wave. The coefficients  $C_m$  are found along with  $R_l$  and  $T_l$  by applying the boundary conditions for tangential fields to the equations, what yields a system of linear equations. The DE of the reflected and transmitted waves are

then given as

$$\begin{aligned}\eta_{1,l} &= \Re\left(\frac{k_{z,1,l}}{k_{z,1,0}}\right)R_l R_l^* \\ \eta_{3,l} &= \Re\left(\frac{k_{z,3,l}}{k_{z,1,0}}\right)T_l T_l^*.\end{aligned}\tag{II.44}$$

In practice, volume holograms are highly efficient and only a small range of waves  $l$  needs to be considered to obtain accurate results. But nowadays the high availability of computational resources means that there is little downside to increasing the range of waves  $l$  for the sake of increased accuracy.

### 2.2.3. Fabrication of arbitrary holograms

The upcoming chapter features a design method for arbitrary HOEs in which the distribution of volume grating periods and slant angle of the grating vector are optimized over the lens surface. The fabrication of such arbitrary HOEs is explained in the following.

As previously discussed, image holograms are recorded as the interference between a plane reference wave and the object wave, which is the light scattered from the object that is supposed to be displayed by the hologram. Most HOEs are recorded as the interference of two waves that can be either plane or spherical, depending on the application. Arbitrary HOEs can be written as the interference pattern of a plane wave and a wave that was arbitrarily structured by a phase mask such as an SLM. In case the pixelation of the SLM would degrade the hologram quality, a holographic printer [120, 121, 122, 123, 124] can be used to demagnify the SLM and write an array of holographic pixels (hogels). Each hogel is then an arbitrary hologram that is not limited by the pixelation of the SLM. The array of hogels itself introduces pixelation only if there is a small spacing between the hogels, which depends on the positioning accuracy of the holographic printer. Holographic printers have very slow writing speeds as they write in series, which adds up the required exposure times and requires additional time to damp all vibrations of moving parts that would disturb the interference pattern. For mass production, this can be circumvented by writing a master hologram that is then replicated by scalable roll-to-roll processes [138]. Therefore, the arbitrary HOE designs presented in the following chapters can in fact be fabricated and are suitable for mass production.





# III. Holographic optical element design method for spectacle lenses

This thesis aims at finding novel applications for HOEs in the field of spectacle lens design. For this purpose, a tool chain is required that addresses the challenges of using HOEs in spectacle lenses such as DE and grating dispersion as well as the known challenges in spectacle lens design such as the gazing eye problem. Fig. III.1 shows a flowchart that illustrates the task of the tool chain. The inputs to the tool chain are a physical model of the optical system including the parameters and geometry of the eye, the properties of the refractive spectacle lens and the HOEs as well as the DE requirements and the desired optical function in terms of SPH and AST prescription as well as CE thresholds. The task of the tool chain is to use e.g. optimization methods to compute a new configuration of the optical system, in which the desired optical function is achieved while keeping the HOE parameters within the constraints that follow from the DE requirements.

This chapter discusses such a tool chain starting with methods to control the DE and dispersion. Sect. 3.1 describes the angular and wavelength bandwidth limitations of HOE DE and calculates a minimum requirements for HOE DE bandwidths in spectacle lens applications. Based on these requirements, optimal HOE parameters for spectacle lens applications are calculated based on the Fourier Modal Method. Fixing the HOE configurations to achieve the required bandwidths limits the possible range of deflection angles that can be achieved by a single HOE. Sect. 3.2 then explains how HOE tandems can be used to circumvent the deflection angle limitation and to compensate dispersion, which is required to limit CE. With these challenges solved, Sect. 3.3 discusses a simple approach to designing HOE-based spectacle lenses as an array of partially overlapping lens-type HOEs. This approach creates discontinuities in the optical function of the spectacle lens, which limits its application to multifocal spectacle lenses. Sect. 3.4 solves this discontinuity problem by introducing a novel design approach for arbitrary, but continuous HOE structures for spectacle lens applications. This approach allows tailoring the optical func-

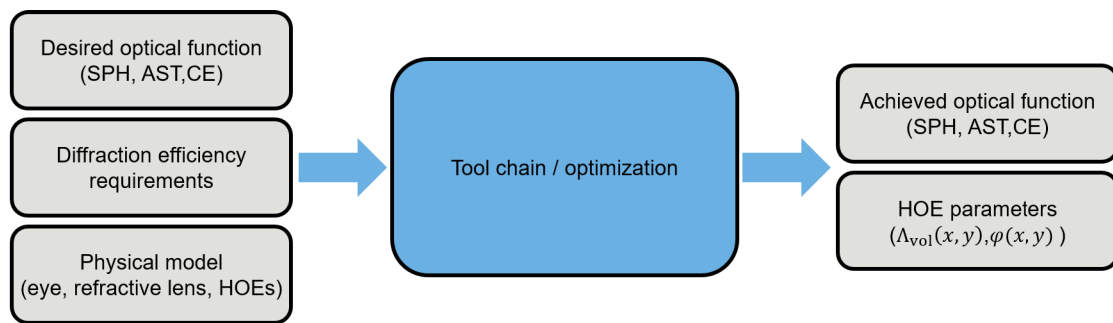


**Figure III.1.** Flowchart describing the task of a tool chain for designing HOE-based spectacle lenses. The inputs to the tool chain are a physical model of the optical system including the parameters and geometry of the eye, the properties of the refractive spectacle lens and the HOEs as well as the DE requirements and the desired optical function in terms of SPH and AST prescription as well as CE thresholds. The task of the tool chain is to use e.g. optimization methods to compute a new configuration of the optical system, in which the desired optical function is achieved while keeping the HOE parameters within the constraints that follow from the DE requirements.

tion of the HOEs to SVSLs as well as PALs.

### 3.1. Diffraction efficiency optimization

Depending on the application at hand, controlling the DE of a HOE can have different goals. In some applications such as monochromatic beam splitters, filters or master HOEs used in mass production type replication processes, it is desirable to fix DE at a specific value e.g. 50% for a 50/50 beam splitter. Positive and negative deviations from the desired value alike are detrimental to the HOE performance in this case. In some systems such as beam steering in telecommunications the goal might be to achieve high DE, but the overall system performance is dominated by other losses e.g. in optical fibers. Therefore, increasing DE might not always be a priority. In imaging systems however, achieving high DE means to reduce stray light, which can be a key contributor to low image quality. In some systems it might be possible to separate stray light like the 0th order light from the beam path relevant to the imaging process. In those cases, like some AR devices, a reduced DE is just a trade off with required display brightness. In the case of spectacle lenses, the goal is to preserve the brightness of the object that is being looked at and to keep stray light low for the best possible imaging performance. Both of these goals translate to keeping DE as high as possible.

#### 3.1.1. Bandwidth requirements

The requirement of achieving high DE can be expressed in terms of a required wavelength and angular bandwidth. For spectacle lenses, it is important to achieve the required wavelength and angular bandwidth simultaneously. In the following, a minimal DE of about 0.7 is assumed since this value has been found reasonable in literature [182]. It should be noted that a threshold value of 0.7 typically corresponds to a much higher mean DE.

##### **Wavelength bandwidth**

Spectacle lenses are expected to work over the visible spectrum of light (VIS), which is usually given as the range from 380 nm (violet) to 740 nm (red) [183]. In daylight, the spectral sensitivity of the eye is maximal at 555 nm (green) and rapidly decreasing to both sides [175]. Therefore, the aim is to achieve high DE over the VIS and placing the maximal DE in the green part of it.

##### **Angular bandwidth**

The angular bandwidth requirement for HOEs in spectacle lens applications depends on many geometrical factors that can vary between patients. Therefore, the required angular bandwidth is estimated for a sample geometry here, while keeping in mind that, if achievable, a larger angular bandwidth is preferable.

In principle, the required angular bandwidth for a HOE in any optical system can be calculated at the input or output side alike due to reciprocity in ray optics. In the case of SVSLs, it seems preferable to calculate the required angular bandwidth on the output side of the HOE since there it is easier to relate to the system geometry. The considerations to calculate the required angular bandwidth start by considering the principal rays introduced in Fig. II.4. There, it was established that for every gaze direction of the eye there is a corresponding principal ray, which connects the center of the eye pupil with the rotational center of the eye ball. Each principal ray intersects the lens at a different position. It is now assumed that at each lens position the available angular bandwidth is centered on the principal ray. This ensures that for each gaze direction, the DE is maximal for the rays in the pupil center. The required angular bandwidth at a lens position is then given as the maximal angular detuning between the corresponding principal ray and other rays entering the pupil at this gaze direction and can be calculated using geo-

### III Holographic optical element design method for spectacle lenses

metrical optics. This is illustrated in Fig. III.2 (a). For the sake of simplicity, a parallel bundle of rays filling the pupil of the eye with the principal ray being in the center of the bundle is considered, here shown as blue rays parallel to a principal ray drawn in red. Ignoring possible lens curvature the one-sided maximal angular detuning between another principal ray and one of the blue rays intersecting the lens at the same position can now be calculated as

$$\frac{\Delta\theta_{\text{air}}}{2} = \arctan\left(\frac{y_{\text{pos}} + \frac{d_{\text{pupil}}}{2}}{d_{\text{eye lens}}}\right) - \arctan\left(\frac{y_{\text{pos}}}{d_{\text{eye lens}}}\right) \quad (\text{III.1})$$

with  $y_{\text{pos}}$  being the current position on the lens,  $\frac{d_{\text{pupil}}}{2}$  being half the pupil diameter and  $d_{\text{eye lens}}$  being the distance between the rotational center of the eye and the lens. The  $d_{\text{eye lens}}$  is assumed as 33.5 mm here, with 13.5 mm accounting for the distance between the front vertex of the eye and its center point [175] and 20 mm accounting for the distance of the eye to the lens. The required angular bandwidth within the lens, where the HOEs are to be placed, can be calculated by applying Snell's law to Eq. III.1 yielding

$$\Delta\theta_n = 2 \arcsin\left(\frac{\sin\left(\arctan\left(\frac{y_{\text{pos}} + \frac{d_{\text{pupil}}}{2}}{d_{\text{eye lens}}}\right) - \arctan\left(\frac{y_{\text{pos}}}{d_{\text{eye lens}}}\right)\right)}{n_{\text{lens}}}\right) \quad (\text{III.2})$$

with  $n_{\text{lens}}$  being the refractive index of the lens polymer. To get a prediction of the worst case scenario, a polymer used in spectacle lenses with a relatively low refractive index of 1.59 is chosen for the further analysis. Fig. III.2 (b) shows an evaluation of Eq. III.2 for different pupil diameters  $d_{\text{pupil}}$  and lens positions  $y_{\text{pos}}$ . The required angular bandwidth in the lens material  $\Delta\theta_n$  decreases with lens position and increases roughly linearly with pupil diameter. Depending on the light condition, the human pupil diameter varies between 2 and 8 mm [175]. This means that for a HOE based SVSL to function in bright daylight, which would correspond to a pupil size of about 2 mm, an angular bandwidth of about  $2^\circ$  is required. While this calculation is just a rough estimation neglecting e.g. lens curvature, it can be concluded that HOEs with an angular bandwidth considerably above  $2^\circ$  will function as intended.

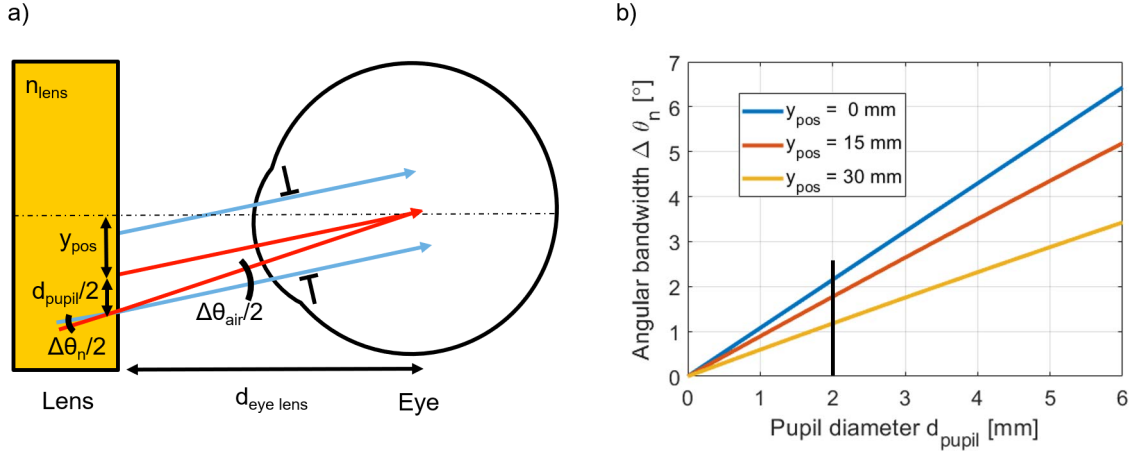


**Figure III.2.** (a) Sketch of the geometry of the lens and eye required to calculate the required angular bandwidth in air and in the lens material. The assumption here is that the available bandwidth at each lens position is centered on the local principal ray and therefore the required bandwidth is given as the detuning between a principal ray (red rays) and the outermost ray in a bundle (blue rays). (b) Evaluation of Eq. III.2 describing the required angular bandwidth in the lens material  $\Delta\theta_n$  as a function of pupil diameter  $d_{\text{pupil}}$  and lens position  $y_{\text{pos}}$ .

### 3.1.2. Optimization with the Fourier Modal Method

The DE requirements for HOE-based spectacle lenses in terms of wavelength and angular bandwidth have been introduced in the previous subsection. Both wavelength and angular bandwidth have to be achieved simultaneously by optimizing the relevant HOE parameters such as volume grating period, HOE thickness or strength of the refractive index modulation. This goal can be visualized as the DE plotted over wavelength and angle being a rectangle with side lengths of the VIS for wavelength and at least  $2^\circ$  for angle. From previous work conducted within the Zeiss group [182] it is known that the DE plotted over wavelength and angle of HOEs often is an ellipsoid, that should be as horizontal as possible i.e. parallel to the wavelength axis. The goal therefore translates to finding a HOE parameter regime with high overall DE that has an elliptic shape parallel to the wavelength axis and consequently ensures high DE for the required wavelength bandwidth.

Here, this matter is further investigated by using an in-house MATLAB implementation of the Fourier Modal Method (FMM), which is mathematically equivalent to the Rigorous Coupled Wave Analysis (RCWA) presented in Sect. 2.2, to simulate the DE of HOEs. In principle, the task at hand is an optimization problem for DE that depends on several HOE parameters: HOE volume grating period, HOE thickness, HOE refractive index, HOE

refractive index modulation. However, knowledge from previous work and the desire to limit HOE parameters to realistic values that can be achieved with state of the art materials such as Bayfol by Covestro AG [147, 149, 146] significantly reduces the complexity of this optimization problem. The investigated HOEs have a refractive index of 1.492, a refractive index modulation of 0.02 and a thickness of 25  $\mu\text{m}$ , which is well within the available Bayfol configurations. This leaves the volume grating period as the main parameter to be optimized. It is known from theory that the volume grating period of a HOE controls the Bragg condition and fixes the HOE deflection angle of maximal DE. This means that a lens type behavior with high DE requires at least a certain variance of the volume grating period over the lens surface. As a side note, the slant angle does not affect the DE bandwidths, but merely shifts it in angle. Therefore, it is necessary to identify a large range of volume grating periods, for which the requirements for wavelength and angular bandwidth can be met. For this purpose, the DE is simulated as a function of wavelength and angle for HOEs of the aforementioned parameters and the results are plotted for volume grating periods between 1.0  $\mu\text{m}$  and 3.0  $\mu\text{m}$  in Fig. III.3. It is found that as volume grating periods increase from 1.0  $\mu\text{m}$  to about 2.4  $\mu\text{m}$ , the elliptic shape of high DE becomes more parallel to the wavelength axis, which is preferable since it increases the wavelength bandwidth. Further increases of the volume grating period from 2.4  $\mu\text{m}$  to 3.0  $\mu\text{m}$  do not further improve the positioning of the ellipse of high DE with respect to the wavelength axis. Instead, the shape of the DE profile changes and is no longer elliptical. As can be seen for the 3.0  $\mu\text{m}$  volume grating period HOE in part (f), the angular bandwidth now decreases for the short wavelengths and increases for the long wavelengths. Furthermore, the magnitude of DE starts to decrease as well. The combination of the three effects of changes in ellipse orientation, loss of DE magnitude and loss of elliptical shape of the DE pattern going from lower to higher volume grating periods means that the optimal range of volume grating periods for achieving the required angle and wavelength bandwidth simultaneously is found between 2.0  $\mu\text{m}$  and 2.7  $\mu\text{m}$ . However, even for the preferred configuration of 2.4  $\mu\text{m}$  shown in part (d), the required angular bandwidth of about  $2^\circ$  is only achieved for a limited wavelength bandwidth of 450 nm to 610 nm.

#### 3.1.3. Multiplexing

Since it is not possible to achieve the required wavelength and angular bandwidth simultaneously by using optimal HOE parameters, angular multiplexing is investigated as a

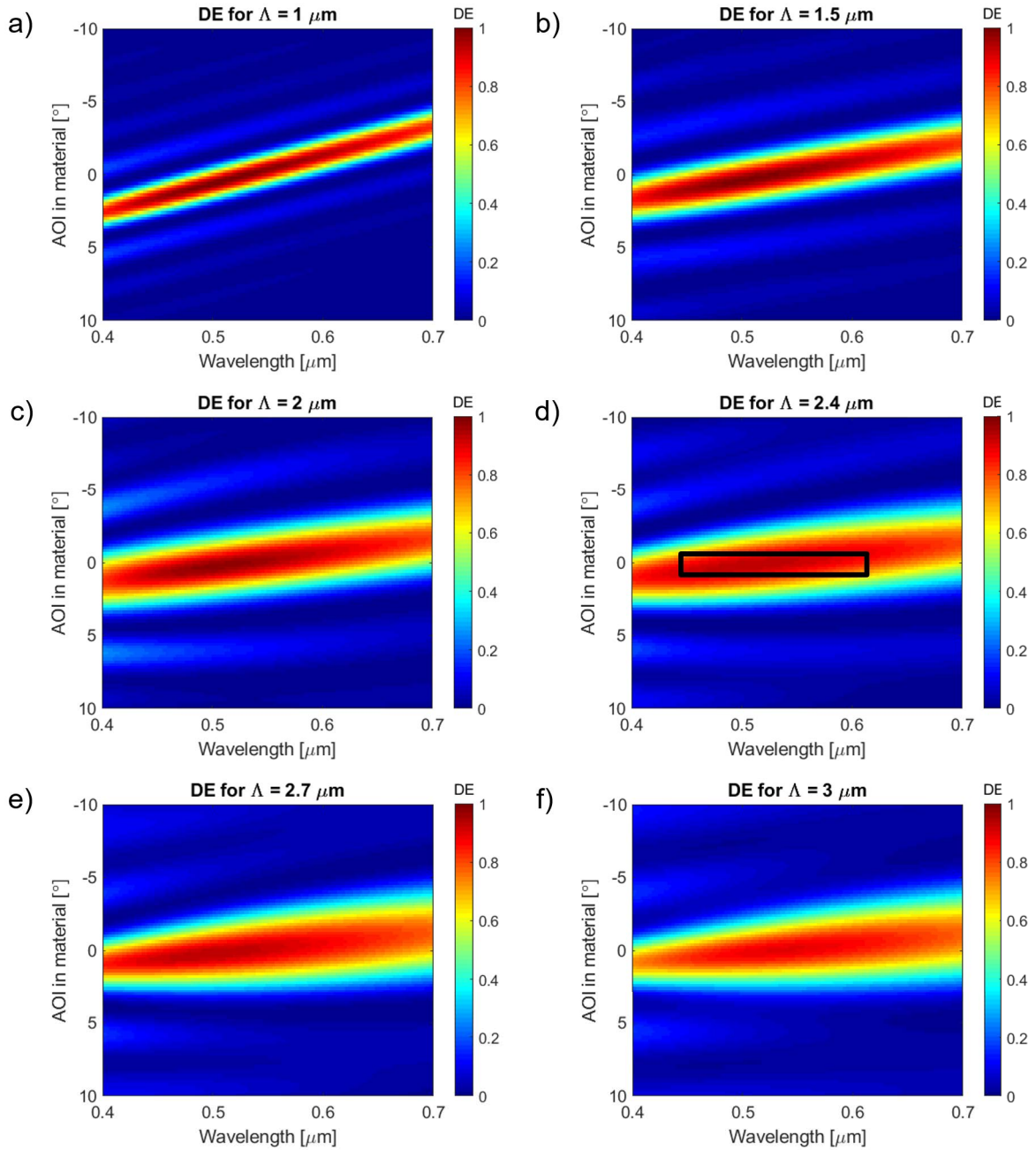


**Figure III.3.** FMM simulation of HOE diffraction efficiency (DE) as a function of wavelength and angle of incidence (AOI) for a volume grating period of  $1.0 \mu\text{m}$  (a),  $1.5 \mu\text{m}$  (b),  $2.0 \mu\text{m}$  (c),  $2.4 \mu\text{m}$  (d),  $2.7 \mu\text{m}$  (e) and  $3.0 \mu\text{m}$  (f). All HOEs have a grating thickness of  $25 \mu\text{m}$  and a refractive index modulation of 0.02. The black rectangle in part (d), which is the preferred configuration, indicates that the required angular bandwidth of about  $2^\circ$  is achieved only for a limited wavelength range.



### III Holographic optical element design method for spectacle lenses

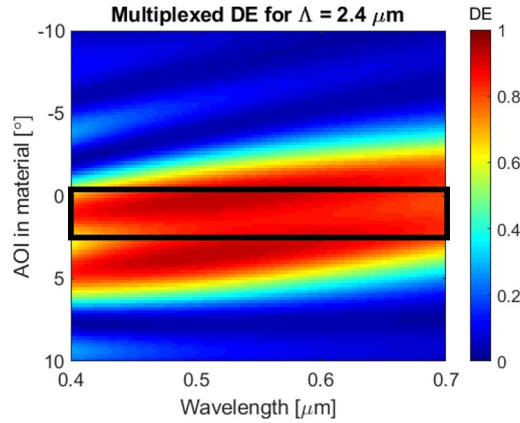


**Figure III.4.** FMM simulation of a multiplexed HOE diffraction efficiency (DE) as a function of wavelength and angle of incidence (AOI) for a volume grating period of  $2.4 \mu\text{m}$ . The multiplexed HOEs have a grating thickness of  $25 \mu\text{m}$  and a combined refractive index modulation of 0.02. The black rectangle indicates that the an angular bandwidth of about  $3.5^\circ$  is achieved for the VIS.

way to increase the angular bandwidth of a HOE.

Multiplexing is the technique of writing two or more holograms into the same holographic film. The multiplexed holograms then share the available index modulation of the holographic film, which can be visualized as a crossed grating. According to Ref. [184], the DE of a multiplexed hologram  $\eta_{\text{sys}}$  can be calculated as

$$\eta_{\text{sys}} = 1 - (1 - \eta_1)(1 - \eta_2)\dots(1 - \eta_n) \quad (\text{III.3})$$

with  $\eta_1$  to  $\eta_n$  being the DE of the  $n$ th hologram if they were written independently. Here, the angular bandwidth of the HOE configuration discussed in the last section is increased by multiplexing a second HOE of the same configuration and DE distribution that is shifted by  $3.5^\circ$  into the same film as the first HOE. The resulting DE distribution of the multiplexed structure is shown in Fig. III.4. The black rectangle indicates that an angular bandwidth of about  $3.5^\circ$  is achieved for the VIS. According to Fig. III.2 (b) this means that the provided angular bandwidth is sufficient for pupil sizes up to at least 3 mm. Similar results can be obtained for other volume grating periods between  $2.0 \mu\text{m}$  and  $2.7 \mu\text{m}$ . Therefore, HOEs in this volume grating period range in principle are suitable for spectacle lens applications.



## 3.2. Dispersion and deflection angle management

The considerations made for DE optimization in Sect. 3.1 fixed the HOE volume grating period, thickness, refractive index and refractive index modulation. While the latter are only relevant for DE, the volume grating period directly influences the HOE deflection angle with highest DE. From the Ewald sphere shown in Sect. 2.2, the deflection angle  $\alpha_{\text{deflection}}$  of a single HOE can be calculated as

$$\alpha_{\text{deflection,HOE}} = 2 \arctan\left(\frac{\lambda}{2\Lambda_{\text{vol}}}\right) \quad (\text{III.4})$$

with  $\lambda$  being the wavelength of the incident light and  $\Lambda_{\text{vol}}$  being the volume grating period in question. Eq. III.4 shows that fixing the accepted range of volume grating periods for DE considerations also fixes the allowed range of HOE deflection angles, which is not centered around zero unless  $\Lambda_{\text{vol}} = \infty$  is accepted. In the context of spectacle lens design, this is a problem, because in a refractive spectacle lens, a ray going through the optical center of the lens would not be deflected i.e. have a deflection angle  $\alpha_{\text{deflection}}$  of zero. For the volume grating period range of  $2.0 \mu\text{m}$  and  $2.7 \mu\text{m}$  chosen in Sect. 3.1 and incident light within the VIS, the HOE deflection angles vary between  $8.5^\circ$  and  $20^\circ$ . This means that a single HOE can not achieve the deflection angles necessary to replicate the behavior of a refractive spectacle lens at high DE. Another problem that can be anticipated based on Eq. III.4 is grating dispersion, because the HOE deflection angle depends on the wavelength of the incident light. Compensating for grating dispersion is a key challenge for the use of HOEs in spectacle lenses.

The problems of dispersion and HOE deflection angle can not be solved by further optimization of an individual HOE, because there are no free parameters to do so. Therefore, additional optical components need to be introduced to the optical system. In the following, HOE tandems are presented as a way to address dispersion compensation as well as HOE deflection angle limitations. Afterwards, the dispersion compensation between a refractive lens and a HOE tandem is discussed as an additional measure to achieve dispersion compensation.

### 3.2.1. HOE tandems

It is known and used in many applications [185, 186] that the angular dispersion of a HOE or grating can be compensated by a second HOE or grating that has the same volume

grating period, but operates in the opposite sign diffraction order as the first one. This is true for HOEs as well as surface gratings and can be seen directly from the formula for angular grating dispersion  $D$

$$D = \frac{m}{\Lambda_{\text{surf}} \cos \theta_{\text{diff}}} \quad (\text{III.5})$$

with  $m$  denoting the diffraction order,  $\Lambda_{\text{surf}}$  denoting the surface grating period and  $\theta_{\text{diff}}$  denoting the diffraction angle [187]. For HOEs, Eq. III.5 is valid provided that the projection of the volume grating period  $\Lambda_{\text{vol}}$  onto the hologram surface as  $\Lambda_{\text{surf}}$  is used. The relationship between HOEs as volume elements and surface gratings is discussed in greater detail in Sect. 3.4. For linear gratings or HOEs with a constant (surface) grating period over the grating surface, this approach is sometimes used with gratings that are placed far apart. For gratings or HOEs, for which the (surface) grating period varies over the lens surface e.g. to realize a lens type function, placing the two gratings or HOEs far apart causes mapping issues in the sense that the individual rays do not necessarily intersect positions with identical (surface) grating period. These mapping issues can be minimized by placing the HOEs directly on top of each other, which is assumed in the following.

This approach of dispersion compensation comes with the added benefit of being able to adjust the deflection angle of the HOE tandem to zero. This is shown in Fig. III.5, where an incident ray with wave vector  $k_1$  is diffracted to wave vector  $k_2$  by HOE B and then wave vector  $k_2$  is diffracted by HOE A to wave vector  $k_3$ , which is parallel to wave vector  $k_1$ . Provided that the distance between the two HOEs is minimal, the spatial offset between  $k_1$  and  $k_3$  due to the propagation of  $k_2$  is minimal and it can be claimed that the HOE tandem structure has a HOE tandem deflection angle of zero.

It should be noted that a lens-type HOE designed as such a HOE tandem would still exhibit dispersion. Assuming that the volume grating periods at all positions are chosen so that the principal rays are perfectly dispersion compensated, ray bundles traveling through the HOEs would not see spatially varying HOE tandem deflection angles and therefore no lens-type function. This can be called a lens with zero CE and zero SPH. Building up SPH can now be achieved by rearranging the volume grating periods, which starts to introduce CE. In that sense the HOE tandem is analogous to a refractive lens: A flat sheet of glass would introduce neither SPH or CE. For glasses with increasing curvature, SPH will increase, but so will CE. This trade-off between SPH and CE is investigated more closely in Sect. 3.4.

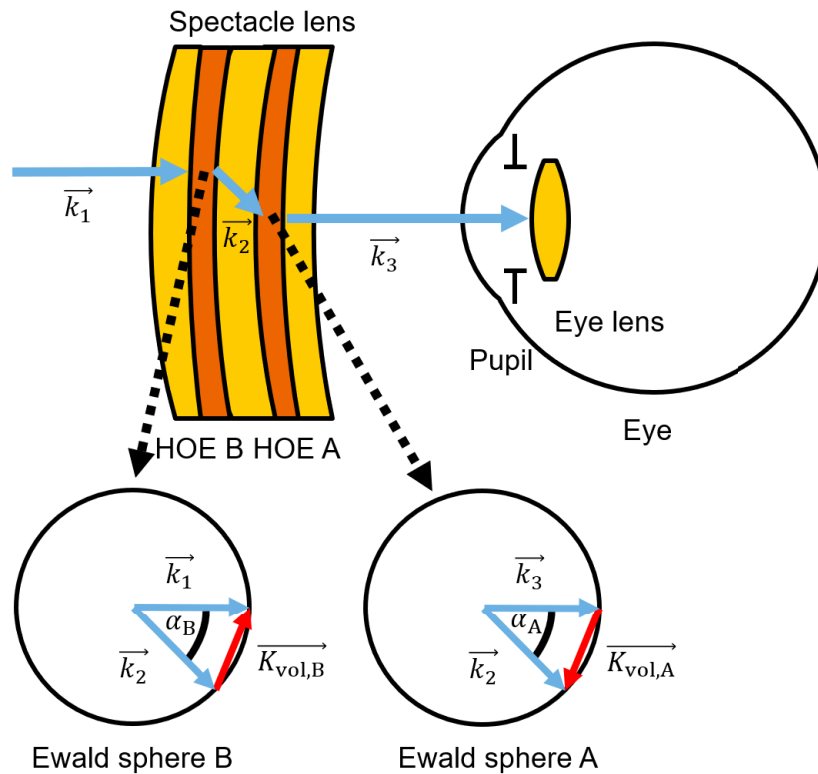


**Figure III.5.** Use of a HOE tandem in a spectacle lens for dispersion compensation and setting the overall deflection angle to zero. HOE A and HOE B operate in opposite diffraction orders so that their HOE deflection angles as well as dispersion cancels out. Possible refraction of the rays is not shown for sake of simplicity.

### 3.2.2. Holographic-refractive hybrid optics

As discussed in the previous paragraph, a HOE tandem fulfilling a lens-type function has a certain amount of CE. While in some cases this CE might be considered to be close enough to the human perception threshold to be acceptable, it is desirable to combine such a HOE tandem with a refractive lens to achieve holographic-refractive dispersion compensation as it is known for many diffractive-refractive hybrid systems in technical optics [117, 118, 119]. Holographic-refractive dispersion compensation is enabled by the fact that for same sign SPH, refractive and holographic components have opposite sign CE. This means that different from refractive achromats that require two lenses with opposite SPH and differing Abbe numbers leading to a very large optical system, holographic-refractive hybrid optics consist of holographic and refractive components with same sign SPH, whose CEs can compensate each other. Implementing such a holographic-refractive hybrid optics for spectacle lenses is a challenging task, because on top of the requirements

for the use of HOEs in spectacle lenses optical design problems specific to spectacle lenses such as the gazing eye problem need to be solved for the refractive as well as holographic components. Methods to do so are discussed in detail in Sect. 3.4.

## 3.3. Micro lens approach

While the DE and dispersion considerations in the previous sections are valid for HOEs in spectacle lens applications in general, designing the optical function of the HOE requires to tailor the HOE tandem deflection angle over the HOE surface to the requirements of the specific spectacle lens application and prescription. This can be done by considering the volume grating periods as a function of the HOE surface or, more straightforwardly, by using analytical HOE descriptions e.g. lens-type HOEs of a given focal length.

Previous work done within the Zeiss group proposed stacked and partially overlapping lens-type HOEs with different focal lengths to create spectacle lenses [182]. This approach is labeled "micro-lens approach" here, because it is very similar to an array of refractive micro lenses. While it is clear that the approach works for holographic bifocals, trifocals or other multi-focal lenses, it requires further investigation to show that this approach allows designing holographic PALs. In this thesis, the applicability of this approach was investigated using ray tracing and rigorous simulations.

### 3.3.1. Concept

Ref. [182] describes a "micro-lens approach" with spectacle lens designs consisting of stacked HOE tandems with some or no overlap. Each HOE tandem has a lens-type function and their focal power may vary between different HOE tandems. If there is no overlap between the HOE tandems, the resulting design is a HOE-based bifocal, trifocal or multi-focal spectacle lens since each HOE tandem forms its separate lens system, much like a facet eye lens. Fig. III.6 shows the recording (a) and use (b) of a HOE-based bifocal spectacle lens consisting of two HOE tandems that are placed next to each other with no overlap. By choosing different object distances indicated as distant objects in Fig. III.6 (a), the HOE tandems differ in SPH. Comparable to the behavior of refractive bifocal spectacle lenses, looking at a single HOE tandem yields SPH of this tandem. Following the same analogy, looking through the two HOE tandems at the same time creates two image points for one object point as shown in Fig. III.6 (b). The question that has been

unanswered so far is if overlapping a larger number of HOE tandems could be used to create other optical functions like PALs.

#### 3.3.2. Overlapping HOE tandems

To investigate the influence of overlapping HOE tandems, an optical system consisting of HOE tandems and an eye lens as shown in Fig. III.6 is implemented into an optical design software. This allows investigating the relationship between object points and their image on the retina by ray tracing. Overlapping the HOE tandems gives rise to many possible ray paths as the possible number of diffraction order permutations increases when a ray intersects up to 4 HOEs (2 for each of the 2 overlapping tandems). This effect was accounted for by simulating the ray paths for all relevant diffraction order permutations and to synthesize their PSFs in MATLAB. The resulting PSF for a single object viewed through two partially overlapping HOE tandems of equal SPH is shown in Fig. III.7. The PSF has two distinct peaks, one at  $x = 0 \mu\text{m}$ ,  $y = 0 \mu\text{m}$  and one at  $x = 0 \mu\text{m}$ ,  $y = 80 \mu\text{m}$ , which correspond to the imaging paths of the two HOE tandems without considering zeroth order contributions. In other words, overlapping HOE tandems does not extend the applicability of this approach to PALs by creating a smooth transition zone between two HOE tandems. It is therefore necessary to develop an approach for the design of continuous HOE structures that can realize arbitrary optical functions such as PALs.

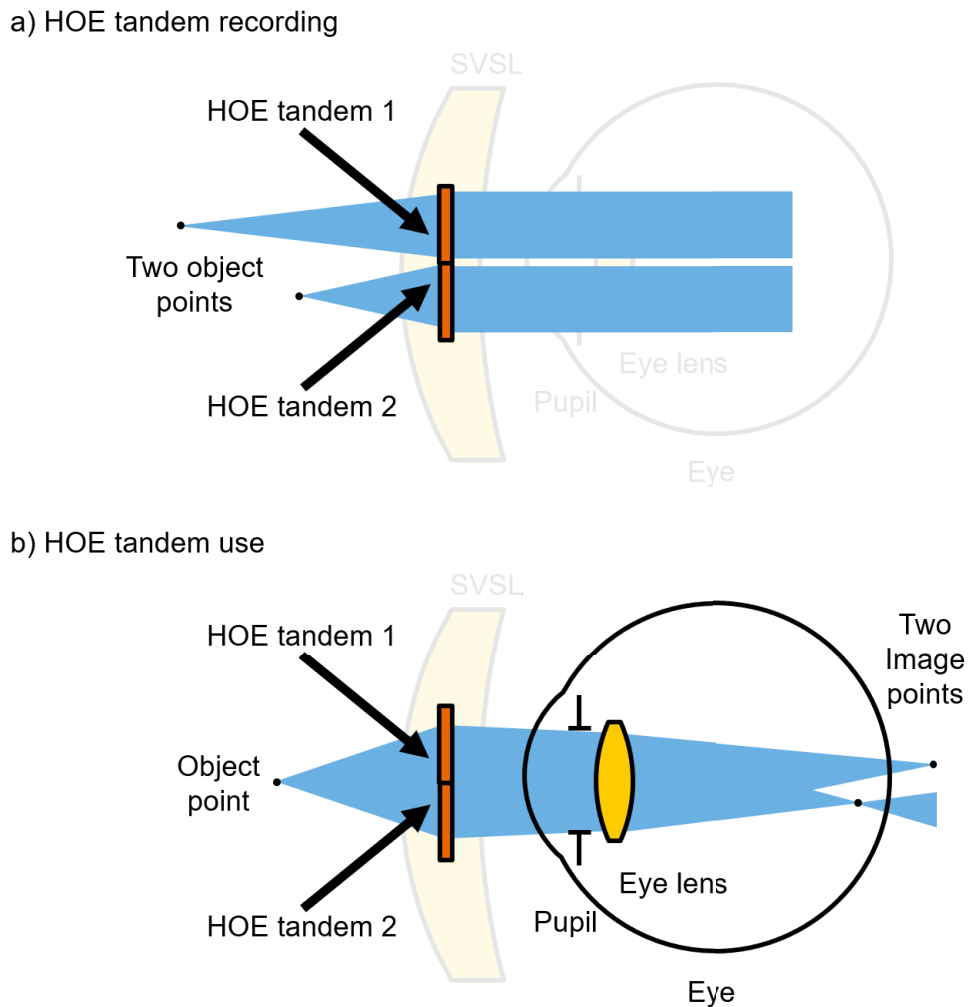


**Figure III.6.** Recording (a) and read-out scheme (b) for non-overlapping HOE tandems. The recording configurations of the HOE tandems are chosen so that each HOE tandem images a spherical wave coming from an object point into a plane wave. Since the spherical waves originating at different object points have different distances, the resulting SPH of the two HOE tandems differ as well. In combination with the eye lens, a HOE tandem can image the object point used to record it to a point on the retina. But when the eye looks at an object point through two HOE tandems at the same time, as depicted in part (b), the two HOE tandems diffract the incoming spherical wave into plane waves of different angles, which are then imaged to different points on the retina. The SPH difference of the HOE tandems leads to an offset of the two image points to the retina.

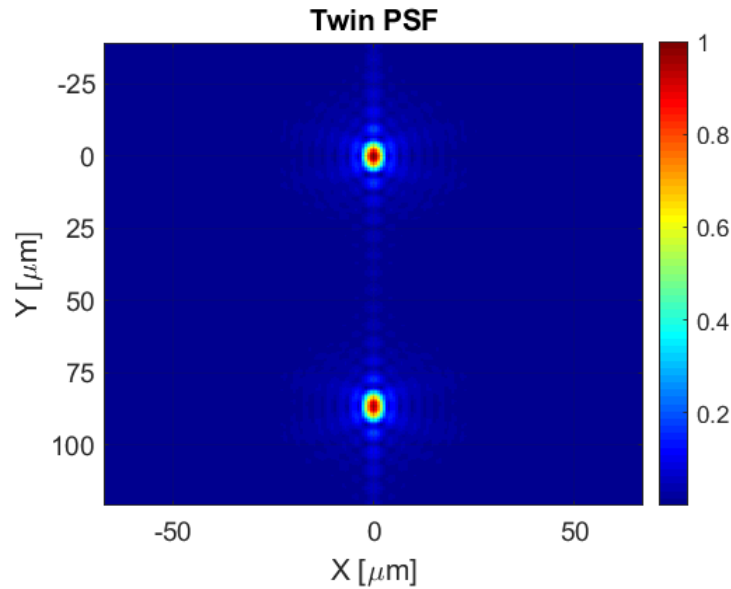


**Figure III.7.** Intensity plot of the PSF of a single object point when viewing it through two partially overlapping HOE tandems of equal SPH. For increased accuracy, this plot has been created by considering all relevant diffraction order permutations. The PSF has two distinct peaks, one at  $x = 0 \mu\text{m}$ ,  $y = 0 \mu\text{m}$  and one at  $x = 0 \mu\text{m}$ ,  $y = 80 \mu\text{m}$ . The two peaks correspond to the imaging paths of the two HOE tandems without considering zeroth order contributions. The zeroth order contributions to the PSF plot are almost invisible due to low intensity.

### 3.4. Continuous holographic optical element approach

The previous section shows that the optical function of HOEs in spectacle lens applications should be continuous to avoid blurred double images. This means that HOE parameters that are responsible for the HOE deflection angle and hence the optical function such as the volume grating periods can be described by continuous functions that vary across the HOE surface. The most simple example of this would be to use an analytical description of lens-type HOE tandems as the interference patterns of spherical and plane waves to create a single vision spectacle lens. But such a simple approach comes with several limitations: Firstly, it does not solve the gazing eye problem discussed in Sect. 2.1 and does not ensure that the required DE wavelength and angular bandwidth are achieved. Secondly, the approach is limited to single vision spectacle lenses with zero dpt astigmatism prescriptions. SVSLs with astigmatic prescriptions or more complex optical functions such as PALs cannot be designed in such a way. Thirdly, the dispersion compensation between two HOEs in a HOE tandem described in Sect. 3.2 requires that the local volume grating periods for each ray path are equal or similar. This is in general not the case in lens-type HOE tandems, where a first HOE images a spherical wave to a plane wave and

a second HOE images the plane wave to another plane wave of a different angle. Designing a lens-type HOE tandem with a similar volume grating period distribution on both HOEs is possible, but not within the confinements of this simple approach. Fourthly, this approach does not make use of the possibility of correcting aberrations via custom HOE functions.

All these limitations can be mitigated by a more complete design approach that includes all possible volume grating period functions over the HOE surface rather than just the ones described by the interference pattern of spherical and plane waves. The corresponding design tool chain is visualized as a flowchart in Fig. III.8. In this tool chain, HOEs are implemented into an optical design tool chain as surface gratings. This is one of the key features of the tool chain and discussed at length in the upcoming subsection. Another key feature is that the initial configuration of the HOEs is computed prior to the optimization in the optical design software. Along with the geometry of the eye and the refractive spectacle lens (if present, e.g. in a hybrid spectacle lens), the initial HOE configuration is considered the physical model of the optical system. Along with the desired optical function of the HOE-based spectacle lens in terms of SPH and AST prescription as well as CE, the physical model is the input for the optimization in the optical design software. There, the variable parameters of the optical system are iteratively varied and the merit function is evaluated via ray tracing until the minimal merit value corresponding to the optimal optical system is found. Within the limitations of the optimization routine, this optimal optical system has the best performance in terms of achieving the required optical function and the requirements for high DE, which were found via the Fourier Modal Method in Sect. 3.1. The tool chain then puts out the final systems performance and HOE configuration for further analysis. In the following, the workings of the tool chain are described in detail. It should be noted here that, as described in the last paragraph of Sect. 2.2, such arbitrary HOE designs can in fact be manufactured by holographic printers.

#### 3.4.1. HOE implementation

Ideally, HOEs could be implemented and optimized in optical design software as volume holograms with their volumetric properties and the resulting DE behavior. But this holistic treatment of volume holograms is not state of the art yet. The typical solution is to consider that the volumetric quantities of a volume hologram are only relevant for DE, but not for the ray deflection induced by the hologram. As already discussed in the context of



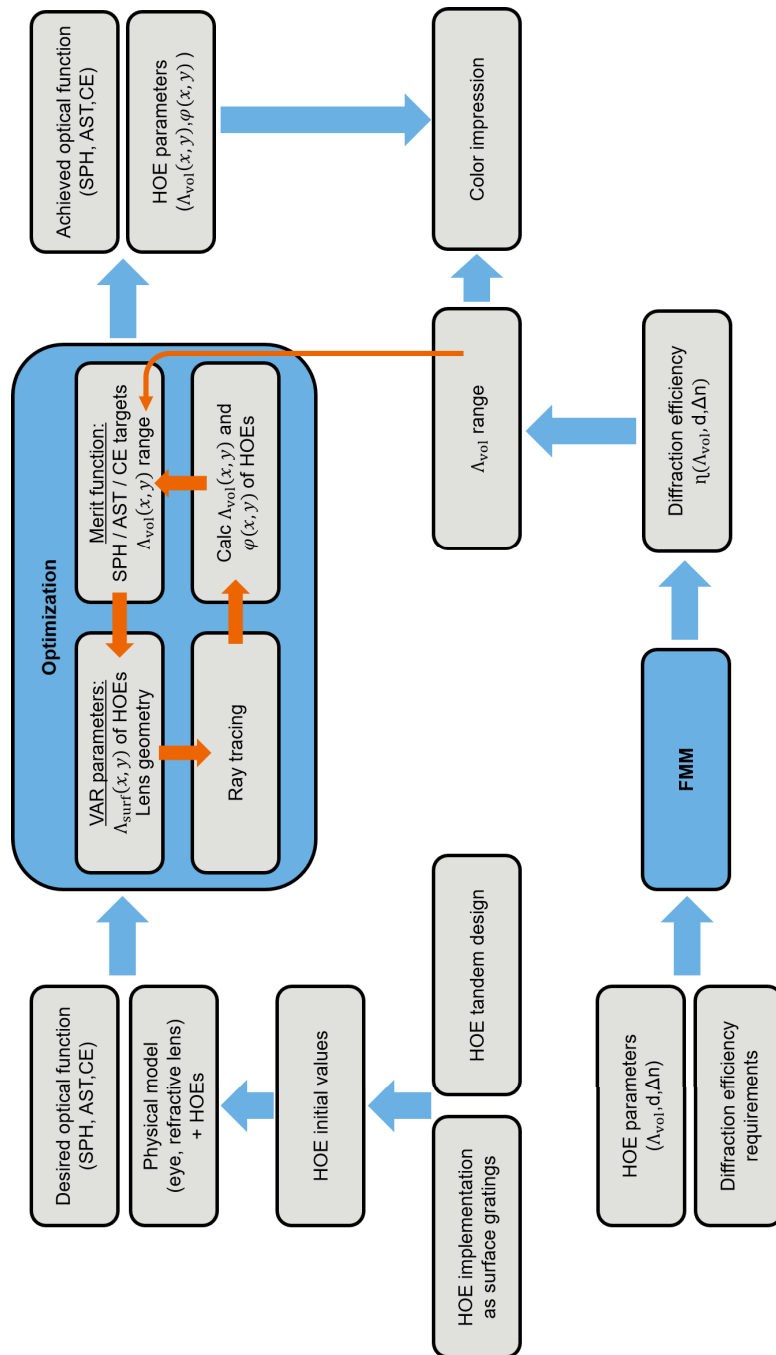


**Figure III.8.** Flowchart structuring the components of the optical design tool chain for HOE-based spectacle lenses. The lower branch describes how the optimization with the Fourier modal method discussed in Sect. 3.1 is used to determine the range of volume grating periods that fulfill the DE requirements. The upper branch describes how an implementation of HOEs as surface gratings and the tandem design play a key role in determining a physical model of the initial optical system. Together with the desired optical function of the HOE-based spectacle lens in terms of the SPH and AST prescription and CE, the physical model of the optical system is the input for an optimization that is implemented into an optical design software. Varying parameters of the optical system yields an optimal system in terms of achieving the desired optical function and fulfilling the DE requirements.

### III Holographic optical element design method for spectacle lenses

---

calculating DE, the wave vector of a diffracted wave is forced by the hologram as  $\vec{k}_S = \vec{k}_R - \vec{K}_{\text{vol}}$ . The underlying physical phenomena here is matching of the tangential components, which means that for ray direction purposes the  $z$ -components describing the volume of the hologram in propagation direction do not need to be considered. This is sometimes referred to as "transparency theory" because the hologram could be represented by a flat phase mask [80]. This means that the direction of a diffracted wave can be calculated using the grating equation known from surface gratings, found e.g. in Ref. [187]:

$$\frac{m\lambda}{\Lambda_{\text{surf}}} = \sin \theta_{\text{inc}} + \sin \theta_{\text{diff}} \quad (\text{III.6})$$

with  $\Lambda_{\text{surf}}$  denoting the projection of the volume grating period  $\Lambda_{\text{vol}}$  onto the grating surface. Fig. III.9 illustrates this concept using Ewald spheres. Part (a) shows the Bragg condition for a HOE with incident wave vector  $\vec{k}_1$ , diffracted wave vector  $\vec{k}_2$  and grating vector  $\vec{K}_{\text{vol,A}}$ . For the purpose of ray tracing i.e. determining the direction of the diffracted ray given the direction of an incident ray, only the  $x$ -component of  $\vec{K}_{\text{vol,A}}$  is relevant. For example, a binary surface grating shown in part (b) that has a grating vector  $\vec{K}_{\text{surf,B}}$  that is equal to the  $x$ -component of  $\vec{K}_{\text{vol,A}}$  would diffract an incident ray with wave vector  $\vec{k}_1$  into the same direction as the HOE in part (a). But the Bragg condition is violated in this case, which can be expressed by the dephasing measure  $\vartheta$ . As discussed in Sect. 2.2, a non-zero dephasing measure  $\vartheta$  decreases DE. This means that HOEs can be described as surface gratings provided that additional information is used to evaluate DE.

The proprietary optical design software used for this thesis allows defining HOEs by specifying the positions of two light sources, whose interference pattern describes the HOE surface grating period distribution over the HOE surface. This implementation does not take volumetric properties such as volume grating period or slant angle into account, but simply calculates the surface grating period distribution over the HOE surface and calculates the HOE deflection angle based on the grating equation Eq. III.6. The DE needs to be considered separately in this approach as well as in comparable state of the art solutions. Since the goal is to implement HOEs with arbitrary grating period distributions and not just the ones described by the interference of spherical and plane waves, the provided implementation is not suitable. However, the optical design software allows implementing surface gratings with arbitrary surface grating period distributions. In that case, the coefficients of a global polynomial  $p(x, y)$  are used to calculate the smooth

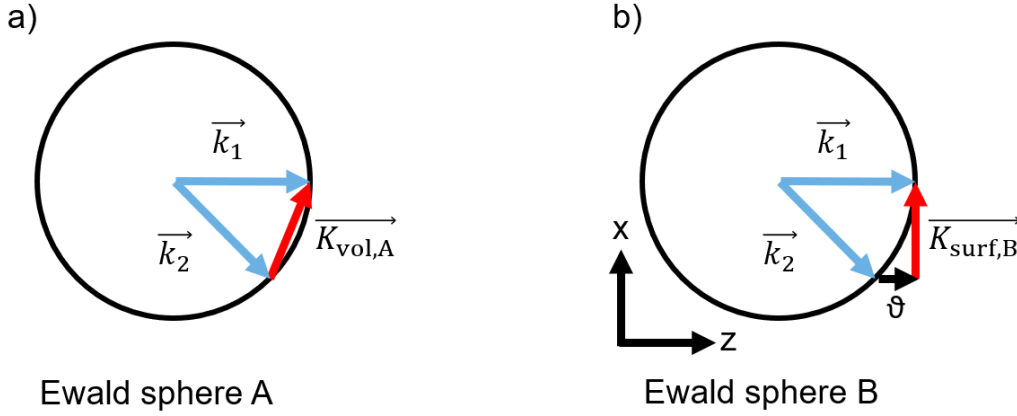


**Figure III.9.** Ewald spheres illustrating the consequences of implementing HOEs as surface gratings in an optical design software. Part (a) shows the Bragg condition for incident wave vector  $\vec{k}_1$ , diffracted wave vector  $\vec{k}_2$  and grating vector  $\vec{K}_{vol,A}$ . Part (b) shows that a surface grating whose grating vector  $\vec{K}_{surf,B}$  is equal to the x-component of  $\vec{K}_{vol,A}$  would diffract an incident ray with wave vector  $\vec{k}_1$  into the same direction as the HOE in part (a), but does not obey the Bragg condition as indicated by the dephasing measure  $\vartheta$ .

surface grating period distribution. The global polynomial is defined on a surface as

$$\begin{aligned}
 p(x, y) = & c_1x + c_2y \\
 & + c_3x^2 + c_4xy + c_5y^2 \\
 & + c_6x^3 + c_7x^2y + c_8xy^2 + c_9y^3 \\
 & + c_{10}x^4 + c_{11}x^3y + c_{12}x^2y^2 + c_{13}xy^3 + c_{14}y^4 \\
 & + c_{15}x^5 + c_{16}x^4y + c_{17}x^3y^2 + c_{18}x^2y^3 + c_{19}xy^4 + c_{20}y^5 \\
 & + \dots
 \end{aligned} \tag{III.7}$$

The local grating vector of the surface grating can be calculated as

$$\vec{K}_{surf} = \vec{\nabla}p(x, y). \tag{III.8}$$

The local surface grating period used to calculate the HOE deflection angles via the grating equation is then given as

$$\Lambda_{surf} = \frac{2\pi}{|\vec{K}_{surf}|} = \frac{2\pi}{|\vec{\nabla}p(x, y)|}. \tag{III.9}$$

The advantage of this surface grating implementation is that it defines arbitrary surface grating period distributions with small numbers of coefficients  $c_n$ . This is relevant because

### III Holographic optical element design method for spectacle lenses

---

it reduces the required amount of variable parameters for optimization procedures and consequently leads to better convergence behavior in the optimization process.

For this reason, HOEs were implemented as surface gratings in the optical design software. This means that only the surface grating period  $\Lambda_{\text{surf}}$  is defined within the given implementation and that volumetric properties such as volume grating period  $\Lambda_{\text{vol}}$  or slant angle  $\phi$  have to be handled separately. For the case of a HOE surface in  $x$  and  $y$  coordinates,  $z$  being the propagation direction and the HOE parameters being independent of  $y$ , the grating vector in the volume  $\vec{K}_{\text{vol}}$  can be expressed as:

$$\vec{K}_{\text{vol}} = \frac{2\pi}{\Lambda_{\text{vol}}} \begin{pmatrix} \sin \phi \\ 0 \\ \cos \phi \end{pmatrix}. \quad (\text{III.10})$$

Projecting this vector onto the HOE surface yields the surface grating vector  $\vec{K}_{\text{surf}}$ :

$$\vec{K}_{\text{surf}} = \frac{2\pi}{\Lambda_{\text{vol}}} \begin{pmatrix} \sin \phi \\ 0 \\ 0 \end{pmatrix}. \quad (\text{III.11})$$

Calculating the length of  $\vec{K}_{\text{surf}}$  then leads to a relationship between surface grating period  $\Lambda_{\text{surf}}$ , volume grating period  $\Lambda_{\text{vol}}$  and slant angle  $\phi$ :

$$|\vec{K}_{\text{surf}}| = \frac{2\pi}{\Lambda_{\text{vol}}} \sin \phi \stackrel{!}{=} \frac{2\pi}{\Lambda_{\text{surf}}} \implies \Lambda_{\text{surf}} = \frac{\Lambda_{\text{vol}}}{\sin \phi}. \quad (\text{III.12})$$

Implementing a HOE as a surface grating in an optical design software means that only the surface grating period  $\Lambda_{\text{surf}}$  is explicitly given. According to Eq. III.12, this surface grating period  $\Lambda_{\text{surf}}$  corresponds to HOEs with a fixed ratio of volume grating period  $\Lambda_{\text{vol}}$  and slant angle  $\phi$ , but one of these quantities can be chosen freely when determining the volume parameters.

In Sect. 3.1, the assumption was made that the available angular bandwidth of HOE DE should always be centered on the principal rays. Fig. III.10 illustrates how this requirement can be met by choosing the local slant angle at each position on the HOE surface so that the principal ray corresponding to that position satisfies the Bragg condition. Part (a) shows the Bragg condition for a HOE with volume grating vector  $\vec{K}_{\text{vol},A}$ , slant angle  $\phi_A$  and the corresponding incident wave vector  $\vec{k}_{1,A}$  and diffracted wave vector  $\vec{k}_{2,A}$ . In

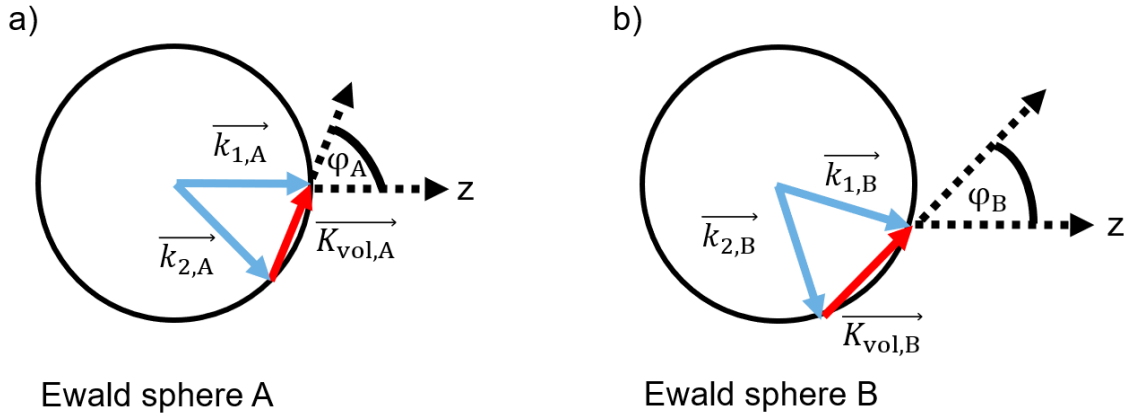


**Figure III.10.** Comparison between two HOE configurations (a) and (b) with the same surface grating period, but different slant angles  $\phi_A$  and  $\phi_B$ . The Ewald spheres illustrate, that changes in the slant angle lead to different Bragg conditions for a fixed wavelength of the incident wave vector. In other words, changes in the slant angle shift the DE bandwidth in angle.

part (b) the slant angle  $\phi_B$  was decreased relative to slant angle  $\phi_A$  and following Eq. III.12, the volume grating period  $\Lambda_{vol,B}$  was decreased to keep the surface grating period constant. Following  $|K| = 2\pi/\Lambda$ , the reduced volume grating period leads to a longer grating vector  $\vec{K}_{vol,B}$  in the figure. Constructing the Bragg condition in the Ewald sphere for the same incident wavelength i.e. the same length for the incident and diffracted wave vectors as in part (b) yields that the maximal DE is now achieved for incident wave vector  $\vec{k}_{1,B}$ , which has a different direction than  $\vec{k}_{1,A}$ . This means that at each lens position, the slant angle can be chosen in a way that the local principal ray obeys the Bragg condition for maximal DE.

The flowchart shown in Fig. III.8 describing the individual components of the tool chain indicates that HOEs are implemented as surface gratings as discussed so far. It also shows that during each iteration of the optimization routine it is necessary to calculate the volumetric properties of the HOEs such as the volume grating periods  $\Lambda_{surf}$  and slant angle  $\phi$ . This is implemented in the tool chain in the following way: At each moment when the volumetric properties are required, the principal rays are traced through the optical system. The deflection angles of the HOEs are calculated using the local surface grating periods  $\Lambda_{surf,B}$ , which are defined by the coefficients of global polynomials  $p(x, y)$ . After this ray tracing step, the intersection points of the principal rays with the HOEs as well as their direction before and after the HOEs are known. Fig. III.11 shows how this information can be used to calculate the slant angle that ensures maximal DE for the principal rays. A bisecting line of the angle between the incident wave vector  $\vec{k}_1$  and the

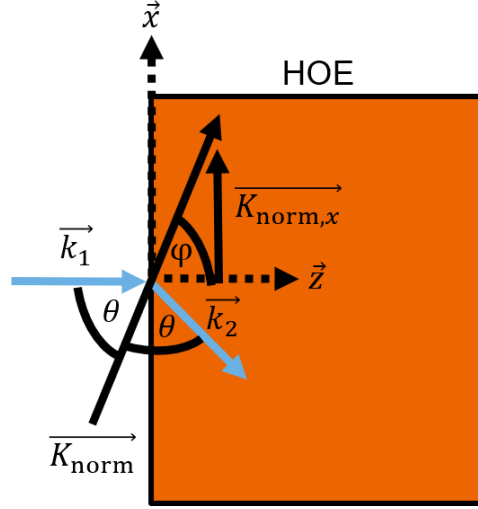


**Figure III.11.** Scheme for the calculation of the slant angle of a HOE based on its implementation as a surface grating. The surface grating period is used to calculate the deflection of an incident wave vector corresponding to a principal ray  $\vec{k}_1$  into the diffracted wave  $\vec{k}_2$ . The bisecting line between the angle of  $\vec{k}_1$  and  $\vec{k}_2$  then has the same direction as the volume grating vector, which satisfies the Bragg condition for the principal ray. In 2D considering only the x- and z-axis, the bisecting line can be represented by a vector of length one  $\vec{K}_{\text{norm}}$ . The sine of the slant angle  $\phi$ , i.e. the angle between the grating vector and the z-axis, is then given by the ratio the x-component of  $\vec{K}_{\text{norm}}$  and the normalized length of  $\vec{K}_{\text{norm}}$ .

diffracted wave vector  $\vec{k}_2$  can be constructed. In the general case, this line is represented by a 3D vector, but for the sake of simplicity it is represented as a 2D vector with x and z component here. This bisecting line has the same direction as the grating vector, whose direction suffices the Bragg condition for the principal ray, and is therefore labeled  $\vec{K}_{\text{norm}}$ . To simplify the following calculations, the length of  $\vec{K}_{\text{norm}}$  is normalized to one. The slant angle  $\phi$  as the angle between  $\vec{K}_{\text{norm}}$  and the z-axis is then given as

$$\sin \phi = \frac{\sqrt{|\vec{K}_{\text{norm},x}|^2 + |\vec{K}_{\text{norm},y}|^2}}{|\vec{K}_{\text{norm}}|} = \sqrt{|\vec{K}_{\text{norm},x}|^2 + |\vec{K}_{\text{norm},y}|^2}. \quad (\text{III.13})$$

This expression is then used to calculate the volume grating period  $\Lambda_{\text{vol}}$  as

$$\Lambda_{\text{vol}} = \Lambda_{\text{surf}} \sin \phi = \Lambda_{\text{surf}} \sqrt{|\vec{K}_{\text{norm},x}|^2 + |\vec{K}_{\text{norm},y}|^2}. \quad (\text{III.14})$$

Using these calculation steps, the slant angle  $\phi$  and the volume grating period  $\Lambda_{\text{vol}}$  can be calculated at a given moment of the optimization even though the surface grating implementation is used to represent the HOE.

### 3.4.2. Initial value calculation

Implementing HOEs as surface gratings, whose surface grating period is parameterized by a global polynomial  $p(x, y)$ , requires to specify the initial values for all coefficients  $c_n$ . The trivial approach would be to initialize all coefficients  $c_n$  as zero and hope that the optimization in the optical design process converges to a usable result by varying the coefficients. This works for convex optimization problems, but optical design, in general, is not a convex problem. Therefore, it is necessary to compute initial values that lead to the optimization algorithm converging to a usable result. In optics design, this usually means that the initial values need to be sufficiently close to a usable solution to begin with. Contrary to this, initializing all coefficients  $c_n$  as zero makes the global polynomial  $p(x, y)$  a flat surface and in turn, the surface grating period described by the inverse of the gradient of  $p(x, y)$  as stated in Eq. III.9 becomes infinitely large. The resulting HOE then has a deflection angle of zero and consequently no effect on the ray tracing. The merit function, which will be discussed later in detail, then returns an infinite value as the requirements for the optical performance of the system, e.g. to keep the volume grating period within the regime of high DE, are not met at all. If an optimization algorithm, such as a standard least-squares solver found in optical design software, then starts to slightly vary the coefficients  $c_n$ , the HOE's optical function changes randomly with each iteration, but it is unlikely that random variations on the coefficients  $c_n$  would lead to a configuration, in which the merit function returns a lower number and the algorithm converges.

Ideally, one set of initial values can be used to initialize HOE tandems for all types of spectacle lens applications and prescriptions. This can be achieved using a HOE tandem that satisfies the general requirements for HOEs in spectacle lenses i.e. the volume grating period constraints for high DE and the dispersion compensation between the two HOEs in the tandem. This corresponds to the ray path shown in Fig. III.5 where the dispersion and deflection induced by HOE B with grating vector  $\vec{K}_B$  is compensated by the dispersion and deflection induced by HOE A with grating vector  $\vec{K}_A$ . The general strategy to compute such initial values is to compute a vector field corresponding to the principal rays, then to calculate the local slant angles by considering the Bragg condition in an Ewald sphere and then to translate the local slant angles into a surface grating period distribution and finally to translate that surface grating distribution into a global polynomial  $p(x, y)$ . The last step is difficult, because the surface grating periods are connected to the global polynomial by a gradient operator, which cannot be reversed in the general case. Because of

this problem with the gradient operator, two successful implementations of this general strategy are discussed here. The first implementation solves a 2D problem on the center line of the lens rather than the full 3D problem with the advantage that in the 2D problem the inverse of the gradient operator is integration. The second implementation solves the 3D problem over the whole surface using a preexisting approximate integration code. It turns out that both implementations lead to the same results when optimizing a HOE-based spectacle lens, so after this section it will not be explicitly mentioned which set of initial values was used.

#### 2D solution

In the 2D case considering only the center line of the lens rather than the entire lens surface, several simplifications over the general strategy outlined above can be used. The principal rays, for example, can be described by their incidence angle rather than by vectors. In that case, the incidence angles as a function of the  $y$ -position of the lens are given as

$$\theta_{\text{inc}}(y) = \arctan\left(\frac{y}{d_1}\right) \quad (\text{III.15})$$

with  $d_1$  being the distance between the rotational center of the eye and the HOE. The angle between the incident and diffracted ray  $\alpha_{\text{deflection,HOE}}$  of a given wavelength  $\lambda$  and the desired volume grating period  $\Lambda_{\text{vol}}$  for the Bragg condition can be calculated from the Ewald sphere as stated in Eq. III.4. Since there is currently no constrain on  $\Lambda_{\text{vol}}$  aside from achieving high DE, the best case value of  $2.4 \mu\text{m}$  that was found in Sect. 3.1 on DE optimization is used here. Both expressions can be combined to calculate the local slant angle  $\phi$  for all  $y$ -positions on the center line ( $x = 0 \text{ mm}$ ) of the lens as

$$\phi(y) = \frac{\pi}{2} + \theta_{\text{inc}}(y) - \frac{\alpha_{\text{deflection,HOE}}}{2}. \quad (\text{III.16})$$

The surface grating period as a function of  $y$ -position can be computed with Eq. III.12. A polynomial function of degree 5 is then fitted to the inverse of the surface grating periods as a function of  $y$ -position. The resulting polynomial is then integrated, which yields all coefficients  $c_n$  of pure  $y$ -terms of  $p(x, y)$  until degree 6. These coefficients can be used to initialize the surface grating implementation of a HOE with arbitrary grating period distribution in the optical design software. For HOE tandem structures, the coefficients



can be used to initialize both HOEs since, provided that the distance between them is small, they require the same HOE deflection angles.

#### 3D solution

In the 3D case, the general strategy to compute initial values outlined above needs to be followed without simplifications. For this implementation, preexisting pieces of a ray tracing code as well as a preexisting implementation of an iterative integration method have been used. As a first step, a 3D vector field of principal rays is computed as a set of vectors at the origin of the coordinate system, which corresponds to the rotational center of the eye here. The components of the vectors are calculated by normalizing a vector  $\vec{c}_{\text{ray}}$  with

$$\vec{c}_{\text{ray}} = \begin{pmatrix} x_{\text{pos}} \\ y_{\text{pos}} \\ d_1 \end{pmatrix} \quad (\text{III.17})$$

with  $x_{\text{pos}}$  and  $y_{\text{pos}}$  being a discrete sampling of all valid HOE positions and  $d_1$  being the distance between the rotational center of the eye and the HOE. The principal ray going through the center of the lens consequently is represented by the unit vector in  $z$ -direction  $\vec{z}$  and intersects the HOE at

$$\vec{p}_{\text{intersection,central}} = \begin{pmatrix} 0 \\ 0 \\ d_1 \end{pmatrix}. \quad (\text{III.18})$$

The intersection point of the other principal rays with the HOE surface is calculated by a ray tracing calculation as

$$\vec{p}_{\text{intersection}} = \vec{p}_{\text{start}} + \frac{-\text{dot}(\vec{n}_{\text{surf}}, \vec{d}_1)}{\text{dot}(\vec{n}_{\text{surf}}, \vec{c}_{\text{ray,norm}})} \vec{c}_{\text{ray,norm}} \quad (\text{III.19})$$

with  $\vec{p}_{\text{start}}$  being the starting point of the principal ray, so in this step the origin of the coordinate system, "dot" denoting the dot product,  $\vec{n}_{\text{surf}}$  being the surface normal of the HOE,  $\vec{d}_1$  being the distance between the starting point of the ray and HOE surface in propagation direction  $z$  and  $\vec{c}_{\text{ray,norm}}$  being the normalized ray direction. Since at the first step all rays start from the origin,  $\vec{d}_1 = \vec{p}_{\text{intersection,central}}$  and, provided that the HOEs have

### III Holographic optical element design method for spectacle lenses

---

zero curvature, Eq. III.19 simplifies to

$$\vec{P}_{\text{intersection}} = \tilde{d} \vec{c}_{\text{ray,norm}} \quad (\text{III.20})$$

with  $\tilde{d}$  being a scaling factor that ensures that the  $z$ -component of  $\vec{P}_{\text{intersection}}$  is  $d_1$ . The direction of the grating vector corresponding to the central principal ray is found by rotating the unit vector in  $y$ -direction  $\vec{y}$  by  $\frac{\alpha_{\text{deflection,HOE}}}{2}$ , which is equivalent to the geometry expressed in Eq. III.16. The direction of the diffracted ray at the center of the lens is found by rotating the principal ray by  $\alpha_{\text{deflection,HOE}}$  around the  $y$ -axis. The local directions of the grating vector at all positions on the lens surfaces are then calculated by rotating the direction of the grating vector for the center principal ray by the rotation angle between the center principal ray and the principal ray intersecting the lens position in question. The same rotation is then applied to the diffracted ray to obtain the diffracted ray directions at all lens positions. At this point, the vectors are scaled to their actual length, i.e. the grating vectors to  $\frac{2\pi}{\Lambda_{\text{vol}}}$  and the incident ray and diffracted ray to  $\frac{2\pi}{\lambda}$ .

The resulting relationships between the local principal rays (red), diffracted rays (green) and grating vectors (blue) in  $k$ -space are illustrated in Fig. III.12. For each lens position, the three vectors form a triangle i.e. they satisfy the Bragg condition for maximal DE as intended. In that sense, the figure can be understood as plotting the vectors in an Ewald sphere. The surface grating periods on the first HOE are calculated using Eq. III.12 with the slant angle being the dot product of the local grating vector and the unit vector in  $z$ -direction  $\vec{z}$  since the slant angle is defined as the angle between the grating vector and the propagation direction  $\vec{z}$ . The  $x$ - and  $y$ -components of the inverse of the surface grating periods are then the input arguments to an iterative integration method mentioned above. The method is based on conjugate gradient solving [188]. The integration method returns a 2D scalar field, whose gradient approximately matches the input parameters. This 2D scalar field is then fitted to a 2D polynomial over the intersection points of the principal rays with the first HOE. The coefficients of this fit then correspond to the coefficients of the global polynomial  $p(x, y)$  describing the first HOE.

To calculate the coefficients of  $p(x, y)$  of the second HOE, it is necessary to fit the 2D scalar function over the intersection points between the principal rays and the second HOE. For this purpose, the intersection points are calculated using Eq. III.18 with  $\vec{P}_{\text{start}}$  now being the intersection point of the principal ray and the first HOE,  $\vec{n}_{\text{surf}}$  being the surface normal of the second HOE,  $\vec{d}_1$  being replaced by  $\vec{d}_2$ , which represents the distance between the two HOEs and  $\vec{c}_{\text{ray,norm}}$  being the normalized direction of the diffracted ray

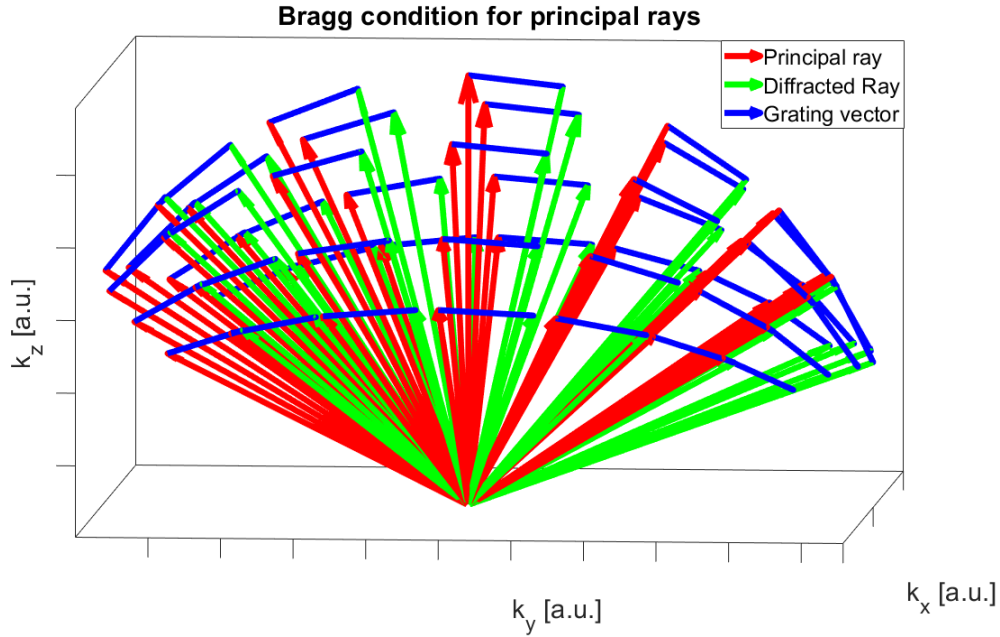


**Figure III.12.** 3D plot of the principal rays (red), diffracted rays (green) and grating vectors (blue) in  $k$ -space. For each lens position, the three vectors form a triangle i.e. they satisfy the Bragg condition as intended. In that sense, the figure can be understood as plotting the vectors in an Ewald sphere.

after the first HOE. Using the direction of the diffracted rays implicitly fixes the second HOE to operate in the opposite diffraction order as the first one, because the Bragg condition now is valid for the diffracted ray being diffracted into the original direction of the principal ray. Fitting the 2D scalar function over these intersection points now ensures that irrespective of the distance between the two HOEs, a principal ray traveling through the system will always be diffracted by the same magnitude of surface grating period on both HOEs in opposite diffraction orders and consequently be dispersion compensated.

### 3.4.3. Alternative HOE parameterizations

In principle, the parametrization of the HOEs can be done in other ways than the global polynomial  $p(x, y)$  from Eq. III.7. In fact, especially for PALs, a parametrization such as cubic splines could seem advantageous because it would allow to induce local variations rather than to affect the whole HOE with each parameter. However, even for relatively large patch sizes for the cubic splines, the number of coefficients quickly increases beyond what can be handled with the solvers and computational resources available for the work conducted for this thesis. Therefore, no viable alternatives to the global polynomial have

been found within this thesis.

#### 3.4.4. Optical design strategy

The considerations made so far allow implementing high DE, dispersion compensated HOE tandems with appropriate initial values for the parametrization of their surface grating periods into an optical design software. These HOE tandems can be used to design different types of spectacle lenses such as SVSLs or PALs for a wide range of prescriptions. The HOE tandems can be used as purely holographic optical systems or embedded into refractive lenses to create holographic-refractive hybrid optical systems. Consequently, different adaptations of a general optical design strategy are used for different applications.

In the following, the optical design strategy is described including the possible adaptations. Firstly, the possible configurations of the optical system acting as either a holographic or hybrid spectacle lens are described. This includes the possible variable parameters for the optimization process that differ from holographic to hybrid lenses. Secondly, the structure of the merit function describing the desired optical function and additional design requirements of the spectacle lens is discussed. This includes how the merit function differs between holographic and hybrid lenses as well as between SVSLs and PALs. Thirdly, the optimization process of the optical design software that is shown in Fig. III.8 is described in detail.

#### Optical system

Fig. III.13 shows an example optical system that illustrates all components that can be considered relevant to the optical design process. In all cases, a HOE tandem consisting of HOE A and HOE B is embedded into a refractive lens with front and back curvatures  $R_1$  and  $R_2$ , respectively, and center thickness  $D$ . In principle, HOE A and B can be placed on top of each other or have a gap between them. In the following, the HOEs are chosen to be placed on top of each other due to the mapping issues mentioned in Sect. 3.2. Both HOEs can have a curvature within the constraint that they may not "stick out" of the polymer or glass material. In most cases, the HOEs are placed close to the flatter curvature  $R_1$  or  $R_2$  since this is assumed to ease manufacturing requirements. This is illustrated in Fig. III.13, where the front side is completely flat  $R_1 = \infty$ . If both, the front and backside, are flat, the refractive lens is not considered to have an optical function in terms of SPH or

AST and is therefore referred to as a "flat sheet of polymer or glass" instead of "refractive lens" henceforth. In some cases, one of the surfaces of the refractive lens is aspherical. In the examples considered later, the asphere (ASPH), if present, is always placed on the backside of the refractive lens to conform to current spectacle lens manufacturing practice [31, 32]. The ASPHs used are conic section ASPHs and parameterize the surface shape  $z(x, y)$  as

$$z(x, y) = z(h) = \frac{\frac{1}{R_2}h^2}{1 + \sqrt{1 - (\frac{1}{R_2}h)^2}} + a_1h^4 + a_2h^6 + a_3h^8 + \dots \quad (\text{III.21})$$

with  $h = \sqrt{x^2 + y^2}$  denoting the height on the surface. Different from the coefficients  $a_n$  of the HOE parametrization, the coefficients of the ASPH can be initialized as zero. This is because the resulting surface is spherical with the intended curvature and therefore relatively close to the desired optical function in terms of SPH and AST, which makes convergence of the optimization more likely. This means that possible variable parameters for the optimization are the coefficients of the global polynomials describing the surface grating period distribution of the two HOEs, the refractive lens curvatures  $R_1$  and  $R_2$ , the coefficients of the ASPH, the center thickness of the refractive lens  $D$  and the curvature, separation and positioning of the HOEs within the refractive lens.

#### Merit function

For the purpose of optimization, it is necessary to formulate a merit function, which describes the desired optical performance of the spectacle lens as well as other constraints such as lens thickness. The specific formulation of the merit function differs by the type of spectacle lens application, the desired prescription and by which optical components are included in the optical system. All optical performance contributions and parameter restriction contributions to the merit function are valid for all gaze directions of the eye and therefore need to be expressed for each of them. Possible optical performance criteria include how well the prescription target values of SPH and AST are met and how large the CE is. Possible parameter restriction contributions include whether or not the local volume grating periods are within the interval for high DE. The volume grating period constraint for HOEs A and B can be expressed as

$$M_{\Lambda,i} := a_{i,1} \left( \left| \Lambda_{\text{vol,HOE A}} - 2.35\mu\text{m} \right| - 0.35\mu\text{m} \right) + a_{i,2} \left( \left| \Lambda_{\text{vol,HOE B}} - 2.35\mu\text{m} \right| - 0.35\mu\text{m} \right)$$

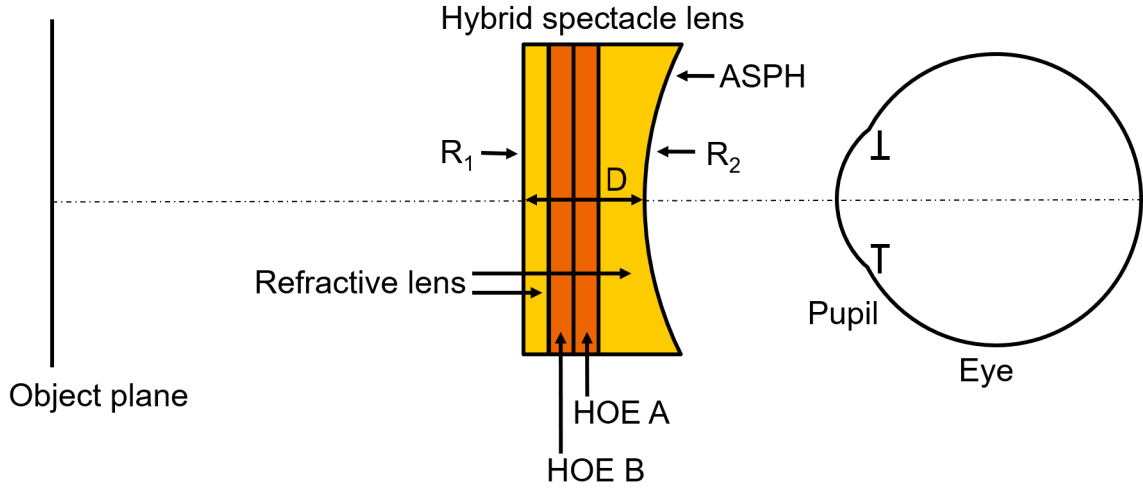


**Figure III.13.** Illustration of all possible optical components used in the investigated holographic-refractive hybrid spectacle lens designs. A HOE tandem consisting of HOEs A and B is embedded into a refractive lens with curvatures  $R_1$  and  $R_2$ , center thickness  $D$  and optionally an ASPH on one surface. In the special case of a purely holographic spectacle lens, the surfaces of the refractive lens are flat and considered not to have any optical function in terms of SPH or AST and is therefore referred to as a "flat sheet of polymer or glass" instead of "refractive lens". The object plane here represents an object plane at infinity as typically used for SVSLs and is therefore drawn as a plane without curvature.

(III.22)

with  $a_{i,n}$  denoting weights to scale the merit function terms. This term penalizes volume grating periods that lie outside of the interval of 2.0 to 2.7  $\mu\text{m}$  (negative values for  $M_{\Lambda,i}$  are considered zero). The merit function terms describing how well the SPH and AST prescription is fulfilled and how large CE is, can be expressed as

$$M_{\text{imaging},i} := a_{i,3}(\text{SPH}_{\text{current}} - \text{SPH}_{i,\text{target}}) + a_{i,4}(\text{AST}_{\text{current}} - \text{AST}_{i,\text{target}}) + a_{i,5}\text{CE}_{\text{current}}. \quad (\text{III.23})$$

In some cases, an additional merit function term can be defined to limit the deflection angle  $\alpha_{\text{deflection,HOE tandem}}$  of the HOE tandem, which can have a stabilizing effect on the convergence of the optimization:

$$M_{\text{deflection,HOE tandem},i} := a_{i,6}(|\alpha_{\text{deflection,HOE A}} + \alpha_{\text{deflection,HOE B}}| - \alpha_{\text{budget}}) \quad (\text{III.24})$$

with  $\alpha_{\text{budget}}$  being an allowed HOE tandem deflection angle offset, which is chosen depending on the lens diameter and prescription value. This term penalizes deflection an-

gles that do not lie within  $-\alpha_{\text{budget}} < \alpha_{\text{deflection,HOE tandem}} < \alpha_{\text{budget}}$  with  $\alpha_{\text{deflection,HOE tandem}}$  being the sum of the deflection angles of both HOEs (negative values of  $M_{\text{deflection},i}$  are considered zero). The full merit function for an arbitrary gaze direction  $i$  is then

$$M_i := M_{\Lambda,i} + M_{\text{imaging},i} + M_{\text{deflection,HOE tandem},i}. \quad (\text{III.25})$$

It should be noted that the weights  $a_{i,n}$  as well as the target values for SPH and AST,  $\text{SPH}_{i,\text{target}}$  and  $\text{AST}_{i,\text{target}}$ , can vary between different gaze directions. For the weights  $a_{i,n}$  this can be done to prioritize e.g. the center gaze direction, which is assumed to be used more than the others, over oblique gaze directions. For the  $\text{SPH}_{i,\text{target}}$  and  $\text{AST}_{i,\text{target}}$ , this can be done e.g. to realize a PAL optical function. By comparison, for a SVSL the SPH and AST target values correspond to the exact prescription values. Merit function terms that do not depend on the viewing directions like the lens edge thickness  $s_{\text{edge}}$  can be formulated as follows:

$$M_{\text{edge}} := a_7 (s_{\text{edge,current}} - s_{\text{edge,target}}). \quad (\text{III.26})$$

Geometrical constraints e.g. that the front and back surface should not intersect below the desired surface height can either be implemented as merit function terms like the edge thickness with very large weights  $a_n$ , or by limiting the allowed value range for the variable parameters so that these constraints cannot be violated in the first place. The full merit function including the contributions of all gaze directions  $i$  and the terms independent of gaze direction is then given as

$$M := \sum_i M_i + M_{\text{edge}}. \quad (\text{III.27})$$

#### Optimization

The optimization process is conducted within an optical design software. As a first step, the components of the optical system are chosen, e.g. for a hybrid lens the refractive lens and the HOE tandem are required. This step includes setting the initial values for these components as previously discussed and a declaration, which parameters are variable during the optimization process. In a second step, the merit function is tailored to the desired optical performance in terms of target prescription and lens type (SVSL / PAL) following the guidelines presented in the previous paragraphs. E.g. in the case of a

### III Holographic optical element design method for spectacle lenses

---

PAL this includes defining the SPH target values either based on a refractive PAL or by computing a desired curve of add power over the lens surface.

The optical design software then uses a least-squares solver to minimize the merit function by iteratively changing the values of the variable parameters. At each step, the merit function is evaluated in the following way: a discrete set of principal rays that samples the entire lens surface is defined at the rotational center of the eye. The principal rays are then traced through the optical system in reverse i.e. from the eye to the object plane. For SVSLs, the object plane is placed at infinity because the prescription of an SVSL is meant to correct human vision at unaccommodated distances. For PALs, the object plane is chosen so that for each gaze direction the distance between the object plane is the inverse of the add power because a PAL is meant to correct human vision in accommodated distances as well. This is shown for a sample gaze direction of a hPAL in Fig. III.14. For each intersection point between a principal ray and the object plane, denoted as  $C_{\text{int}}$  in the Fig., a parallel bundle of rays is defined and traced through the hPAL to the rotational center of the eye. The width of the ray bundle is limited by the pupil of the eye. Because of reciprocity, it is ensured that the principal ray, which is at the center of the bundle, intersects the rotational center of the eye. This process of tracing the rays back and forth ensures that the sampling of intersection points  $C_{\text{int}}$  on the object plane, from which the parallel ray bundles are started, corresponds directly to the desired sampling of principal rays over the lens surface. The SPH, AST and CE of each ray bundle are then evaluated with respect to the vertex sphere as described in Chapt. II for refractive spectacle lens design. Because the ray tracing data for the principal rays is available already, the volume grating periods  $\Lambda_{\text{vol}}$  and deflection angles  $\alpha_{\text{deflection,HOE}}$  are directly calculated as described earlier in this section. With all relevant variables known, the merit function is then evaluated. The variable parameters are then varied by the least-squares solver and the merit function is evaluated again using the same process detailed above.

The optimization procedure described above can be referred to as a one shot optimization as there is no user interaction with the optimization procedure after the merit function and variable parameters have been defined. In some cases, especially the ones with relatively low prescription values, such one shot optimizations converge to useful designs. But in other cases, the optimization either does not converge or converges to a local minimum of unsatisfactory performance. These problems can be addressed by step wise optimization procedures in which several one shot optimizations are conducted in sequence with changes made to either the optical system, the variable parameters or the



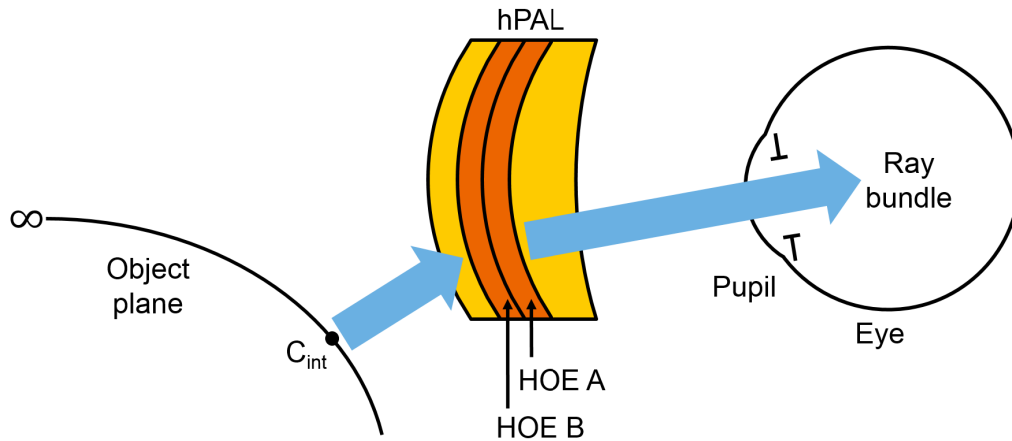


**Figure III.14.** Visualization of the object plane of a hPAL. For parts of the hPAL with add power contributions to SPH, the distance between the hPAL and the object plane is the inverse of the add power. Consequently, in regions with zero add power like the upper part of the hPAL, the object plane is placed at infinity as it is for SVSLs. The intersection point  $C_{int}$  of a principal ray with the object plane is used as the starting point of a parallel ray bundle that is used to calculate the optical performance in terms of SPH, AST and CE of the hPAL.

merit function in between the one shot optimizations. For the optimization tasks described within this thesis, a step wise optimization strategy has been found to solve this issue and improve optimization results: When optimizing holographic-refractive hybrid SVSLs that include an ASPH, it is advantageous to first optimize the base curvatures of the refractive lens and the parameters of the HOE tandem without the ASPH to a prescription SPH value that is about 90% of the final intended SPH while leaving all AST terms out of the merit function. In a second optimization step, the prescription is then updated to the intended SPH and AST values and the coefficients of the ASPH are included in the variable parameters.



## IV. Holographic and hybrid spectacle lens designs

This chapter discusses a variety of holographic and hybrid spectacle lenses that have been designed with the tool chain presented in Chapt. III. Sect. 4.1 is devoted to single vision spectacle lenses (SVSLs) and discusses two sample prescriptions of -4 dpt power (SPH) and 0 dpt astigmatism (AST) and -8 dpt SPH and 0 dpt AST. For SVSLs, the goal is to investigate if the use of holographic optical element (HOE) tandems in either holographic or refractive-holographic hybrid SVSL designs can yield improvements in terms of reduced color error (CE) or lens thickness. Sect. 4.2 discusses progressive addition lenses (PALs) and presents two sample prescriptions, 2.0 and 2.5 dpt add power. For PALs, the goal is to investigate if a refractive PAL that is defined by its varying curvature over the lens surface can be replaced by a purely holographic PAL (hPAL).

### 4.1. Holographic and hybrid single vision spectacle lenses

This section is based on Ref. [189] and discusses holographic and hybrid SVSLs with two sample prescriptions of -4 dpt SPH and 0 dpt AST and -8 dpt SPH and 0 dpt AST. Refractive spherical and aspherical SVSL designs with a prescription of -4 dpt SPH and 0 dpt AST are presented in Chapt. II. Here, purely holographic as well as hybrid designs with and without aspheres (ASPHs) are presented. This allows a detailed comparison between the performance of HOEs and ASPHs. The other prescription of -8 dpt SPH and 0 dpt AST is chosen to evaluate the performance of hybrid SVSLs for high prescription values for which CE is a significant problem. For all designs the goal is to achieve better optimization compromises between SPH error, AST error, CE and lens thickness than what can be achieved with refractive SVSLs. The design tool chain presented in Chapt. III ensures that all resulting SVSL designs fulfill the requirements for high DE.

### 4.1.1. SVSL prescription -4 dpt SPH and 0 dpt AST

Here, the prescription of -4 dpt SPH and 0 dpt AST is chosen because it is a relatively common prescription while featuring notable levels of CE. The refractive SVSLs of this prescription are shown in Fig. II.5 in Chapt. II. To establish an understanding on how the performance of purely holographic SVSLs differs from refractive ones, the tool chain described in Chapt. III is used to design a purely holographic SVSL. This SVSL consists of a HOE tandem, which is embedded in a flat sheet of the spectacle lens polymer with refractive index 1.59 and Abbe number 41.11 that was already used for the refractive SVSLs of the same prescription. The flat sheet of polymer affects the rays according to Snell's law, but does not introduce notable contributions to SPH error, AST error or CE. The SVSLs performance can therefore be considered to be purely holographic. In this case, the only variable parameters are the coefficients of the global polynomials  $p(x, y)$  describing the surface grating periods of the HOEs. The weights of the merit function are chosen to target the same level of SPH error as the spherical SVSL of the same prescription shown in Fig. II.5(a). CE is not constrained in the merit function, because without the option of refractive holographic dispersion compensation, the only ways to limit CE are the dispersion compensation of the HOE tandem that is used without explicitly writing it into the merit function or to reduce the achieved SPH value since SPH correlates with CE. The resulting distributions of SPH error, AST error and CE over the lens surface are shown in Fig. IV.1(a)-(c), respectively, with SPH error and AST error being plotted in the same color scale as in Fig. II.5. SPH error has a maximum of approximately 0.6 dpt on the lens edge, which is a bit lower than the maximum SPH error of approximately 0.8 dpt of the spherical, refractive SVSL. AST error, however, has a maximum of approximately 1 dpt on the lens edge, which is considerably higher than the maximal AST error of the spherical, refractive SVSL of approximately 0.3 dpt. This high level of AST error is not expected and could be linked to the fact that, different from the refractive SVSLs, holographic SVSLs are not rotationally symmetric. For a refractive SVSL the parametrization of all surfaces is typically chosen with radial parameters and the origin coinciding with the center of the lens. For the holographic SVSL investigated here, such a parametrization is not possible since due to the deflection angle of the first HOE, the center points of the two HOEs do not overlap. The results achieved with the parametrization used here can also not be improved by increasing the number of coefficients of the global polynomial in Eq. III.7, since the higher order coefficients are negligible already. However, as stated in Sect. 3.4, it is certainly possible that other HOE parametrizations lead to slightly improved results.

CE is plotted in a different color scale than the spherical, refractive SVSL, because it has a maximum CE of approximately -10, which is one order of magnitude more and the opposite direction. Stronger and inverted CE is expected for a holographic SVSL as this behavior is known from technical optics [117]. While the holographic SVSL shown here clearly is not an attractive design, it helps to understand the consequences of using HOE tandems in SVSL design: increased AST error and increased, inverted CE that is used for dispersion compensation in holographic-refractive hybrid SVSLs in the following.

The insights gained from evaluating the holographic SVSL can be used to design hybrid SVSLs. The full optical system of a hybrid lens as a HOE tandem embedded into a refractive lens that includes an ASPH is shown in Fig. III.13. To isolate the performance increase of the ASPH from the benefits of using a hybrid design, the first hybrid design to be evaluated does not include an ASPH i.e. is a spherical lens. The variable parameters in this case are the front and back curvatures  $R_1$  and  $R_2$  as well as the coefficients of the global polynomials  $p(x, y)$  describing the HOEs. The CE of the holographic SVSL design already suggests that a hybrid device with about 10% of the overall SPH coming from the HOE tandem can achieve dispersion compensation. But the performance of the holographic SVSL design also suggests that SPH provided by the HOE tandems comes with more AST error than SPH provided by a refractive lens. Therefore, the merit function for the hybrid SVSL does not enforce perfect dispersion compensation, but only penalizes CE above the perception threshold, which is 0.4 due to the normalization used. The resulting SPH error, AST error and CE of such a hybrid SVSL are shown in Fig. IV.1(d)-(f). The maximal SPH error is approximately 0.7 dpt, which is comparable to the SPH error of the refractive SVSL with an ASPH shown in Fig. II.5(d) and 0.1 dpt lower than the SPH error of the refractive, spherical SVSL shown in Fig. II.5(a). The maximal AST error is approximately 0.14 dpt, which is comparable to the AST error of the refractive spherical SVSL shown in Fig. II.5(b), but higher than the AST error of the refractive SVSL with an ASPH shown in Fig. II.5(e). The maximal CE is at the perception threshold of 0.4, while the CE of the refractive SVSLs shown in Fig. II.5(c) and (f) are 1. This hybrid SVSL design shows two interesting properties of hybrid SVSLs. Looking at the SPH error and AST error, the optimization compromise achieved between the two is not as good as the one of a refractive SVSL with an ASPH, but considerably better than the one of a refractive, spherical SVSL. This indicates that the degrees of freedom provided by the HOE tandem have a similar influence on the optimization compromise as an ASPH and can partially replace it. The other interesting property is that dispersion compensation works in hybrid

## IV Holographic and hybrid spectacle lens designs

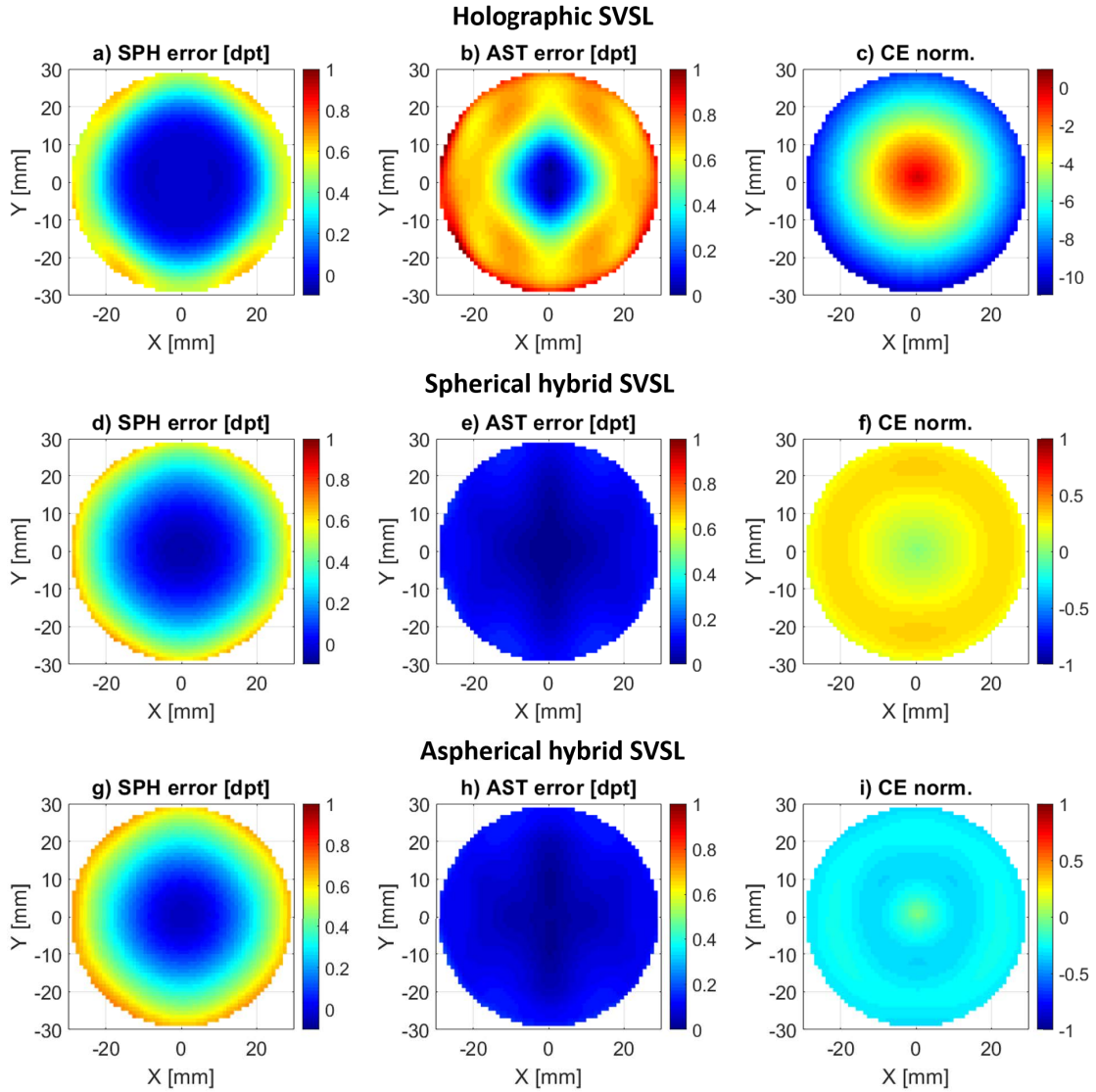


**Figure IV.1.** SPH error, AST error and normalized CE of holographic and hybrid SVSL designs of the prescription -4 dpt SPH and 0 dpt AST. A purely holographic SVSL that consists of a HOE tandem embedded into a flat sheet of polymer without notable contributions to SPH error, AST error and CE is shown in parts (a)-(c). Compared to a spherical, refractive SVSL of the same prescription, SPH error is decreased by approximately 0.2 dpt, AST error is increased by approximately 0.7 dpt and CE is inverted and increased by a factor of 10. Adding a HOE tandem to a spherical, refractive SVSL to create a hybrid SVSL as done in (d)-(f), achieves a reduced SPH error, AST error and CE relative to a spherical, refractive SVSL. Relative to a refractive SVSL that includes an ASPH, however, only CE is reduced. Hybrid SVSLs with ASPHs allow to achieve strong thickness reductions e.g. from 4.5 mm (refractive SVSL with ASPH) to 3.8 mm for a hybrid SVSL design that is shown in parts (g)-(i). SPH error, AST error and CE of the hybrid SVSL shown in (g)-(i) are similar to the hybrid SVSL shown in (d)-(f) aside from the sign switching of CE.

SVSL and CE can be reduced to the perception threshold despite the more complicated optical system with different gaze directions.

Because the previous hybrid SVSL design indicates that HOE tandems can be used to strongly reduce CE and ASPHs are even better than HOE tandems at improving the optimization compromise between SPH error and AST error, it makes sense to combine the two approaches and to design hybrid SVSLs that include ASPHs to achieve the best possible optimization compromise between SPH error, AST error and CE. For such a hybrid SVSL, the variable parameters include the front and back curvatures  $R_1$  and  $R_2$ , the coefficients of the ASPH from Eq. III.21 as well as the coefficients of the global polynomials  $p(x, y)$  describing the HOEs. In lens design practice, ASPHs are often used to reduce the lens thickness rather than to increase the optical performance in terms of SPH error and AST error. HOE tandems also have the potential to reduce the lens thickness since they are thin films with a typical thickness of only 10 to 100  $\mu\text{m}$ . To investigate this, a merit function is written that prioritizes thickness decreases over SPH error, AST error or CE reductions relative to the hybrid SVSL shown in Fig. IV.1(d)-(f). The resulting distributions of SPH error, AST error and CE over the lens surface of a hybrid SVSL design that includes an ASPH are shown in Fig. IV.1(g)-(i). Because the question at hand is to evaluate if the HOE tandem improves the performance of a refractive SVSL with an ASPH, the SVSL presented in Fig. II.5(d)-(f) is an appropriate benchmark. In this comparison, SPH error is approximately the same for both designs, AST error is increased to 0.14 dpt for the hybrid design and CE is -0.4 for the hybrid design. The increased AST error is still relatively close to the smallest tolerance for spectacle lenses AST of 0.09 dpt [190] and should therefore be of little relevance. CE is again below the perception threshold of 0.4, but inverted its direction. Assuming that CE impairs vision in a similar fashion irrespective of CE sign, this would still be below the perception threshold. The edge thickness of the hybrid SVSL is reduced to 3.8 mm, which is a significant improvement relative to the edge thickness of 4.5 mm of the refractive SVSL with ASPH. This clearly shows that HOE tandems can be used to decrease the thickness of SVSL designs. In fact the change in CE direction indicates that in this example the optimization converged to a result with maximal SPH contribution from the HOE tandem. The mechanism here is that more SPH being contributed by the HOE tandem leads to lower CE, increased AST error and decreased thickness since less SPH needs to be contributed by the refractive parts of the lens, which translates to lower curvatures being used.

### 4.1.2. SVSL prescription -8 dpt SPH and 0 dpt AST

While the investigations of SVSLs with a prescription of -4 dpt SPH and 0 dpt AST already provide a lot of insights into the benefits of using HOE tandems in SVSL designs, it is interesting to evaluate other, stronger prescriptions where CE is of even greater importance. For this purpose, a prescription of -8 dpt SPH and 0 dpt AST is considered. As a benchmark device, a refractive SVSL that includes an ASPH is designed using the tool chain. This time another standard spectacle lens polymer with refractive index 1.73, Abbe number 32.15 is used since typically higher refractive index materials are used for higher prescription values. The resulting SPH error, AST error and CE over the lens surface are shown in Fig. IV.2(a)-(c). The maximal SPH error is approximately 1.4 dpt, the maximal AST error is approximately 0.06 dpt and the maximal CE is approximately 2.5 in the same normalization used for the -4 dpt SPH prescription SVSLs, which is far above the level of the CE of a SVSL with a prescription of -4 dpt SPH and 0 dpt AST. The edge thickness is 5.7 mm.

To investigate whether or not the addition of a HOE tandem can improve the optimization compromise in terms of SPH error, AST error, CE and edge thickness, a hybrid SVSL made from the same material and an ASPH is designed using the tool chain. For SPH error, AST error and edge thickness, the goal is to reduce them below the results of the refractive SVSL, while for CE the goal is to achieve a CE of 1, which corresponds to the CE of a -4 dpt SPH SVSL that is known to be uncritical from practice. The resulting distributions of SPH error, AST error and CE over the lens surface are shown in Fig. IV.2(d)-(f). SPH error remained relatively close to the refractive SVSL with a maximal value of 1.5 dpt. AST error is slightly increased to 0.14 dpt, which is still very close to the smallest tolerance for spectacle lenses AST of 0.09 dpt [190] and should therefore be of little relevance. CE is, as intended, reduced to a maximal value of 1. The edge thickness is decreased by 0.2 mm to a value of 5.5 mm. Overall, this shows that the optimization compromise can in fact be strongly improved by adding HOE tandems to SVSL designs. It should be noted though, that strong requirements on CE reduction make it harder to achieve improvements in SPH error and AST error. But for the users reducing the very noticeable CE of a -8 dpt SPH SVSL to the uncritical one of a -4 dpt SVSL is certainly a relevant improvement.

To assess how well the volume grating periods  $\Lambda_{\text{vol}}$  were kept in the range for high DE, the volume grating periods of HOE A and HOE B of the HOE tandem are plotted over the lens surface in Fig. IV.3 (a) and (b), respectively. The color plots indicate that the



volume grating periods are well within the proposed range of 2.0 to 2.7  $\mu\text{m}$ . To estimate how this affects the color impression of the user, the median DE at three sample wavelengths (430 nm, 546 nm, 620 nm) for the required angular bandwidth are calculated as a function of the volume grating period using the data from FMM simulations. Multiplying the median DE of HOE A and HOE B at each lens position depending on the local volume grating period then yields the expected color impression when looking at a white object, which is shown in Fig. IV.3 (c). The minimum median DE achieved here after the multiplication of the DE of HOE A and HOE B is approximately 0.7. The resulting color impression is very homogeneous across the lens surface, but features a greenish tint that may be perceived as disturbing or like sunglasses. The greenish tint is caused by the maximum DE being in the green part of the wavelength bandwidth.

The optimization compromise presented here can be varied further by changing the refractive index of the refractive lens material. One possibility would be to decrease the refractive index but keep the SPH contribution of the refractive lens constant. In that case, the lens curvature and thickness would increase as the same SPH contribution has to be realized with the lower refractive index. In turn, SPH error would increase due to the increased lens curvature. The only benefit would be that CE would be reduced further due to the reduced dispersion of the lower refractive index lens material. In summary, this is not attractive as CE already is lowered considerably and the both SPH error and lens thickness would increase. Another possibility would be to decrease the refractive index and increase the SPH contribution from the HOE tandem. In this case, CE would decrease, but due to the increased SPH contribution of the HOE tandem, AST error would increase as well. This would likely increase AST error to non-negligible values and is therefore not an attractive approach. In fact, it would be attractive to further increase the refractive index to lower the lens curvature, thickness and consequently SPH error, but this isn't practical considering the availability of approved materials for SVSL manufacturing.

## IV Holographic and hybrid spectacle lens designs

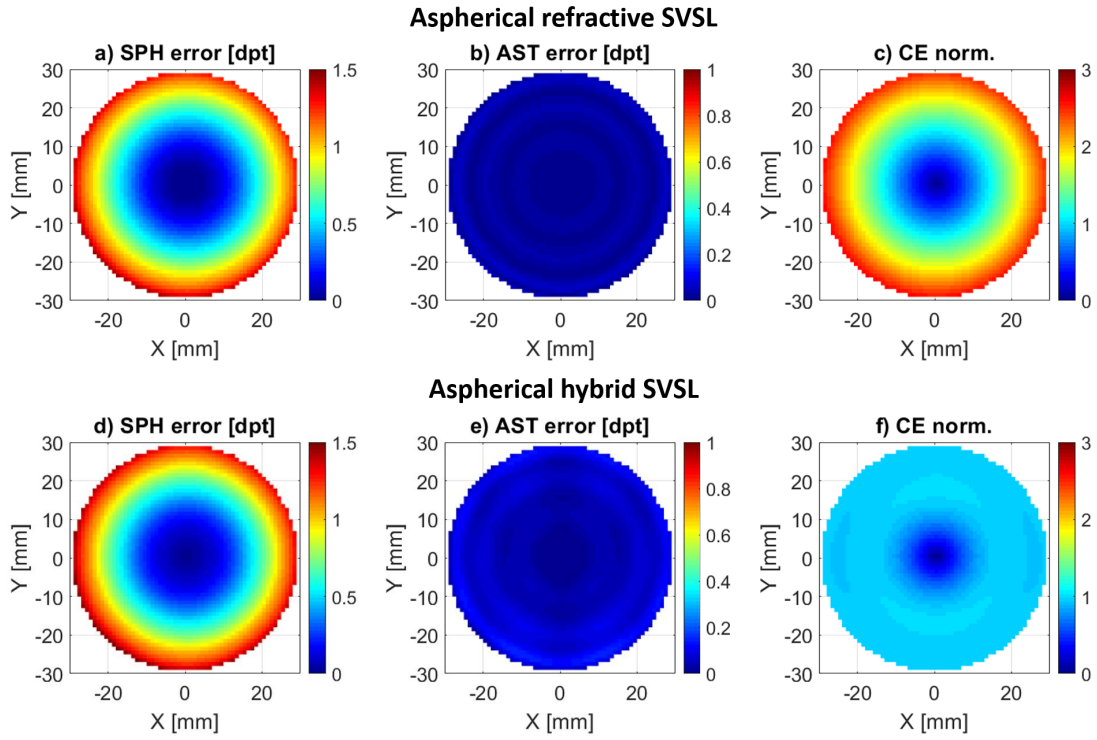


**Figure IV.2.** Comparison of SPH error, AST error and CE of a refractive (a-c) and a hybrid SVSL design (d-f) for a prescription of -8 dpt SPH and 0 dpt AST. Both designs include an ASPH. Both designs perform approximately the same in terms of SPH error and AST error, while the hybrid design achieves a much lower CE of 1, which is the same CE as a refractive SVSL with a prescription of -4 dpt SPH due to the normalization used.

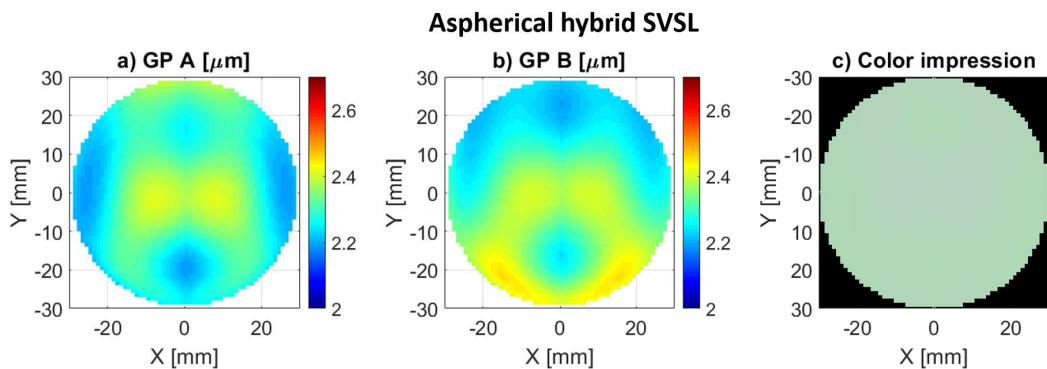


**Figure IV.3.** Volume grating periods of HOE A (a) and HOE B (b) as well as the overall color impression (c) plotted across the lens surface of the -8 dpt hybrid SVSL. The volume grating periods of both HOE A and HOE B are well within the range for high DE of 2.0 to 2.7  $\mu\text{m}$ . The color impression is homogeneous across the lens surface and has a greenish tint.

## 4.2. Holographic progressive addition lenses

The research question investigated in this section is whether or not it is possible to design more complicated optical functions than SVSLs using the tool chain described in Chapt. III. The example studied here is to replicate the optical function of a refractive PAL with an hPAL. The results presented here have been published in Refs. [191, 192]. Prescriptions of 2.0 dpt and 2.5 dpt add power with no further refractive errors outside of presbyopia are investigated here and compared to refractive PALs of the same prescription. Because it is not clear a priori if the optical function of a PAL in terms of SPH and AST can be replicated while enforcing the requirements for high DE and dispersion compensation, the corresponding data is discussed in detail. A possible application for such an hPAL is to combine the hPAL that corrects the users presbyopia with an inexpensive spherical lens that corrects the users other refractive errors. Such a hybrid device would then address a wide range of prescriptions without requiring the complicated freeform surfaces used in current PAL designs.

### 4.2.1. hPALs with 2.0 dpt add power

A 2.0 dpt add power hPAL is designed using the tool chain with the goal of replicating the optical function of a benchmark refractive PAL. The SPH and AST distributions of the refractive PAL of the corresponding prescription are shown in Fig. II.6(a) and (b), respectively. The hPAL is made up of a HOE tandem embedded into flat sheets of polymer. Since the polymer sheet has no noteworthy impact on SPH or AST, the only variable parameters relevant for the optimization are the coefficients of the global polynomials  $p(x, y)$  describing the two HOEs. The merit function is set up analogous to the ones of SVSL with the exception that the target values of Eq. III.23 of the merit function are no longer constant over the lens surface, but vary. For each gaze direction  $i$ , the target values for SPH and AST are the values of the same gaze direction for the benchmark refractive PAL. To express that the merit function does not force high AST, but merely allows as much AST as the benchmark PAL, Eq. III.23 is rewritten that the AST targets are marked as smaller or equal rather than equal.

To evaluate whether or not such a hPAL design achieves the requirements for high DE, the volume grating periods are plotted over the lens surface for both HOEs in the tandem, HOE A and HOE B, in Fig. IV.4(a) and (b), respectively. For both HOE A and HOE B, the desired range of the volume grating period between  $2.0 \mu\text{m}$  and  $2.7 \mu\text{m}$  is color coded

#### IV Holographic and hybrid spectacle lens designs

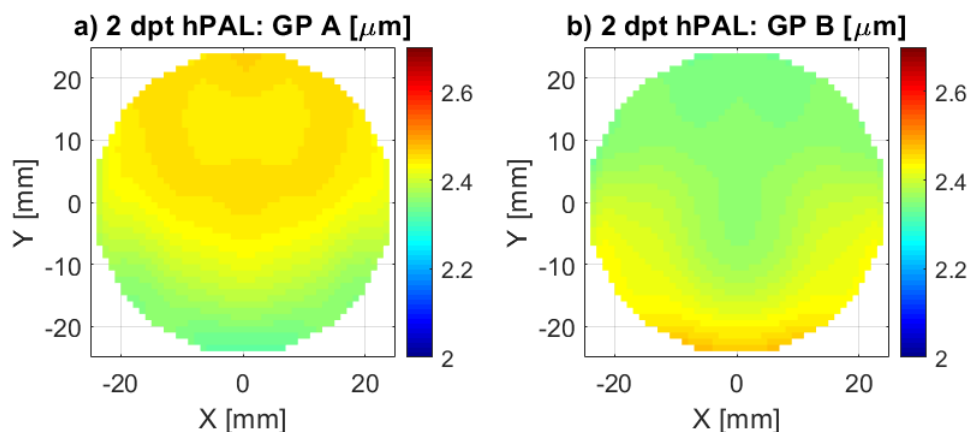


**Figure IV.4.** Volume grating period distribution over the lens surface for HOE A (a) and HOE B (b) of the HOE tandem of the hPAL. The color code shows that the volume grating periods vary by less than  $\pm 0.1 \mu\text{m}$  around the desired value of  $2.4 \mu\text{m}$ .

from blue to red. The colors clearly show that the variation of the volume grating periods over the hPAL surface is less than  $\pm 0.1 \mu\text{m}$  around the desired value of  $2.4 \mu\text{m}$  in both cases. This means that the requirements for high DE in terms of angular and wavelength bandwidth are achieved. The angular bandwidth is centered on the principal ray for all gaze directions thanks to the grating period parametrization method of the tool chain.

The hPAL is a purely holographic device, so CE has to be limited by dispersion compensation of the HOE tandem rather than by refractive-holographic dispersion compensation as in hybrid SVSLs. This is investigated by calculating CE of the hPAL with the same normalization as the SVSLs presented earlier in this chapter. The rationale here is that CE of up to 1 would correspond to the CE of a -4 dpt SPH SVSL, which is known to be uncritical from practice. Larger CE might be a problem, at least to users with a high individual sensitivity to CE. The resulting distribution of CE over the lens surface is shown in Fig. IV.5. While the maximal CE is above 1, this is only the case in the left and right bottom parts of the lens with  $-20 \text{ mm} < x < -10 \text{ mm}$  as well as  $10 \text{ mm} < x < 20 \text{ mm}$  and  $-20 \text{ mm} < y < -10 \text{ mm}$ . Comparison with the AST distribution of the refractive PAL in Fig. II.6(b) yields that these regions have very high AST values and are therefore not required to achieve pristine optical performance. Outside of these regions, CE is below 1, especially in the the progressive corridor at  $-5 \text{ mm} < x < 5 \text{ mm}$  and  $-15 \text{ mm} < y < 0 \text{ mm}$ , where CE even takes negative values. Because the negative values are above -1, it can be assumed that the CE there has no negative impact on the user. In conclusion, dispersion

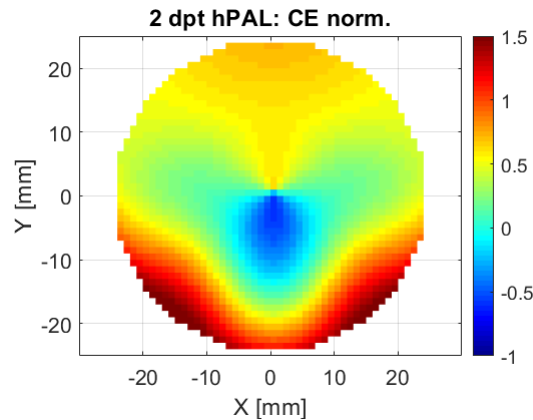


**Figure IV.5.** CE of the hPAL over the lens surface. CE is normalized so that a value of 1 corresponds to the maximal CE of a -4 dpt SPH SVSL, which is known to be uncritical from practice. Outside of regions with high AST, CE is below 1.

compensation of the HOE tandem works as desired to limit CE to acceptable values that are comparable to a refractive SVSL with a prescription of -4 dpt SPH and 0 dpt AST.

The SPH and AST distribution of the hPAL over the lens surface is shown in Fig. IV.6(a) and (b), respectively. Comparison with the refractive PAL shown in Fig. II.6 yields that the hPAL qualitatively replicates the SPH and AST distributions of the refractive PAL. In particular, the continuous increase in SPH over the lens surface and the zones of low AST in the near and far zone as well as in the progressive corridor.

In order to quantitatively compare the hPAL with the refractive PAL, Fig. IV.7 shows their SPH and AST along cuts of the lens surface. Part (a) shows the central cut ( $x = 0$  mm) of the lens, which evaluates the performance in the progressive corridor as well as the center of the near and far viewing zones. Part (b) shows the  $y = -23$  mm cut, which evaluates the near viewing zone. In the progressive corridor shown in part (a), the SPH gradient of the hPAL is about 0.1 dpt per mm, which is very close to the refractive PAL's SPH gradient of 0.13 dpt per mm. The maximal AST of the hPAL of 0.16 dpt in the progressive corridor is a bit higher than the one of the refractive PAL of 0.04 dpt. Evaluating the near zone shown in part (b) shows that while the hPAL has a slightly lower SPH distribution with a maximal SPH of 2.0 dpt for the hPAL and 2.2 dpt for the PAL, AST is also strongly reduced with a minimal AST of 0.16 dpt for the hPAL and 0.31 dpt for the PAL. It is especially interesting that the gradient of AST along  $x$  is much lower for the hPAL, which is an indication that the provided near zone is preferable to the one of the PAL.

These results show that an hPAL can be designed to have a qualitatively comparable optical performance in terms of SPH and AST as a refractive one. At the same time, the

#### IV Holographic and hybrid spectacle lens designs

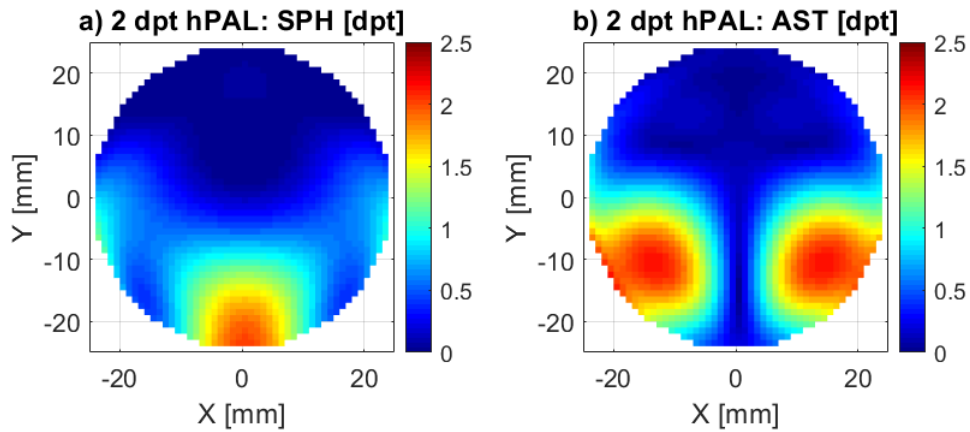


**Figure IV.6.** SPH (a) and AST (b) distributions over the lens surface of a 2 dpt add power hPAL design. Both profile qualitatively match the SPH and AST distribution of a refractive PAL of the same prescription.

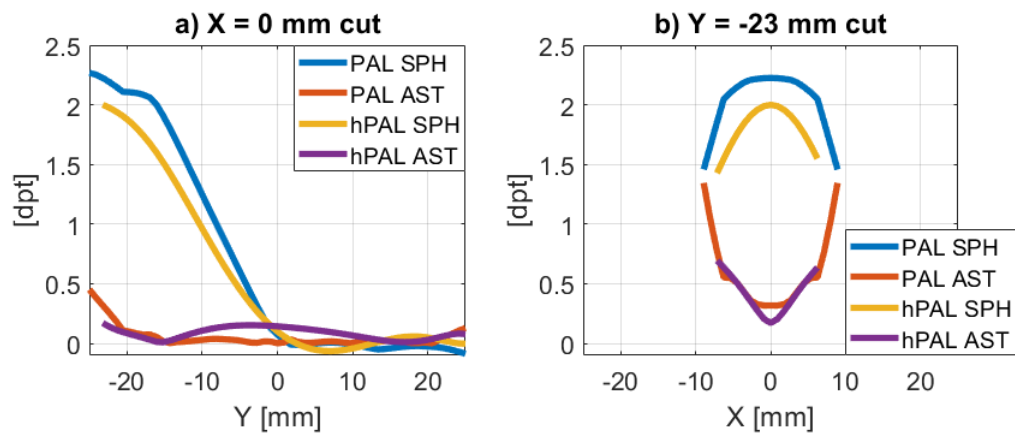


**Figure IV.7.** Comparison of the SPH and AST of the hPAL and PAL along a cut at  $x = 0$  mm (a) and a cut at  $y = -23$  mm (b). Part (a) shows that the SPH gradient of SPH of the hPAL is 0.1 dpt per mm, which is relatively close to the SPH gradient of 0.13 dpt per mm with AST being low in both cases. Part (b) shows that while the hPAL does not reach the maximal SPH value of the PAL, it has considerably lower AST and a much lower AST gradient along  $x$ .

requirements for high DE as well as low CE due to dispersion compensation in the HOE tandem can be upheld. The shape of the SPH and AST distributions in the near zone suggest that due to an increased number of free parameters, HOE tandems might be able to provide advantageous i.e. lower AST gradients along  $x$ . Additionally, the thickness of the hPAL is only  $25\ \mu\text{m}$  plus a thin polymer substrate, which is significantly less than the thickness of a refractive PAL of several millimeters.

### 4.2.2. hPALs with 2.5 dpt add power

An hPAL with a prescription of 2.5 dpt add power and no further refractive errors to be corrected is designed to evaluate the limitations of the hPAL approach. The SPH and AST distributions over the lens surface of a refractive PAL of the same prescription that serves as a benchmark device, is shown in Fig. IV.8(a) and (b), respectively. The SPH and AST distributions of the hPAL are shown in Fig. IV.8(c) and (d), respectively. Comparison between the hPAL and the PAL yields that the near zone (red area in the SPH plots) of the hPAL is a bit smaller than the one of the PAL. Looking at the AST distributions, however, it is found that the hPAL has much lower AST than the PAL. This includes a much lower maximal AST of approximately 2.8 dpt rather than 3.7 dpt for the PAL as well as progressive corridor being a bit wider for the hPAL. In principle, these findings are an excellent ground to argue that the increased degrees of freedom of the HOE tandem in fact improve the optimization result of the hPAL.

However, the hPAL suffers from large CE. The distribution of CE over the lens surface of the hPAL is shown in Fig. IV.9. The same normalization as before is used, so CE up to 1 is assumed as uncritical. For this hPAL, the maximal CE is above 3 and both the near zone and the progressive corridor feature CE levels considerably above 1 and are therefore potentially disturbing for users. This means that the correlation between add power and CE limits the hPAL design approach to add powers of up to approximately 2.0 dpt. Refractive-holographic dispersion compensation only has a limited potential to circumvent this. Combining a refractive PAL with an hPAL would allow to achieve a locally fitting dispersion compensation i.e. that refractive and holographic add powers stay within a dispersion compensated ratio for all parts of the lens. This approach, however, would jeopardize the goal of replacing the complex free-form surfaces required to fabricate refractive PALs. A possible alternative would be to combine an hPAL design as shown here with a refractive SVSL that corrects the other refractive errors the user might have such as myopia, hyperopia or astigmatism. In the case of hyperopia, dispersion compen-

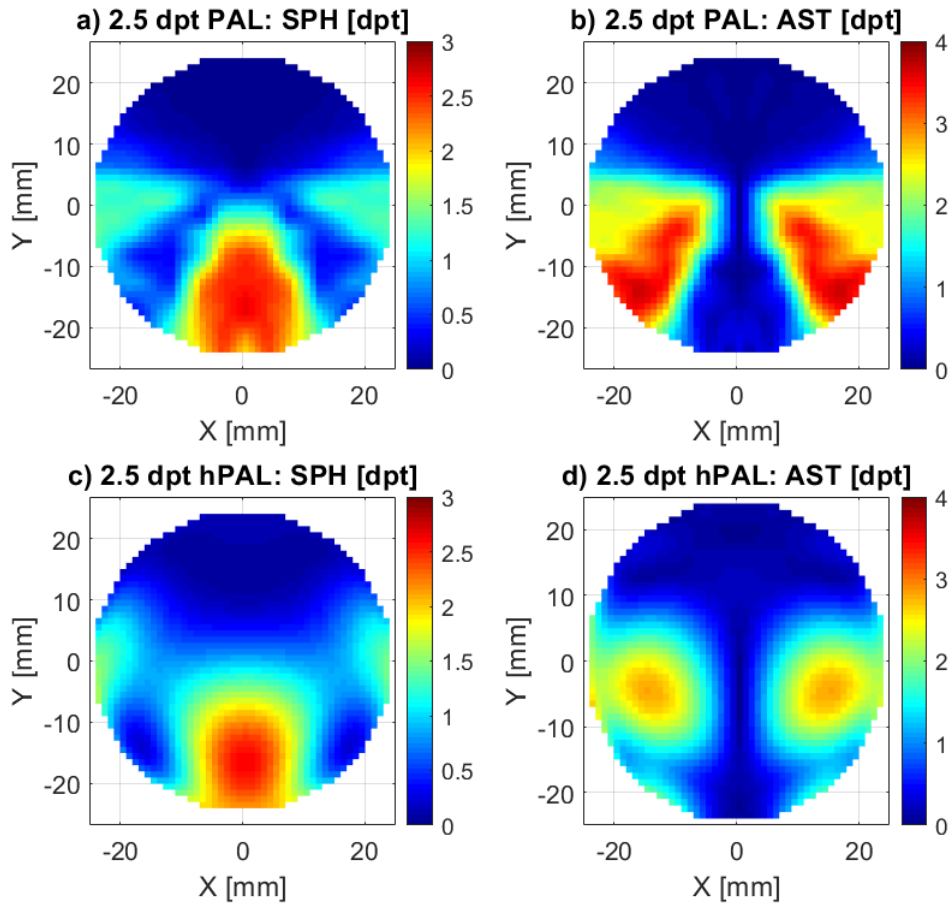


**Figure IV.8.** SPH (a) and AST (b) distributions of a 2.5 dpt add power refractive PAL over the lens surface. The PAL is used as a benchmark device to design an hPAL of the same prescription, whose SPH and AST distributions over the lens surface are shown in (c) and (d), respectively. Comparison between the PAL and the hPAL shows that the hPAL has a smaller near zone (red area in part c), but much lower AST.

sation between the refractive SVSL and the hPAL is possible and would allow to increase the range of accessible add power prescriptions. In the case of myopia, the dispersion contributions of the refractive SVSL and the hPAL have the same sign and would add up rather than to compensate each other. This would lead to even higher CE and means that this hPAL approach is not compatible with correcting notable levels of myopia.



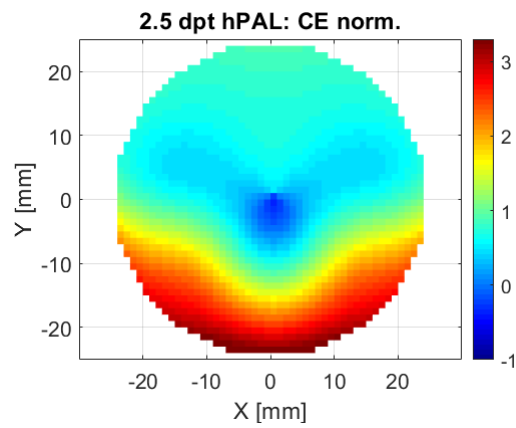


**Figure IV.9.** Distribution of CE of a 2.5 dpt add power hPAL over the lens surface. CE is normalized so that 0.4 corresponds to the perception threshold and 1 corresponds to the CE of a -4 dpt SVSL, which is known to be uncritical from practice. For this hPAL, the maximal CE is above 3 and both the near zone and the progressive corridor feature CE levels considerably above 1 and are therefore potentially disturbing for users.



# V. Summary and Outlook

## 5.1. Summary

In this thesis, several benefits of including HOEs into spectacle lens designs such as the replacement of freeform surfaces for PALs or ASPHs for SVSLs with HOEs as well as CE and thickness reductions in SVSLs have been evaluated. For this purpose, challenges for the use of HOEs in spectacle lenses such as DE requirements or dispersion compensation had to be fulfilled. The requirement of achieving large angular and wavelength DE bandwidth was solved in this thesis by optimizing HOE parameters using rigorous simulations to find a parameter range in which the required bandwidths can be achieved for multiplexed HOEs. Dispersion in purely holographic spectacle lens designs is decreased by using a tandem of two HOEs operating in opposite diffraction orders. In refractive-holographic hybrid spectacle lenses, the dispersion induced by refractive and holographic components can be used to compensate each other. With these challenges solved, a tool chain for the design of arbitrary HOEs in spectacle lens applications was created. This tool chain solves design issues such as optimizing the optical function of the HOEs in terms of SPH error and AST error for all gaze directions of the eye and ensuring that the available DE angular bandwidth is centered on the principal ray for all gaze directions.

Using this tool chain, holographic and hybrid SVSL designs as well as holographic PAL designs were created. For SVSLs, the achieved benefits were CE reductions, thickness reductions and the possibility to replace ASPHs with HOEs. For PALs, the achieved benefits were to replace the free-form required in refractive PALs with the arbitrary optical function of a HOE. In the case of SVSLs, it was shown that CE reductions using HOEs are indeed possible. For example it was possible to reduce CE of a -4 dpt SPH SVSL, which is considered uncritical but above the perception threshold, to below the perception threshold or to reduce the CE of a -8 dpt SPH SVSL to the CE of a -4 dpt SPH SVSL, both without notable increases in other performance parameters such as SPH error or AST error. In fact, incorporating HOEs also reduces the thickness of the lens. When aiming at reducing

the edge thickness of a -4 dpt SPH SVSL, it is possible to reduce the edge thickness of an already optimized SVSL with an ASPH by an additional 16% by including HOEs without notable increases in other relevant performance parameters such as SPH error or AST error. Replacing the ASPH in a refractive SVSL with a spherical and one aspherical surface by a HOE is possible, but the results show that ASPHs are better suited to improve the optimization compromise between SPH error and AST error. Still, the optimization compromise between SPH error and AST error in a spherical SVSL with HOEs is strongly improved compared to a spherical, refractive SVSL. In PAL designs, it is possible to replace the complicated free-form surface with HOEs for add powers up to 2.0 dpt. For larger add powers, CE increases beyond uncritical levels. Because refractive-holographic dispersion compensation works only for SPH contributions of the same sign, combining holographic PALs with refractive hyperopia correction increases the available range of possible add powers, while refractive myopia correction would increase CE and therefore reduce the available range of possible add powers.

### 5.2. Outlook

The results of this thesis show that there are several possibilities to benefit from including HOEs in spectacle lens designs.

While the holographic and hybrid spectacle lens designs presented in this thesis can certainly be manufactured, this remains a challenging task for example in terms of recording high quality HOEs via a holographic printer or embedding HOEs into refractive lenses with high positioning accuracy. Solving these challenges for a prototype would allow to assess the potential of this technology for mass production in a more informed manner as well as to assess potential technological drawbacks such as environmental stability of the HOEs in terms of temperature or humidity, haze from scattering and glare effects from diffraction when unexpected wavelength and angle pairs fulfill the Bragg condition. Looking at other holography applications such as augmented reality (AR) or head-up displays (HUDs) it seems reasonable to expect that haze from scattering is not a problem, but glare effects might play a role.

Looking at potential applications of using HOEs in spectacle lenses, there is a large field of potential applications that has been opened up by this thesis. Especially applications in AR or myopia control can play a vital role in motivating further research into this field. In AR applications, the technology developed here can benefit HOE design for varying SPH

profiles that create different depth perceptions as well as AST error reductions. Such functional design approaches are attractive for AR glasses as well as HUDs. In myopia control, the angular selectivity of HOEs that is a drawback for the applications presented in this thesis can be an important feature. One type of refractive spectacle lenses for myopia control utilizes a tailored Petzval field curvature to move the focal plane in front of the retina for peripheral vision while the focal plane is still on the retina for foveal vision [78, 193, 194]. Of course, this approach is limited to one gaze direction. Here, the angular selectivity of a hybrid SVSL designed with the methods described in this thesis can be used so that for each gaze direction, only a narrow angular spectrum around the principal ray is diffracted. The diffracted rays then form an image on the retina, while the other rays that are only refracted form an image in front of the retina. This way, the functionality of the Petzval curvature myopia control lenses can be extended to work for all gaze directions [195].

## Bibliography

- [1] The Eye Diseases Prevalence Research Group, “The prevalence of refractive errors among adults in the united states, western europe, and australia,” *Archives of Ophthalmology*, vol. 122, no. 4, pp. 495–05, 2004.
- [2] T. Hung, “Epidemiologic study of the prevalence and severity of myopia among schoolchildren in taiwan in 2000,” *Journal of the Formosan Medical Association*, vol. 100, no. 10, 2001.
- [3] L. L.-K. Lin, Y.-F. Shih, C. K. Hsiao, and C. Chen, “Prevalence of myopia in taiwanese schoolchildren: 1983 to 2000,” *Annals of the Academy of Medicine Singapore*, vol. 33, no. 1, pp. 27–33, 2004.
- [4] S.-M. Saw, L. Tong, W.-H. Chua, K.-S. Chia, D. Koh, D. T. Tan, and J. Katz, “Incidence and progression of myopia in singaporean school children,” *Investigative Ophthalmology & Visual Science*, vol. 46, no. 1, pp. 51–57, 2005.
- [5] I. G. Morgan, K. Ohno-Matsui, and S.-M. Saw, “Myopia,” *The Lancet*, vol. 379, no. 9827, pp. 1739–1748, 2012.
- [6] D. A. Atchison, “Spectacle lens design: a review,” *Applied Optics*, vol. 31, no. 19, pp. 3579–3585, 1992.
- [7] J. Alonso and J. Alda, “Ophthalmic optics,” *Encyclopedia of Optical Engineering*, pp. 1563–1576, 2003.
- [8] L. Jones, “Disposable contact lenses: a review,” *Journal of the British Contact Lens Association*, vol. 17, no. 2, pp. 43–49, 1994.
- [9] K. D. Solomon, L. E. F. de Castro, H. P. Sandoval, J. M. Biber, B. Groat, K. D. Neff, M. S. Ying, J. W. French, E. D. Donnenfeld, R. L. Lindstrom, *et al.*, “Lasik world literature review: quality of life and patient satisfaction,” *Ophthalmology*, vol. 116, no. 4, pp. 691–701, 2009.

- 
- [10] W. H. Wollaston, "LXI. On an improvement in the form of spectacle glasses," *The Philosophical Magazine*, vol. 17, no. 68, pp. 327–329, 1804.
- [11] F. Ostwalt, "Ueber periskopische Gläser," *Albrecht von Graefes Archiv für Ophthalmologie*, vol. 46, pp. 475–524, Oct 1898.
- [12] A. Bennett, "Tscherning on best-form lenses," *The Refractionist*, vol. 32, pp. 181–194, 1945.
- [13] M. Von Rohr, "Improvements in toric spectacle glasses," Feb. 2 1911. GB Patent 191021864.
- [14] M. Von Rohr, "Toric spectacle-glass," Apr. 18 1911. US Patent 989,645.
- [15] A. Percival, "Periscopic lenses," *British Medical Journal*, vol. 2, no. 2133, p. 1508, 1901.
- [16] J. K. Davis, "Geometric optics in ophthalmic lens design," in *SPIE Annual Technical Symposium*, vol. 0039, International Society for Optics and Photonics, 1974.
- [17] H. W. Hill, E. D. Tillyer, and H. H. Styll, "Ophthalmic lens," Sept. 9 1919. US Patent 1,315,667.
- [18] E. D. Tillyer, "Ophthalmic lens," June 15 1926. US Patent 1,588,559.
- [19] Firma Carl Zeiss in Jena, "Menisenförmiges brillenglas," Aug. 22 1909. German Empire Patent (DRP) 217254.
- [20] W. W. Merte, "Anastigmatic lens," Nov. 21 1950. US Patent 2,530,397.
- [21] Société des Lunetiers, "Perfectionnements aux lentilles ophtalmiques de puissance," Jan. 3 1969. FR 1.552.022.
- [22] M. Jalie, "Ophthalmic spectacle lenses having a hyperbolic surface," Sept. 15 1981. US Patent 4,289,387.
- [23] G. Smith and D. A. Atchison, "Effect of conicoid asphericity on the tscherning ellipses of ophthalmic spectacle lenses," *Journal of the Optical Society of America*, vol. 73, no. 4, pp. 441–445, 1983.

## Bibliography

---

- [24] G. W. Cashell, "A short history of spectacles," *Proceedings of the Royal Society of Medicine*, vol. 64, no. 10, pp. 1063–1064, 1971.
- [25] C. M. Sullivan and C. W. Fowler, "Progressive addition and variables focus lenses: A review," *Ophthalmic and Physiological Optics*, vol. 8, no. 4, pp. 402–414, 1988.
- [26] G. Minkwitz, "Über den flächenastigmatismus bei gewissen symmetrischen asphären," *Optica Acta: International Journal of Optics*, vol. 10, no. 3, pp. 223–227, 1963.
- [27] J. E. Sheedy, C. Campbell, E. King-Smith, and J. R. Hayes, "Progressive powered lenses: the minkwitz theorem," *Optometry and Vision Science*, vol. 82, no. 10, pp. 916–922, 2005.
- [28] O. Aves, "Improvements in and relating to multifocal lenses and the like, and the method of grinding same," *GB patent*, vol. 15735, 1908.
- [29] H. Gowlland, "Multifocal lens," *Patente Canadiense*, no. 159.395, 1914.
- [30] B. Cretin-Maitenaz, "Multifocal lens having a locally variable power," Jan. 20 1959. US Patent 2,869,422.
- [31] G. Kelch, H. Lahres, and H. Wietschorke, "Spectacle lens," Aug. 22 1995. US Patent 5,444,503.
- [32] A. Hof and A. Hanssen, "Spectacle lens with spherical front side and multifocal back side and process for its production," July 18 2000. US Patent 6,089,713.
- [33] A. Miks, J. Novak, and P. Novak, "Third-order design of aspheric spectacle lenses," *Optik*, vol. 121, no. 23, pp. 2097 – 2104, 2010.
- [34] G. Esser, W. Becken, W. Müller, P. Baumbach, J. Arasa, and D. Uttenweiler, "Derivation of the refraction equations for higher-order aberrations of local wavefronts at oblique incidence," *Journal of the Optical Society of America A*, vol. 27, pp. 218–237, Feb 2010.
- [35] A. Miks and J. Novak, "Fifth-order theory of astigmatism of thin spherical spectacle lenses," *Optometry and Vision Science*, vol. 88, Nov 2011.



- [36] P. Rojo, S. Royo, J. Ramírez, and I. Madariaga, “Numerical implementation of generalized coddington equations for ophthalmic lens design,” *Journal of Modern Optics*, vol. 61, no. 3, pp. 204–214, 2014.
- [37] G. Esser, H. Altheimer, W. Becken, and D. Uttenweiler, “Method for calculating and optimizing an eyeglass lens taking into consideration higher-order imaging errors,” Apr. 10 2014. US Patent App. 14/118,455.
- [38] G. Esser, H. Altheimer, W. Becken, and D. Uttenweiler, “Method for calculating and optimizing an eyeglass lens taking into consideration higher-order imaging errors,” Aug. 15 2017. US Patent 9,733,491.
- [39] R. Li, Z. Wang, Y. Liu, and G. Mu, “A method to design aspheric spectacles for correction of high-order aberrations of human eye,” *Science China Technological Sciences*, vol. 55, pp. 1391–1401, May 2012.
- [40] S. Barbero, “Minimum tangential error ophthalmic lens design without multi-parametric optimization,” *Optics Communications*, vol. 285, no. 12, pp. 2769 – 2773, 2012.
- [41] W.-S. Sun, C.-L. Tien, C.-C. Sun, M.-W. Chang, and H. Chang, “Ophthalmic lens design with the optimization of the aspherical coefficients,” *Optical Engineering*, vol. 39, no. 4, pp. 978 – 988 – 11, 2000.
- [42] W.-S. Sun, H. Chang, C.-C. Sun, M.-W. Chang, C.-H. Lin, and C.-L. Tien, “Design of high-power aspherical ophthalmic lenses with a reduced error budget,” *Optical Engineering*, vol. 41, no. 2, pp. 460 – 470 – 11, 2002.
- [43] R.-S. Chen, D. Chen, B. Chen, and S. Hsieh, “Systematic design of myopic ophthalmic lens,” *Asian Journal of Arts and Sciences*, vol. 1, pp. 83–95, 2010.
- [44] Z. Zalevsky, S. B. Yaish, O. Yehezkel, and M. Belkin, “Thin spectacles for myopia, presbyopia and astigmatism insensitive vision,” *Optics Express*, vol. 15, pp. 10790–10803, Aug 2007.
- [45] J. E. Sheedy, “Progressive addition lenses—matching the specific lens to patient needs,” *Optometry-Journal of the American Optometric Association*, vol. 75, no. 2, pp. 83–102, 2004.

## Bibliography

---

- [46] J. Forkel, J. L. Reiniger, A. Muschielok, A. Welk, A. Seidemann, and P. Baumbach, “Personalized progressive addition lenses: Correlation between performance and design,” *Optometry and Vision Science*, vol. 94, no. 2, pp. 208–218, 2017.
- [47] C. W. Fowler, “Method for the design and simulation of progressive addition spectacle lenses,” *Applied Optics*, vol. 32, pp. 4144–4146, Aug 1993.
- [48] J. A. Gómez-Pedrero, J. Alonso, and E. Bernabeu, “Calculation of optical imbalances in ophthalmic lenses using a new algorithm based on the local dioptric power matrix formalism,” *Journal of the Optical Society of America A*, vol. 18, no. 7, pp. 1452–1459, 2001.
- [49] M. A. Morris, S. R. Varnas, and A. D. Miller, “Progressive lens,” Nov. 25 2003. US Patent 6,652,096.
- [50] M. A. Morris, S. W. Fisher, S. R. Varnas, and D. R. Pope, “Progressive lens,” Sept. 21 2004. US Patent 6,793,340.
- [51] A. Kitani, “Progressive-power lens and design process for same,” Mar. 30 2004. US Patent 6,712,467.
- [52] G. Savio, G. Concheri, and R. Meneghello, “Progressive lens design by discrete shape modelling techniques,” *International Journal on Interactive Design and Manufacturing*, vol. 7, no. 3, pp. 135–146, 2013.
- [53] G. Qiu and X. Cui, “Hyperbolic tangential function-based progressive addition lens design,” *Applied Optics*, vol. 54, no. 35, pp. 10404–10408, 2015.
- [54] D. J. Fischer and D. T. Moore, “I like your grin: design methods for gradient-index progressive addition lenses,” in *SPIE Proceedings*, vol. 4832, International Society for Optics and Photonics, 2002.
- [55] D. J. Fischer, *Gradient-index ophthalmic lens design and polymer material studies*. University of Rochester, 2002.
- [56] D. A. Volk, “Multi-layered gradient index progressive lens,” May 29 2008. US Patent App. 11/977,353.

- [57] Y. Shitanoki, A. Tagaya, and Y. Koike, "Application of graded-index for astigmatism reduction in progressive addition lens," *Applied Physics Express*, vol. 2, no. 3, p. 032401, 2009.
- [58] Y. Shitanoki, A. Tagaya, and Y. Koike, "Copolymer-based progressive addition lens with graded index designed for astigmatism and distortion correction," *ACS Applied Materials & Interfaces*, vol. 1, no. 4, pp. 907–912, 2009.
- [59] Y. Shitanoki, A. Tagaya, and Y. Koike, "Application of polymer graded-index materials for aberration correction of progressive addition lenses," in *Organic Photonic Materials and Devices XI*, vol. 7213, p. 72130L, International Society for Optics and Photonics, 2009.
- [60] D. A. Volk, "Multi-layered gradient index progressive lens," June 22 2010. US Patent 7,740,354.
- [61] G. Li, D. L. Mathine, P. Valley, P. Äyräs, J. N. Haddock, M. S. Giridhar, G. Williby, J. Schwiegerling, G. R. Meredith, B. Kippelen, S. Honkanen, and N. Peyghambarian, "Switchable electro-optic diffractive lens with high efficiency for ophthalmic applications," in *Proceedings of the National Academy of Sciences*, vol. 103, pp. 6100–6104, National Academy of Sciences, 2006.
- [62] G. Li, P. Valley, P. Äyräs, J. Haddock, M. S. Giridhar, D. Mathine, J. Schwiegerling, G. Meredith, B. Kippelen, S. Honkanen, and N. Peyghambarian, "High-efficiency switchable diffractive lens," in *SPIE Proceedings*, vol. 6310, International Society for Optics and Photonics, 2006.
- [63] G. Li, P. Valley, P. Äyräs, D. L. Mathine, S. Honkanen, and N. Peyghambarian, "High-efficiency switchable flat diffractive ophthalmic lens with three-layer electrode pattern and two-layer via structures," *Applied Physics Letters*, vol. 90, no. 11, p. 111105, 2007.
- [64] P. Valley, D. L. Mathine, M. R. Dodge, J. Schwiegerling, G. Peyman, and N. Peyghambarian, "Tunable-focus flat liquid-crystal diffractive lens," *Optics Letters*, vol. 35, pp. 336–338, Feb 2010.
- [65] Y.-H. Lin and H.-S. Chen, "Electrically tunable-focusing and polarizer-free liquid crystal lenses for ophthalmic applications," *Optics Express*, vol. 21, pp. 9428–9436, Apr 2013.

## Bibliography

---

- [66] N. Hasan, A. Banerjee, H. Kim, and C. H. Mastrangelo, “Tunable-focus lens for adaptive eyeglasses,” *Optics Express*, vol. 25, pp. 1221–1233, Jan 2017.
- [67] I. Mitsui Chemicals, “The fusion of progressive addition lenses and electronic liquid crystal lenses gets spectacle lenses to a new dimension (translated).” <https://www.touchfocus.com/>. accessed 2019-03-13.
- [68] G. D. Award, “Good design best100 winners 2018.” <http://www.g-mark.org/award/describe/47002>. accessed 2019-03-13.
- [69] J. Taberero, D. Vazquez, A. Seidemann, D. Uttenweiler, and F. Schaeffel, “Effects of myopic spectacle correction and radial refractive gradient spectacles on peripheral refraction,” *Vision Research*, vol. 49, no. 17, pp. 2176–2186, 2009.
- [70] P. Rojo, S. Royo, J. Caum, J. Ramírez, and I. Madariaga, “Generalized ray tracing method for the calculation of the peripheral refraction induced by an ophthalmic lens,” *Optical Engineering*, vol. 54, no. 2, p. 025106, 2015.
- [71] J. T. Leung and B. Brown, “Progression of myopia in hong kong chinese schoolchildren is slowed by wearing progressive lenses,” *Optometry and Vision Science*, vol. 76, no. 6, pp. 346–354, 1999.
- [72] D. J. Kris, S. J. Edwards, S. W. Fisher, S. J. Pavy, and S. R. Varnas, “Myopia lens,” Feb. 5 2002. US Patent 6,343,861.
- [73] J. Gwiazda, L. Hyman, M. Hussein, D. Everett, T. T. Norton, D. Kurtz, M. C. Leske, R. Manny, W. Marsh-Tootle, and M. Scheiman, “A randomized clinical trial of progressive addition lenses versus single vision lenses on the progression of myopia in children,” *Investigative Ophthalmology & Visual Science*, vol. 44, no. 4, pp. 1492–1500, 2003.
- [74] S. Hasebe, H. Ohtsuki, T. Nonaka, C. Nakatsuka, M. Miyata, I. Hamasaki, and S. Kimura, “Effect of progressive addition lenses on myopia progression in japanese children: a prospective, randomized, double-masked, crossover trial,” *Investigative Ophthalmology & Visual Science*, vol. 49, no. 7, pp. 2781–2789, 2008.
- [75] Z. Yang, W. Lan, J. Ge, W. Liu, X. Chen, L. Chen, and M. Yu, “The effectiveness of progressive addition lenses on the progression of myopia in chinese children,” *Ophthalmic and Physiological Optics*, vol. 29, no. 1, pp. 41–48, 2009.

- [76] P. Sankaridurg, L. Donovan, S. Varnas, A. Ho, X. Chen, A. Martinez, S. Fisher, Z. Lin, E. L. Smith III, J. Ge, *et al.*, “Spectacle lenses designed to reduce progression of myopia: 12-month results,” *Optometry and Vision Science*, vol. 87, no. 9, p. 631, 2010.
- [77] S. Hasebe, J. Jun, and S. R. Varnas, “Myopia control with positively aspherized progressive addition lenses: a 2-year, multicenter, randomized, controlled trial,” *Investigative Ophthalmology & Visual Science*, vol. 55, no. 11, pp. 7177–7188, 2014.
- [78] E. L. Smith, A. Ho, B. A. Holden, N. Greeman Jr, *et al.*, “Methods and apparatuses for altering relative curvature of field and positions of peripheral, off-axis focal positions,” Apr. 11 2006. US Patent 7,025,460.
- [79] S. Barbero and M. Faria-Ribeiro, “Foveal vision power errors induced by spectacle lenses designed to correct peripheral refractive errors,” *Ophthalmic and Physiological Optics*, vol. 38, no. 3, pp. 317–325, 2018.
- [80] R. R. A. Syms, *Practical volume holography*. Clarendon Press, 1990.
- [81] J. Marín-Sáez, J. Atencia, D. Chemisana, and M.-V. Collados, “Characterization of volume holographic optical elements recorded in bayfol hx photopolymer for solar photovoltaic applications,” *Optics Express*, vol. 24, no. 6, pp. A720–A730, 2016.
- [82] D. Gabor, “A new microscopic principle,” *Nature*, vol. 161, 1948.
- [83] D. Gabor, “Microscopy by reconstructed wave-fronts,” *Proceedings of the Royal Society of London. Series A. Mathematical and Physical Sciences*, vol. 197, no. 1051, pp. 454–487, 1949.
- [84] F. Yu and S. Jutamulia, “Holography: Origin, development, and beyond,” *Optical Memory and Neural Networks*, vol. 16, no. 1, pp. 1–16, 2007.
- [85] E. N. Leith and J. Upatnieks, “Reconstructed wavefronts and communication theory,” *Journal of the Optical Society of America*, vol. 52, no. 10, pp. 1123–1130, 1962.
- [86] Y. N. Denisyuk, “Photographic reconstruction of the optical properties of an object in its own scattered radiation field,” in *Soviet Physics Doklady*, vol. 7, p. 543, 1962.

## Bibliography

---

- [87] D. Senderakova, “White light reconstructed holograms,” in *Holography-Basic Principles and Contemporary Applications*, IntechOpen, 2013.
- [88] G. L. Rogers, “Xiv.—experiments in diffraction microscopy,” *Proceedings of the Royal Society of Edinburgh Section A: Mathematics*, vol. 63, no. 3, pp. 193–221, 1952.
- [89] W. Cathey, “Three-dimensional wavefront reconstruction using a phase hologram,” *Journal of the Optical Society of America*, vol. 55, no. 4, pp. 457–457, 1965.
- [90] W. Cathey, “Phase holograms, phase-only holograms, and kinoforms,” *Applied Optics*, vol. 9, no. 6, pp. 1478–1479, 1970.
- [91] F.-K. Bruder, T. Fäcke, and T. Rölle, “The chemistry and physics of bayfol hx film holographic photopolymer,” *Polymers*, vol. 9, no. 10, p. 472, 2017.
- [92] H. Kogelnik, “Coupled wave theory for thick hologram gratings,” *The Bell System Technical Journal*, vol. 48, no. 9, pp. 2909–2947, 1969.
- [93] M. Moharam and T. Gaylord, “Rigorous coupled-wave analysis of planar-grating diffraction,” *Journal of the Optical Society of America*, vol. 71, no. 7, pp. 811–818, 1981.
- [94] G. Tricoles, “Computer generated holograms: an historical review,” *Applied Optics*, vol. 26, no. 20, pp. 4351–4360, 1987.
- [95] L. Lessem, P. Hirsh, and J. Jordan, “Computer synthesis of holograms for 3d displays,” *Communications of the ACM*, vol. 11, pp. 661–674, 1968.
- [96] L. Lessem, P. Hirsch, and J. Jordan, “The kinoform: a new wavefront reconstruction device,” *IBM Journal of Research and Development*, vol. 13, no. 2, pp. 150–155, 1969.
- [97] F.-K. Bruder, T. Fäcke, R. Hagen, D. Hönel, T. P. Kleinschmidt, E. Orselli, C. Rewitz, T. Rölle, and G. Walze, “Diffractive optics in large sizes: computer-generated holograms (cgh) based on bayfol hx photopolymer,” in *Advances in Display Technologies V*, vol. 9385, p. 93850C, International Society for Optics and Photonics, 2015.
- [98] A. Morozov, G. Dubinin, S. Dubynin, I. Yanusik, S. I. Kim, C.-S. Choi, H. Song, H.-S. Lee, A. Putilin, S. Kopenkin, *et al.*, “High collimated coherent illumination for

- reconstruction of digitally calculated holograms: design and experimental realization,” in *Digital Optical Technologies 2017*, vol. 10335, p. 103350J, International Society for Optics and Photonics, 2017.
- [99] A. D. Cohen, “Dynamic digital holographic wavelength filtering,” *Journal of Light-wave Technology*, vol. 16, no. 7, p. 1259, 1998.
- [100] K. Wakunami, P.-Y. Hsieh, R. Oi, T. Senoh, H. Sasaki, Y. Ichihashi, M. Okui, Y.-P. Huang, and K. Yamamoto, “Projection-type see-through holographic three-dimensional display,” *Nature Communications*, vol. 7, p. 12954, 2016.
- [101] J.-H. Park and S.-B. Kim, “Optical see-through holographic near-eye-display with eyebox steering and depth of field control,” *Optics Express*, vol. 26, no. 21, pp. 27076–27088, 2018.
- [102] S.-B. Kim and J.-H. Park, “Optical see-through maxwellian near-to-eye display with an enlarged eyebox,” *Optics Letters*, vol. 43, no. 4, pp. 767–770, 2018.
- [103] B. Walther, C. Helgert, C. Rockstuhl, and T. Pertsch, “Diffractive optical elements based on plasmonic metamaterials,” *Applied Physics Letters*, vol. 98, no. 19, p. 191101, 2011.
- [104] B. Walther, C. Helgert, C. Rockstuhl, F. Setzpfandt, F. Eilenberger, E.-B. Kley, F. Lederer, A. Tünnermann, and T. Pertsch, “Spatial and spectral light shaping with metamaterials,” *Advanced Materials*, vol. 24, no. 47, pp. 6300–6304, 2012.
- [105] X. Ni, A. V. Kildishev, and V. M. Shalaev, “Metasurface holograms for visible light,” *Nature Communications*, vol. 4, p. 2807, 2013.
- [106] L. Huang, X. Chen, H. Mühlenbernd, H. Zhang, S. Chen, B. Bai, Q. Tan, G. Jin, K.-W. Cheah, C.-W. Qiu, *et al.*, “Three-dimensional optical holography using a plasmonic metasurface,” *Nature Communications*, vol. 4, p. 2808, 2013.
- [107] G. Zheng, H. Mühlenbernd, M. Kenney, G. Li, T. Zentgraf, and S. Zhang, “Metasurface holograms reaching 80% efficiency,” *Nature Nanotechnology*, vol. 10, no. 4, p. 308, 2015.
- [108] D. Wen, F. Yue, G. Li, G. Zheng, K. Chan, S. Chen, M. Chen, K. F. Li, P. W. H. Wong, K. W. Cheah, *et al.*, “Helicity multiplexed broadband metasurface holograms,” *Nature Communications*, vol. 6, p. 8241, 2015.

## Bibliography

---

- [109] L. Wang, S. Kruk, H. Tang, T. Li, I. Kravchenko, D. N. Neshev, and Y. S. Kivshar, “Grayscale transparent metasurface holograms,” *Optica*, vol. 3, no. 12, pp. 1504–1505, 2016.
- [110] Q. Wang, X. Zhang, Y. Xu, J. Gu, Y. Li, Z. Tian, R. Singh, S. Zhang, J. Han, and W. Zhang, “Broadband metasurface holograms: toward complete phase and amplitude engineering,” *Scientific Reports*, vol. 6, p. 32867, 2016.
- [111] W. Wan, J. Gao, and X. Yang, “Full-color plasmonic metasurface holograms,” *ACS Nano*, vol. 10, no. 12, pp. 10671–10680, 2016.
- [112] G. Andersen, P. Gelsinger-Austin, R. Gaddipati, P. Gaddipati, and F. Ghebremichael, “Fast, compact, autonomous holographic adaptive optics,” *Optics Express*, vol. 22, no. 8, pp. 9432–9441, 2014.
- [113] D. Faklis and G. M. Morris, “Broadband imaging with holographic lenses,” *Optical Engineering*, vol. 28, no. 6, p. 286592, 1989.
- [114] M. Domingo, I. Arias, and A. García, “Achromatic fourier processor with holographic optical lenses,” *Applied Optics*, vol. 40, no. 14, pp. 2267–2274, 2001.
- [115] J. Atencia, I. Arias, M. Quintanilla, A. García, and A. M. López, “Field improvement in a uniaxial centered lens composed of two stacked-volume holographic elements,” *Applied Optics*, vol. 38, no. 19, pp. 4011–4018, 1999.
- [116] A. M. López, J. Atencia, J. Tornos, and M. Quintanilla, “Partitioned-field uniaxial holographic lenses,” *Applied Optics*, vol. 41, no. 10, pp. 1872–1881, 2002.
- [117] T. Stone and N. George, “Hybrid diffractive-refractive lenses and achromats,” *Applied Optics*, vol. 27, no. 14, pp. 2960–2971, 1988.
- [118] T. Stone and N. George, “Bandwidth of holographic optical elements,” *Optics Letters*, vol. 7, no. 9, pp. 445–447, 1982.
- [119] T. Stone and N. George, “Wavelength performance of holographic optical elements,” *Applied Optics*, vol. 24, no. 22, pp. 3797–3810, 1985.
- [120] C.-K. Lee, J. W.-J. Wu, S.-L. Yeh, C.-W. Tu, Y.-A. Han, E. H.-Z. Liao, L. Y.-Y. Chang, I.-E. Tsai, H.-H. Lin, J. C.-T. Hsieh, *et al.*, “Optical configuration and color-



- representation range of a variable-pitch dot matrix holographic printer,” *Applied Optics*, vol. 39, no. 1, pp. 40–53, 2000.
- [121] K. Hong, S.-g. Park, J. Yeom, J. Kim, N. Chen, K. Pyun, C. Choi, S. Kim, J. An, H.-S. Lee, *et al.*, “Resolution enhancement of holographic printer using a hogel overlapping method,” *Optics Express*, vol. 21, no. 12, pp. 14047–14055, 2013.
- [122] A. V. Morozov, A. N. Putilin, S. S. Kopenkin, Y. P. Borodin, V. V. Druzhin, S. E. Dubynin, and G. B. Dubinin, “3d holographic printer: fast printing approach,” *Optics Express*, vol. 22, no. 3, pp. 2193–2206, 2014.
- [123] R. Oi, P.-Y. Chou, B. J. Jackin, K. Wakunami, Y. Ichihashi, M. Okui, Y.-P. Huang, and K. Yamamoto, “Three-dimensional reflection screens fabricated by holographic wavefront printer,” *Optical Engineering*, vol. 57, no. 6, p. 061605, 2018.
- [124] J. Su, X. Yan, Y. Huang, X. Jiang, Y. Chen, and T. Zhang, “Progress in the synthetic holographic stereogram printing technique,” *Applied Sciences*, vol. 8, no. 6, p. 851, 2018.
- [125] R. W. Gerchberg and W. O. Saxton, “A practical algorithm for the determination of phase from image and diffraction plane pictures,” *Optik*, vol. 35, no. 2, pp. 237–246, 1972.
- [126] P. Marquet, B. Rappaz, P. J. Magistretti, E. Cuche, Y. Emery, T. Colomb, and C. Depeursinge, “Digital holographic microscopy: a noninvasive contrast imaging technique allowing quantitative visualization of living cells with subwavelength axial accuracy,” *Optics Letters*, vol. 30, no. 5, pp. 468–470, 2005.
- [127] F. Charrière, A. Marian, F. Montfort, J. Kuehn, T. Colomb, E. Cuche, P. Marquet, and C. Depeursinge, “Cell refractive index tomography by digital holographic microscopy,” *Optics Letters*, vol. 31, no. 2, pp. 178–180, 2006.
- [128] J. Kühn, T. Colomb, F. Montfort, F. Charrière, Y. Emery, E. Cuche, P. Marquet, and C. Depeursinge, “Real-time dual-wavelength digital holographic microscopy with a single hologram acquisition,” *Optics Express*, vol. 15, no. 12, pp. 7231–7242, 2007.
- [129] B. Kemper and G. Von Bally, “Digital holographic microscopy for live cell applications and technical inspection,” *Applied Optics*, vol. 47, no. 4, pp. A52–A61, 2008.

## Bibliography

---

- [130] M. K. Kim, "Adaptive optics by incoherent digital holography," *Optics Letters*, vol. 37, no. 13, pp. 2694–2696, 2012.
- [131] M. K. Kim, "Incoherent digital holographic adaptive optics," *Applied Optics*, vol. 52, no. 1, pp. A117–A130, 2013.
- [132] X. A. Shen, A.-D. Nguyen, J. W. Perry, D. L. Huestis, and R. Kachru, "Time-domain holographic digital memory," *Science*, vol. 278, no. 5335, pp. 96–100, 1997.
- [133] P. Ambs, L. Bigue, Y. Fainman, R. Binet, J. Collineau, J.-C. Leheureau, and J.-P. Huignard, "Image reconstruction using electrooptic holography," in *The 16th Annual Meeting of the IEEE Lasers and Electro-Optics Society, 2003. LEOS 2003.*, vol. 1, pp. 179–180, Institute of Electrical and Electronics Engineers, 2003.
- [134] I. Yamaguchi, "Holography, speckle, and computers," *Optics and Lasers in Engineering*, vol. 39, no. 4, pp. 411–429, 2003.
- [135] C. Kohler, X. Schwab, and W. Osten, "Optimally tuned spatial light modulators for digital holography," *Applied Optics*, vol. 45, no. 5, pp. 960–967, 2006.
- [136] T. Nomura, S. Murata, E. Nitandai, and T. Numata, "Phase-shifting digital holography with a phase difference between orthogonal polarizations," *Applied Optics*, vol. 45, no. 20, pp. 4873–4877, 2006.
- [137] S. S. Kou and C. J. Sheppard, "Imaging in digital holographic microscopy," *Optics Express*, vol. 15, no. 21, pp. 13640–13648, 2007.
- [138] F.-K. Bruder, T. Fäcke, F. Grote, R. Hagen, D. Hönel, E. Koch, C. Rewitz, G. Walze, and B. Wewer, "Mass production of volume holographic optical elements (vhoes) using bayfol hx photopolymer film in a roll-to-roll copy process," in *Practical Holography XXXI: Materials and Applications*, vol. 10127, International Society for Optics and Photonics, 2017.
- [139] M. Eich, J. H. Wendorff, B. Reck, and H. Ringsdorf, "Reversible digital and holographic optical storage in polymeric liquid crystals," *Die Makromolekulare Chemie, Rapid Communications*, vol. 8, no. 1, pp. 59–63, 1987.
- [140] P. Lundquist, C. Poga, R. DeVoe, Y. Jia, W. Moerner, M.-P. Bernal, H. Coufal, R. Grygier, J. Hoffnagle, C. Jefferson, *et al.*, "Holographic digital data storage in a photorefractive polymer," *Optics Letters*, vol. 21, no. 12, pp. 890–892, 1996.

- [141] S. J. Zilker, T. Bieringer, D. Haarer, R. S. Stein, J. W. van Egmond, and S. G. Kostromine, "Holographic data storage in amorphous polymers," *Advanced Materials*, vol. 10, no. 11, pp. 855–859, 1998.
- [142] J. F. Heanue, M. C. Bashaw, and L. Hesselink, "Volume holographic storage and retrieval of digital data," *Science*, vol. 265, no. 5173, pp. 749–752, 1994.
- [143] K. Buse, A. Adibi, and D. Psaltis, "Non-volatile holographic storage in doubly doped lithium niobate crystals," *Nature*, vol. 393, no. 6686, p. 665, 1998.
- [144] S. Hvilsted, C. Sánchez, and R. Alcalá, "The volume holographic optical storage potential in azobenzene containing polymers," *Journal of Materials Chemistry*, vol. 19, no. 37, pp. 6641–6648, 2009.
- [145] D. Jurbergs, F.-K. Bruder, F. Deuber, T. Fäcke, R. Hagen, D. Hönel, T. Rölle, M.-S. Weiser, and A. Volkov, "New recording materials for the holographic industry," in *Practical Holography XXIII: Materials and Applications*, vol. 7233, p. 72330K, International Society for Optics and Photonics, 2009.
- [146] F.-K. Bruder, F. Deuber, T. Fäcke, R. Hagen, D. Hönel, D. Jurbergs, T. Rölle, and M.-S. Weiser, "Reaction-diffusion model applied to high resolution bayfol hx photopolymer," in *Practical Holography XXIV: Materials and Applications*, vol. 7619, p. 76190I, International Society for Optics and Photonics, 2010.
- [147] H. Berneth, F. K. Bruder, T. Fäcke, R. Hagen, D. Hönel, D. Jurbergs, T. Rölle, and M.-S. Weiser, "Holographic recording aspects of high-resolution bayfol hx photopolymer," in *Practical Holography XXV: Materials and Applications*, vol. 7957, p. 79570H, International Society for Optics and Photonics, 2011.
- [148] H. Berneth, F.-K. Bruder, T. Fäcke, R. Hagen, D. Hönel, T. Rölle, G. Walze, and M.-S. Weiser, "Holographic recordings with high beam ratios on improved bayfol hx photopolymer," in *Holography: Advances and Modern Trends III*, vol. 8776, p. 877603, International Society for Optics and Photonics, 2013.
- [149] H. Berneth, F.-K. Bruder, T. Fäcke, D. Jurbergs, R. Hagen, D. Hönel, T. Rölle, and G. Walze, "Bayfol hx photopolymer for full-color transmission volume bragg gratings," in *Practical Holography XXVIII: Materials and Applications*, vol. 9006, p. 900602, International Society for Optics and Photonics, 2014.

## Bibliography

---

- [150] F.-K. Bruder, T. Fäcke, R. Hagen, D. Hönel, E. Orselli, C. Rewitz, T. Rölle, and G. Walze, “Diffractive optics with high bragg selectivity: volume holographic optical elements in bayfol hx photopolymer film,” in *Optical Systems Design 2015: Optical Design and Engineering VI*, vol. 9626, p. 96260T, International Society for Optics and Photonics, 2015.
- [151] F.-K. Bruder, H. Bang, T. Fäcke, R. Hagen, D. Hönel, E. Orselli, C. Rewitz, T. Rölle, D. Vukicevic, and G. Walze, “Precision holographic optical elements in bayfol hx photopolymer,” in *Practical Holography XXX: Materials and Applications*, vol. 9771, p. 977103, International Society for Optics and Photonics, 2016.
- [152] G. Li, D. Lee, Y. Jeong, J. Cho, and B. Lee, “Holographic display for see-through augmented reality using mirror-lens holographic optical element,” *Optics Letters*, vol. 41, no. 11, pp. 2486–2489, 2016.
- [153] Y. Su, Z. Cai, W. Zou, L. Shi, F. Zhou, P. Guo, Y. Lu, and J. Wu, “Viewing angle enlargement in holographic augmented reality using an off-axis holographic lens,” *Optik*, vol. 172, pp. 462–469, 2018.
- [154] C. Jang, K. Bang, G. Li, and B. Lee, “Holographic near-eye display with expanded eye-box,” in *SIGGRAPH Asia 2018 Technical Papers*, p. 195, Association for Computing Machinery, 2018.
- [155] Y. Amitai, “Substrate-guided optical beam expander,” Dec. 7 2004. US Patent 6,829,095.
- [156] H. Mukawa, K. Akutsu, I. Matsumura, S. Nakano, T. Yoshida, M. Kuwahara, and K. Aiki, “A full-color eyewear display using planar waveguides with reflection volume holograms,” *Journal of the Society for Information Display*, vol. 17, no. 3, pp. 185–193, 2009.
- [157] J.-A. Piao, G. Li, M.-L. Piao, and N. Kim, “Full color holographic optical element fabrication for waveguide-type head mounted display using photopolymer,” *Journal of the Optical Society of Korea*, vol. 17, no. 3, pp. 242–248, 2013.
- [158] H.-J. Yeom, H.-J. Kim, S.-B. Kim, H. Zhang, B. Li, Y.-M. Ji, S.-H. Kim, and J.-H. Park, “3d holographic head mounted display using holographic optical elements with astigmatism aberration compensation,” *Optics Express*, vol. 23, no. 25, pp. 32025–32034, 2015.

- [159] J. Han, J. Liu, X. Yao, and Y. Wang, "Portable waveguide display system with a large field of view by integrating freeform elements and volume holograms," *Optics Express*, vol. 23, no. 3, pp. 3534–3549, 2015.
- [160] C. M. Bigler, P.-A. Blanche, and K. Sarma, "Holographic waveguide heads-up display for longitudinal image magnification and pupil expansion," *Applied Optics*, vol. 57, no. 9, pp. 2007–2013, 2018.
- [161] J. Schwider, W. Stork, N. Streibl, and R. Vökel, "Possibilities and limitations of space-variant holographic optical elements for switching networks and general interconnects," *Applied Optics*, vol. 31, no. 35, pp. 7403–7410, 1992.
- [162] J. Schwider, "Achromatic design of holographic optical interconnects," *Optical Engineering*, vol. 35, no. 3, pp. 826–832, 1996.
- [163] M. V. Collados, D. Chemisana, and J. Atencia, "Holographic solar energy systems: The role of optical elements," *Renewable and Sustainable Energy Reviews*, vol. 59, pp. 130–140, 2016.
- [164] B. D. Chrysler, Y. Wu, Z. Yu, and R. K. Kostuk, "Volume holographic lens spectrum-splitting photovoltaic system for high energy yield with direct and diffuse solar illumination," in *Next Generation Technologies for Solar Energy Conversion VIII*, vol. 10368, p. 103680G, International Society for Optics and Photonics, 2017.
- [165] Z. Yan, X. Yan, X. Jiang, H. Gao, and J. Wen, "Integral imaging based light field display with enhanced viewing resolution using holographic diffuser," *Optics Communications*, vol. 402, pp. 437–441, 2017.
- [166] M.-L. Piao, K.-C. Kwon, H.-J. Kang, K.-Y. Lee, and N. Kim, "Full-color holographic diffuser using time-scheduled iterative exposure," *Applied Optics*, vol. 54, no. 16, pp. 5252–5259, 2015.
- [167] S. Liu, X. Zhang, and H. Lai, "Artistic effect and application of moiré patterns in security holograms," *Applied Optics*, vol. 34, no. 22, pp. 4700–4702, 1995.
- [168] S. Lai, "Security holograms using an encoded reference wave," *Optical Engineering*, vol. 35, no. 9, pp. 2470–2473, 1996.

## Bibliography

---

- [169] A. K. Yetisen, H. Butt, T. Mikulchyk, R. Ahmed, Y. Montelongo, M. Humar, N. Jiang, S. Martin, I. Naydenova, and S. H. Yun, “Color-selective 2.5 d holograms on large-area flexible substrates for sensing and multilevel security,” *Advanced Optical Materials*, vol. 4, no. 10, pp. 1589–1600, 2016.
- [170] S. Zacharovas, R. Bakanas, A. Bulanovs, and V. Varadarajan, “Effective public security features for embossed holograms,” in *Practical Holography XXXI: Materials and Applications*, vol. 10127, p. 1012702, International Society for Optics and Photonics, 2017.
- [171] P. Hartmann, R. Jedamzik, S. Reichel, and B. Schreder, “Optical glass and glass ceramic historical aspects and recent developments: a schott view,” *Applied Optics*, vol. 49, no. 16, pp. D157–D176, 2010.
- [172] D. J. Meister and S. W. Fisher, “Progress in the spectacle correction of presbyopia. part 2: Modern progressive lens technologies,” *Clinical and Experimental Optometry*, vol. 91, no. 3, pp. 251–264, 2008.
- [173] F. Z. Fang, X. D. Zhang, A. Weckenmann, G. X. Zhang, and C. Evans, “Manufacturing and measurement of freeform optics,” *CIRP Annals*, vol. 62, no. 2, pp. 823–846.
- [174] D. A. Atchison, G. Smith, and G. Smith, *Optics of the Human Eye*. Butterworth-Heinemann Oxford, 2000.
- [175] H. Gross, F. Blechinger, and B. Achtner, *Handbook of Optical Systems, Volume 4, Survey of Optical Instruments*, vol. 4 of *Handbook of Optical Systems*. Wiley-VCH, 2008.
- [176] R. Kingslake, “Who discovered coddington’s equations?,” *Optics and Photonics News*, vol. 5, no. 8, pp. 20–23, 1994.
- [177] H. Goersch, *Wörterbuch der Optometrie*. Heidelberg: DOZ-Verlag, 3rd ed., 2004.
- [178] D. J. Meister and S. W. Fisher, “Progress in the spectacle correction of presbyopia. part 1: Design and development of progressive lenses,” *Clinical and Experimental Optometry*, vol. 91, no. 3, pp. 240–250, 2008.
- [179] P. Hariharan, *Basics of Holography*. Cambridge University Press, 2002.
- [180] E. Hecht, *Optics*. Addison-Wesley, 2002.

- 
- [181] B. Krüger, T. Brenner, and A. Kienle, "Solution of the inhomogeneous maxwell's equations using a born series," *Optics Express*, vol. 25, no. 21, pp. 25165–25182, 2017.
- [182] K. Rifai, R. Sessner, J. Petschulat, P. Klopffleisch, M. Burkhardt, P. Pacher, T. Kratzer, and H. Krug, "Spectacle lens having a plurality of diffraction structures for light," 2014. US Patent 20170075139A1.
- [183] C. Starr, C. Evers, and L. Starr, *Biology: Concepts and Applications*. Brooks/Cole Publishing Company, 2006.
- [184] S. Altmeyer, Y. Hu, P. Thiée, J. Matrisch, M. Wallentin, and J. Silbermann, "Multiplexing of transmission holograms in photopolymer," in *DGaO Proceedings*, Deutschen Gesellschaft für angewandte Optik e.V., 2013.
- [185] N. F. Hartman, "Heads-up display system with holographic dispersion correcting," Sept. 23 1986. US Patent 4,613,200.
- [186] R. T. Smith, "Dispersion-compensated windshield hologram virtual image display," Jan. 1 1991. US Patent 4,981,332.
- [187] C. Palmer, *Diffraction Grating Handbook*. Richardson Grating Laboratory, 2000.
- [188] P. E. Gill, W. Murray, M. A. Saunders, and M. H. Wright, "Sparse matrix methods in optimization," *SIAM Journal on Scientific and Statistical Computing*, vol. 5, no. 3, pp. 562–589, 1984.
- [189] J. M. Trapp, T. G. Jabbour, G. Kelch, T. Pertsch, and M. Decker, "Hybrid refractive holographic single vision spectacle lenses," *Journal of the European Optical Society-Rapid Publications*, vol. 15, June 18 2019.
- [190] "DIN Deutsches Institut für Normung e. V., Ophthalmic optics - Uncut finished spectacle lenses - Part 1: Specifications for single-vision and multifocal lenses (ISO 8980-1:2004); German version EN ISO 8980-1:2004."
- [191] J. Trapp, M. Decker, J. Petschulat, T. Pertsch, and T. G. Jabbour, "Holographic progressive lenses," in *Current Developments in Lens Design and Optical Engineering XIX*, vol. 10745, p. 107450G, International Society for Optics and Photonics, 2018.

## Bibliography

---

- [192] J. M. Trapp, M. Decker, J. Petschulat, T. Pertsch, and T. G. Jabbour, "Design of a 2 diopter holographic progressive lens," *Optics Express*, vol. 26, no. 25, pp. 32866–32877, 2018.
- [193] E. L. Smith III, N. Greeman Jr, A. Ho, and B. A. Holden, "Methods and apparatuses for altering relative curvature of field and positions of peripheral, off-axis focal positions," Aug. 3 2010. US Patent 7,766,482.
- [194] D. Vazquez Martinez, H. Altheimer, A. Seidemann, M. Zimmermann, and D. Uttenweiler, "An ophthalmic lens with peripheral refractive power variation," Nov. 16 2009. DE Patent 102009053467B4.
- [195] Patent application submitted.



# List of abbreviations

AOI Angle of Incidence

AR Augmented Reality

AST Astigmatism

CCD Charge Coupled Device Sensor

CE (transverse) Color Error

CGH Computer Generated Hologram

CNC Computerized Numerical Control

DE Diffraction Efficiency

FMM Fourier Modal Method

HOE Holographic Optical Element

hPAL Holographic Progressive Addition Lens

HUD Head-Up Display

PAL Progressive Addition Lens

PSF Point Spread Function

RCWA Rigorous Coupled Wave Analysis

SLM Spatial Light Modulator

SPH Spherical Power (defined in Eq. II.4)

SVSL Single Vision Spectacle Lens

VIS Visible Spectrum of Light

## Acknowledgements

This PhD project was made possible by a cooperation between FSU Jena and Carl Zeiss AG within the framework of the NOLOSS European Union (EU) project funded by the EU's Horizon 2020 research and innovation programme. I am very grateful to have received funding from the EU under the Marie Skłodowska-Curie grant agreement No 675745 as well as direct funding from Zeiss corporate research. Naturally, such a collaborative project involves many parties, and I have plenty of people to thank for their support in making this project successful.

First and foremost, I would like to express my deep gratitude towards my university supervisor Prof. THOMAS PERTSCH for accepting me as his student and guiding me through the PhD process.

Within the corporate research department of Carl Zeiss AG, my first supervisor was Dr. TOUFIC G. JABBOUR. I owe him great thanks not only for his guidance and our friendly work atmosphere, but also for mentoring me over the long distance from Oberkochen to Jena and for continuing to support me long after transferring to a new role within the Zeiss group. I would also like to thank Dr. MANUEL DECKER for becoming my second supervisor at corporate research and for supporting me to finish all publications as well as this thesis in time.

Aside from my direct supervisors, there are many people within the Zeiss group I would like to express my gratitude towards. Dr. JÖRG PETSCHULAT initiated the Zeiss participation in the NOLOSS project and I am very happy that he entrusted me to work on this challenging project. There have been many fruitful discussions on various technical topics and I would like to especially thank my friend and fellow PhD student DANIEL WERDEHAUSEN as well as Dr. CHRISTOPH MENKE, Dr. THOMAS NOBIS, ANDREA BERNER, Dr. MATTHIAS WALD, Dr. TOBIAS BÜHREN, Dr. LARS OMLOR, Dr. CHRISTOPH HUSEMANN and everyone else at corporate research for this stimulating work environment. I am also grateful for all the technical support and open discussions on spectacle lens design with people from Carl Zeiss Vision GmbH, especially Dr. PHILIPP JESTER, Dr. GERHARD KELCH,

Dr. SIEGFRIED WAHL and Dr. KATHARINA RIFAI.

A part of my work was conducted at the Laboratory of Applied Photonics Devices of EPFL. I am grateful to Prof. CHRISTOPHE MOSER for hosting me in his group and to Dr. MANON ROSTYKUS, Dr. ZAHRA MONEMHAGHDOUST and MATHIEU KUNZI for their warm welcome and sharing a lab with me.

I very much appreciated working in the framework of the NOLOSS project and I would like to thank Dr. TORALF SCHARF of EPFL for organizing NOLOSS as well as all ESRs for the supportive community that we built. In the same vein, I would like to acknowledge my colleagues at the IAP for the friendly interactions inside and outside of work as well as the great collaboration on teaching duties. I would also like to thank the reviewers of this thesis for their efforts.

Finally, I would like to thank my friends, girlfriend and family for their unconditional support. Their encouragements and patience were vital in completing this thesis.

# Ehrenwörtliche Erklärung

Ich erkläre hiermit ehrenwörtlich, dass ich die vorliegende Arbeit selbständig, ohne unzulässige Hilfe Dritter und ohne Benutzung anderer als der angegebenen Hilfsmittel und Literatur angefertigt habe. Die aus anderen Quellen direkt oder indirekt übernommenen Daten und Konzepte sind unter Angabe der Quelle gekennzeichnet.

Bei der Auswahl und Auswertung folgenden Materials haben mir die nachstehend aufgeführten Personen in der jeweils beschriebenen Weise unentgeltlich geholfen:

1. Dr. TOUFIC G. JABBOUR, damals Carl Zeiss AG, stellte seine Implementation einer FMM zur Verfügung, die ich für die Berechnungen von Beugungseffizienzen in Kapitel III benutzte.
2. Für die Berechnungen der 3D Initialwerte der HOEs in Kapitel III benutzte ich eine von Dr. LARS OMLOR, damals Carl Zeiss AG, zur Verfügung gestellte Methode zur iterativen Integration.

Weitere Personen waren an der inhaltlich-materiellen Erstellung der vorliegenden Arbeit nicht beteiligt. Insbesondere habe ich hierfür nicht die entgeltliche Hilfe von Vermittlungs- bzw. Beratungsdiensten (Promotionsberater oder andere Personen) in Anspruch genommen. Niemand hat von mir unmittelbar oder mittelbar geldwerte Leistungen für Arbeiten erhalten, die im Zusammenhang mit dem Inhalt der vorgelegten Dissertation stehen.

Die Arbeit wurde bisher weder im In- noch im Ausland in gleicher oder ähnlicher Form einer anderen Prüfungsbehörde vorgelegt.

Die geltende Promotionsordnung der Physikalisch-Astronomischen Fakultät ist mir bekannt.

Ich versichere ehrenwörtlich, dass ich nach bestem Wissen die reine Wahrheit gesagt und nichts verschwiegen habe.

Ort, Datum

Unterschrift

# Publications

## Academic

- J. M. Trapp, T. G. Jabbour, G. Kelch, T. Pertsch and M. Decker, "Hybrid refractive holographic single vision spectacle lenses" *Journal of the European Optical Society-Rapid Publications* vol. 15, 2019.
- J. M. Trapp, M. Decker, J. Petschulat, T. Pertsch and T. G. Jabbour, "Design of a 2 diopter holographic progressive lens" *Optics express* vol. 26 no. 25, 2018.
- J. M. Trapp, M. Decker, J. Petschulat, T. Pertsch and T. G. Jabbour, "Holographic progressive lenses" *Current Developments in Lens Design and Optical Engineering XIX* vol. 10745, International Society for Optics and Photonics, 2018.
- G. Hernandez-Sosa, S. Tekoglu, S. Stolz, R. Eckstein, C. Teusch, J. Trapp, U. Lemmer, M. Hamburger and N. Mechau, "The Compromises of Printing Organic Electronics: A Case Study of Gravure-Printed Light-Emitting Electrochemical Cells" *Advanced Materials* vol. 26 no. 20, 2014.

## Legal

- T. Bühren, J. M. Trapp, S. Wahl and K. Rifai, "Brillenglas für das Erzeugen voneinander beabstandeter Objektbilder" *in preparation*, expected filing date in 2019.
- J. M. Trapp, T. G. Jabbour and W. Singer, "Brillenglas mit einer Beugungsstruktur für Licht" *WO PCT/EP2019/050730*, filing date 13.01.2019.
- J. M. Trapp, T. G. Jabbour, M. Decker and W. Singer, "Verbesserte Holographische Brillen" *DE 10 2018117 020.3*, filing date 13.07.2018.
- J. M. Trapp, T. G. Jabbour and W. Singer, "Brillenglas mit einer Beugungsstruktur für Licht" *DE 102018100705.1*, filing date 14.01.2018.